

A thesis submitted in fulfillment of the requirements for the degree of
Master of Science
in
Nuclear, Particle and Astrophysics

**Development of New Methods to Include Systematic Effects
in the First Tritium Data Analysis and Sensitivity Studies
of the KATRIN Experiment**

Entwicklung neuer Methoden zur Berücksichtigung
von systematischen Effekten
in der Analyse von ersten Tritium Daten und Sensitivitätsstudien
im KATRIN Experiment

Author: Lisa Schlüter
Reviewer: Prof. Dr. Susanne Mertens
Second Reviewer: Prof. Dr. Stefan Schönert
Supervisor: Dr. Thierry Lasserre

January 24, 2019

Erklärung der Selbstständigkeit

Ich versichere hiermit, dass ich die von mir eingereichte Masterarbeit selbstständig verfasst und keine anderen als die angegebenen Quellen und Hilfsmittel benutzt habe.

Declaration of Authorship

I hereby declare that I am the sole author of this master thesis. All direct or indirect sources used are acknowledged as references.

Lisa Schlüter
München, 24.01.2019

Contents

1	Introduction	1
2	Neutrino Physics	3
2.1	Postulation and Discovery	3
2.2	Neutrino Oscillations	4
2.3	Neutrino Mass Determination	7
3	The KATRIN Experiment	11
3.1	Experimental Setup	11
3.2	Model of the Integral Spectrum	15
3.3	Measurement Time Distribution	19
4	Analysis Software and Strategy	21
4.1	Samak	21
4.2	FPD Pixel Combination	22
4.3	Run Combination	23
5	Statistical Methods	29
5.1	Parameter Inference	29
5.2	Confidence Intervals	30
5.3	Uncertainty Propagation	31
5.4	Covariance Matrix Approach	32
5.5	Average of Correlated Parameters	34
6	Assessment of Systematic Uncertainties	37
6.1	General Remarks on Displayed Covariance Matrices	37
6.2	Molecular Final State Distribution	38
6.3	Theoretical Corrections	40
6.4	Tritium Activity Fluctuations	42
6.5	Response Function	42
6.6	Background	44
6.7	Run Combination - Stacking	45
7	First Tritium Campaign	49
7.1	Description of Data	49
7.2	Systematic Uncertainty Budget	51
7.3	Expected Sensitivity	52
7.4	Statistical Analysis	52
7.5	Analysis with Systematic Effects	55

8	KATRIN Neutrino Mass Sensitivity	67
8.1	Elevated Background	67
8.2	Measurement Time Distribution	68
8.3	Systematic Uncertainty Budget	70
8.4	KATRIN Design Report (TDR) Sensitivity	71
8.5	Sensitivity with Current Background Level of 364 mcps	72
8.6	Sensitivity with SDS Background Level of 201 mcps	76
9	Summary and Conclusion	81
	Appendices	87
A	Measurement Time Distributions	89
B	Covariance Matrices	91
B.1	Convergence Test	91
B.2	Final State Distribution	93
B.3	Response Function	94
B.4	Theoretical Corrections	95
C	First Tritium Campaign	96
D	Neutrino Mass Sensitivity Studies	98
	Acknowledgment	105

Chapter 1

Introduction

Neutrinos are the most abundant massive particles in the universe. Their properties, in particular their mass, are central parameters in the fields of particle physics and cosmology. Even though the observation of neutrino oscillations confirmed that neutrinos have non-vanishing mass, they are not sensitive to the absolute mass scale. However, neutrino oscillations do provide a lower limit of 0.05 eV on the effective mass of the electron antineutrino m_{β} . Furthermore, the parameter space is limited by an upper bound of 2 eV from direct neutrino mass experiments.

The KArllsruhe TRItium Neurino ([KATRIN](#)) experiment is designed to measure the effective electron antineutrino mass with an unprecedented sensitivity of 200 meV (90 % C.L.) after five calendar years of data taking. This is achieved in a neutrino mass model-independent way by measuring the tritium β -decay spectrum in the close vicinity of its endpoint at 18.6 keV. Given the tiny fraction of electrons found in this energy region and the minuscule imprint of the neutrino mass on the β -spectrum, the [KATRIN](#) experiment is equipped with an ultra-stable windowless high luminosity tritium source and an excellent energy resolution to pursue this ambitious project.

The technique of β -spectroscopy is only sensitive to the squared neutrino mass m_{β}^2 . Therefore, in order to improve the current limit on m_{β} by one order of magnitude, the total uncertainty has to be reduced even by two orders of magnitude with respect to the predecessor experiments. On one hand, the reduction of statistical uncertainty is achieved with a high tritium activity in the source. The suppression of systematic uncertainties, on the other hand, demands a hundredfold higher stability of all experimental parameters, such as the tritium gas density. Remaining systematic effects have to be understood as precisely as possible, mostly below the percent level.

The objective of this thesis is the assessment of systematic uncertainties in the [KATRIN](#) experiment with the simulation and analysis software [Samak](#), which is largely developed in the framework of this thesis, as working basis. Various systematic effects are considered, originating from the theoretical tritium spectrum, over the molecular tritium source to the main spectrometer. The associated uncertainties are propagated in a way that they can be applied to both simulation and data using the same technique. For this purpose [Samak](#) is equipped with a class, that enables the automatized calculation of covariance matrices for the [KATRIN](#) experiment for any desired set of input parameters. The systematic effects are modeled and propagated to the integral spectrum following the philosophy of the *MultiSim* method. Furthermore, features for display, combination of systematic effects and sanity checks, such as a convergence test, are developed. Additionally, a large data base of ready-to-use covariance matrices is created. The assessment of systematic effects with covariance matrices allows for the consistent neutrino mass sensitivity estimation on the one hand and the analysis of actual data on the other hand.

The developed treatment of systematic effects is applied in two ways in the course of this work: Firstly, the covariance matrices are used in the data analysis of the first [KATRIN](#) tritium data, taken in May and June 2018. To facilitate data handling and to standardize the basic data analyses in [Samak](#), a new tritium data analysis class is implemented, which allows different run and pixel combination techniques. Through an interface with the covariance matrix class, the user can choose to include any desired set of systematic effects and their associated uncertainties in the data analysis. It is demonstrated in this work, that the inclusion of systematic effects yields a more consistent data analysis in terms of goodness-of-fits and parameter stability over measurement time and

range. Additionally, the impact of different energy loss functions, final state distributions and column densities on the fit results is investigated.

Secondly, a comprehensive neutrino mass sensitivity study is performed in the light of the elevated background level of the [KATRIN](#) experiment. Two timescales are considered: One month of measurement time, which corresponds approximately to the duration of the upcoming first neutrino mass measurement campaign in March 2019, and the full anticipated measurement period of 30 month. The impact of systematic effects on the sensitivity is investigated in detail through covariance matrices, calculated individually for every considered set of [KATRIN](#) input parameters, such as measurement time distribution or magnetic field strength configuration. Generally, the higher the background rate, the less pronounced appears the modification of the integral spectrum due to the neutrino mass. Additionally, the neutrino mass signal is shifted further away from the endpoint with increasing background levels. From the point of view of statistic uncertainties alone, the loss of neutrino mass sensitivity can be compensated by exploring larger measurement energy ranges. However, in the frame of this work it is found that systematic uncertainties increase strongly when extending the measurement interval. Consequently both statistic and systematic uncertainties have to be taken into account to optimize the measurement time distribution for upcoming measurement phases.

Chapter 2

Neutrino Physics

Neutrinos are leptons without electric charge. Interacting only weakly, they do not feel the electromagnetic or strong forces, which makes them notoriously difficult to observe. Due to their extremely tiny cross sections, neutrinos are mostly detected indirectly in processes additionally involving charged particles. By measuring the other interaction partners and by applying conservation laws, neutrino properties can be inferred.

There are three sorts of neutrinos, one associated to each lepton family:

$$\begin{pmatrix} \nu_e \\ e^- \end{pmatrix} \begin{pmatrix} \nu_\mu \\ \mu^- \end{pmatrix} \begin{pmatrix} \nu_\tau \\ \tau^- \end{pmatrix}. \quad (2.1)$$

The lepton families differ in their lepton flavors. The electron neutrino ν_e is associated with electron flavor, the muon neutrino ν_μ with the muon flavor and the tau neutrino ν_τ with the tau flavor respectively. In the current state of knowledge, leptons within a family are connected by lepton number and lepton flavor conservation. According to these two conservation laws, the number of leptons of a particular family minus the number of the corresponding anti-leptons is conserved within every leptonic interaction. Therefore, the production process in eq. 2.2 is allowed, whereas the one in 2.3 is forbidden. Although neither the lepton number nor the lepton family number conservation comes from any fundamental symmetry in the standard model, the upper limits for their violations are very small [PRS⁺15].

$$\pi^+ \rightarrow \mu^+ + \nu_\mu \quad (2.2)$$

$$\pi^+ \nrightarrow e^+ + \nu_\mu \quad (2.3)$$

While masses are assigned to the three charged leptons in the standard model, neutrinos were believed to be massless. However, the discovery of neutrino oscillations in 1998 [F⁺98] and 2001 [A⁺01] proved that neutrinos indeed have masses.

This chapter is structured as follows: Section 2.1 gives a brief overview of the postulation and discovery of the neutrino. Thereafter, section 2.2 is devoted to neutrino oscillations and section 2.3 addresses the neutrino mass determination.

2.1 Postulation and Discovery

The joint history of neutrinos and mankind started in the beginning of the 20th century, when radioactivity was first being explored and the nuclear structure was still unraveled. Measurements of β^- -decay stirred controversial discussion among physicists: A continuous electron energy spectrum was measured. Believed to be a two-body decay, emitting only a proton and an electron, the energy of the latter should be constant. In an attempt to explain this puzzling observation, Wolfgang Pauli postulated the neutrino in 1930 for the first time in his famous letter to a group of physicists [Pau30].

Since neutrinos interact only extremely weakly with other particles, it took another 26 years to experimentally

confirm their existence. In 1956, Cowan and Reines detected within the *project poltergeist* electron antineutrinos from a nuclear reactor at the Savannah River Site [CJRH⁺56]. Their detector comprised a liquid scintillator, serving both as target and γ -ray detector, and water doped with cadmium chloride to enhance neutron capture signals. The electron antineutrinos undergo inverse beta decay with the free protons of the liquid scintillator

$$\bar{\nu}_e + p \rightarrow e^+ + n. \quad (2.4)$$

The emitted positron annihilates promptly with an electron into two 511 keV photons. After a time delay of several μ s, the neutron is captured by a cadmium nucleus. The capture process releases several γ -rays with a total energy of 9 MeV. This smoking gun signal enabled Cowan and Reines finally to distinguish the electron antineutrinos signal from the immense cosmic backgrounds [CJRH⁺56].

2.2 Neutrino Oscillations

2.2.1 Flavor and Mass Eigenstates

The neutrino flavor eigenstates $|\nu_e\rangle$, $|\nu_\mu\rangle$ and $|\nu_\tau\rangle$ are not identical to the neutrino mass eigenstates $|\nu_1\rangle$, $|\nu_2\rangle$ and $|\nu_3\rangle$. However, they can be expressed as linear combinations of the mass states

$$\begin{pmatrix} |\nu_e\rangle \\ |\nu_\mu\rangle \\ |\nu_\tau\rangle \end{pmatrix} = \begin{pmatrix} U_{e1} & U_{e2} & U_{e3} \\ U_{\mu1} & U_{\mu2} & U_{\mu3} \\ U_{\tau1} & U_{\tau2} & U_{\tau3} \end{pmatrix} \begin{pmatrix} |\nu_1\rangle \\ |\nu_2\rangle \\ |\nu_3\rangle \end{pmatrix}. \quad (2.5)$$

The unitary transformation matrix U is called PMNS matrix, named after Pontecorvo, who predicted neutrino-antineutrino oscillations [Pon58] and after Maki, Nakagawa and Sakata, who introduced two flavor neutrino mixing in 1962 [MNS62]. The PMNS matrix contains three mixing angles and three phases. It requires neutrinos to be massive, because the distinction between flavor and mass eigenstates would not make sense otherwise.

Being predicted by the neutrino flavor mixing theory, the observation of neutrino oscillations are a confirmation of this theory and a compelling evidence for neutrino masses.

2.2.2 Two Flavor Oscillation

This section derives neutrino oscillations in the simplified two flavor model. This example illustrates how neutrino oscillations can be observed and additionally, what can learned about the PMNS matrix.

The electron and tau flavor eigenstates can be written as a superposition of two mass eigenstates with only one mixing angle θ

$$\begin{pmatrix} |\nu_e\rangle \\ |\nu_\mu\rangle \end{pmatrix} = \begin{pmatrix} \cos \theta & \sin \theta \\ -\sin \theta & \cos \theta \end{pmatrix} \begin{pmatrix} |\nu_1\rangle \\ |\nu_2\rangle \end{pmatrix}. \quad (2.6)$$

In a weak interaction process, neutrinos are always produced in their flavor eigenstates. Let's consider an electron neutrino for example:

$$|\nu_e\rangle = \cos \theta |\nu_1\rangle + \sin \theta |\nu_2\rangle. \quad (2.7)$$

The electron antineutrino carries a fraction of both mass eigenstates. After the interaction, the electron neutrino may propagate freely in space. By applying the time propagation operator e^{-iEt} , the wave function of the physical neutrino $|\nu\rangle$ after the time t can be written as

$$|\nu(t)\rangle = \cos \theta e^{-iE_1 t} |\nu_1\rangle + \sin \theta e^{-iE_2 t} |\nu_2\rangle. \quad (2.8)$$

The fractions of $|\nu_1\rangle$ and $|\nu_2\rangle$, carried by $|\nu\rangle$, have changed by different magnitudes. This means, that the relative phase of the two mass eigenstates is not constant in time. Therefore, as a particular example the survival probability $P_{\nu_e \rightarrow \nu_e}$, that the neutrino $|\nu\rangle$ is an electron neutrino is no longer 100%. Calculated by the modulus square,

$P_{\nu_e \rightarrow \nu_e}$ is:

$$P_{\nu_e \rightarrow \nu_e}(t) = || \langle \nu(t) | \nu_e \rangle ||^2 \quad (2.9)$$

$$\Rightarrow P_{\nu_e \rightarrow \nu_e}(t) = |\cos^2 \theta + \sin^2 \theta \cdot e^{-i(E_2 - E_1)t}|^2 \quad (2.10)$$

$$\Rightarrow P_{\nu_e \rightarrow \nu_e}(t) = 1 - \sin^2(2\theta) \sin^2\left(\frac{\Delta E t}{4}\right). \quad (2.11)$$

Neutrino are ultra relativistic particles. Therefore, their energies can be expressed as:

$$E_i = \sqrt{p_i^2 + m_i^2} = p_i \sqrt{1 + \frac{m_i^2}{p_i^2}} \stackrel{\text{Taylor}}{\approx} p_i + \frac{m_i^2}{2p_i} \quad (2.12)$$

with

$$p_i \approx p \approx E. \quad (2.13)$$

It follows, that the survival probability can be rewritten as

$$\Rightarrow P_{\nu_e \rightarrow \nu_e}(t) = 1 - \sin^2(2\theta) \sin^2\left(\frac{\Delta m^2 L}{4E}\right) \quad (2.14)$$

with the neutrino energy E , the traveled distance L and the neutrino mass splitting $\Delta m^2 = m_1^2 - m_2^2$ [PRS⁺15]. The probability, that the neutrino has a muon flavor, is $1 - P_{\nu_e \rightarrow \nu_e}(t)$ respectively.

The oscillation pattern is illustrated in figure 2.1. Starting at the weak interaction point $L/E = 0 \text{ km/MeV}$, the electron neutrino has the probability of 1 to have electron flavor. While propagating through space, the survival probability changes. For a 1 MeV electron neutrino it decreases to a minimum of about 0.14 after 15.5 km. The oscillation length, that means the distance between the two maxima is $L_{\text{osc.}} \approx 31 \text{ km}$.

By measuring the oscillation pattern, the parameters of the PMNS matrix can be inferred. As can be seen in eq. 2.14, the oscillation amplitude is sensitive to the mixing angle, whereas the neutrino mass splitting can be deduced from the oscillation length.

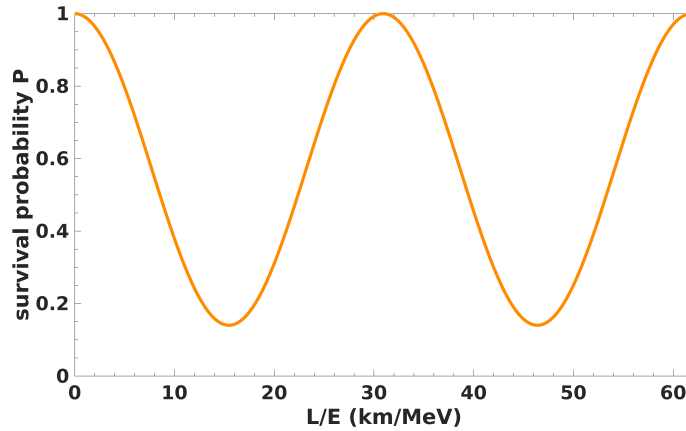


Figure 2.1: Neutrino oscillation pattern in the two flavor approximation according to eq. 2.14. The mixing angle is assumed to be $\theta = 34^\circ$ and the mass splitting $\Delta m_{12}^2 = 8 \cdot 10^{-5} \text{ eV}^2$.

2.2.3 Oscillation Parameters

In order to obtain all neutrino mass splittings and mixing angles, different neutrino sources and various neutrino energies have to be investigated. Along natural sources like the earth atmosphere, the sun and more distant

objects in the universe, also man-made sources like particle accelerators and nuclear reactors have been studied in numerous experiments. Although many hints towards the existence of neutrino oscillations were collected before, the Super-Kamiokande experiment and the Sudbury Neutrino Observatory (SNO) finally affirmed their existence.

The Super-Kamiokande experiment observed the oscillation pattern of atmospheric muon neutrinos for the first time, whereas the SNO experiment studied solar neutrinos. This confirmation of neutrino oscillations led to the award of the Nobel prize to T. Kajita and A. McDonald in 2015. These two measurements and the corresponding oscillation parameters are presented in the following.

Solar neutrino oscillation and the SNO experiment

The Homestake experiment aimed to measure the solar neutrino flux in the 1960s and confronted the physics community with a puzzling observation: The measured neutrino flux was too low by a factor of three compared to the flux expected from the solar model [DHH68]. Studying only weak interactions mediated by charged currents, they were solely sensitive to electron neutrinos. Solar muon or tau neutrinos cannot participate in such interactions, because their small energies ($E < 20$ MeV) are insufficient to produce the relatively heavy muons and taus.

However, the solar neutrino problem was resolved in 2001 by the Sudbury Neutrino Observatory (SNO) [A⁺01]. Additionally measuring neutral current interactions, the SNO experiment was sensitive to all three neutrino flavors. They confirmed that electron neutrinos, produced by fusion processes in the sun, change their flavor on their way to earth, while the total number of neutrinos is conserved. The measured neutrino flux is consistent with the solar model.

With neutrino energies in the MeV-range and a large source-detector distance of 1 AU, solar neutrino experiments are especially sensitive to the mixing angle θ_{12} and the mass splitting Δm_{12}^2 . They are found to be [T⁺]

$$\theta_{12} \approx 34^\circ \quad \text{and} \quad \Delta m_{12}^2 \approx 8 \cdot 10^{-5} \text{ eV}^2. \quad (2.15)$$

Atmospheric Neutrinos and the Super-Kamiokande experiment

The earth atmosphere is permanently bombarded with high energetic protons and heavier nuclei from cosmic rays. Interacting with the molecules in the atmosphere, large amounts of pions and kaons are produced, which decay further on into electron neutrinos and muon neutrinos, so called atmospheric neutrinos. The decay results in a flavor ratio of $\nu_\mu : \nu_e = 2 : 1$ over a wide energy range.

The Kamiokande experiment was the first experiment to observe atmospheric neutrinos. They studied charged current interactions of high energetic electron and muon neutrinos ($E > 100$ MeV) with ultrapure water in a large underground tank [PRS⁺15]. Charged leptons, produced in such an interaction, emit Cherenkov light, which is used to reconstruct the directions and energies of the incoming neutrinos. Therefore, they were able to distinguish downgoing neutrinos, flying directly from the atmosphere to the detector and upgoing neutrinos, which traveled a much longer distance through the earth.

The electron neutrino flux neither showed any unexpected angular dependence nor deviated the magnitude from its expectation. Atmospheric neutrinos travel a much shorter distance (20 km-10⁴ km) to the detector than solar neutrinos (1 AU $\approx 1.5 \cdot 10^{11}$ km). Therefore, the transition $\nu_e \rightarrow \nu_\mu$ is not observable on this scale, due to the small mass splitting Δm_{12}^2 .

In contrast to that, the muon neutrino flux showed a dependence on the direction of the incident neutrino consistent with neutrino oscillations. Additionally, the muon neutrino flux was too low by a factor of two. Since Super-Kamiokande was not sensitive to tau neutrinos, the muon neutrino disappearance was attributed to the transition $\nu_\mu \rightarrow \nu_\tau$.

The oscillation parameters¹ were found to be [T⁺]

$$\theta_{23} \approx 45^\circ \quad \text{and} \quad \Delta m_{23}^2 \approx \Delta m_{13}^2 \approx 2.4 \cdot 10^{-3} \text{ eV}^2. \quad (2.16)$$

¹The mixing angle θ_{13} , mentioned for completeness, is in the focus of reactor and accelerator neutrino experiments. It is found to be very small $\theta_{13} \approx 8.3^\circ$ [T⁺].

2.3 Neutrino Mass Determination

Although the neutrino mass splittings Δm_{ij}^2 can be inferred from neutrino oscillation experiments, the absolute neutrino mass scale is still unknown and cannot be deduced from neutrino oscillations. Currently three methods of neutrino mass determination are being explored, which are briefly presented in the following.

2.3.1 Cosmology

The Λ CDM cosmological model describes the evolution of the universe from the Big Bang to its present state. Existing in vast abundance, neutrinos have a large influence on structure formation processes in the universe. Relic neutrinos from the Big Bang still have a number density of 339 neutrinos and antineutrinos per cm^3 [LP12]. Having a large free streaming length, ultra-relativistic neutrinos act as hot dark matter and wash out small scale structures. Observations of anisotropies in the cosmic microwave background combined with large-scale structures (LSS) provide an upper limit on the sum of neutrino masses

$$m_\nu = \sum_{i=1}^3 m_i. \quad (2.17)$$

The current bounds lie between 0.12 eV and 0.73 eV [T⁺]. However, the determination of the neutrino mass by cosmological observations is rather model dependent. The obtained bounds vary substantially, depending on the underlying data sample, because the model parameters are partly degenerate. That means, that different combinations of parameters can mimic a similar effect. As an example, there is a correlation between the Hubble constant H_0 and the number of neutrino species [T⁺].

2.3.2 Neutrinoless Double β -Decay

In double β -decays, abbreviated as $2\nu\beta\beta$, two neutrons decay weakly into two protons under the emission of two electrons and two electron antineutrinos



Being a second order weak nuclear process, $2\nu\beta\beta$ may only occur when the single β -decay of a nucleus is energetically forbidden. This is depicted in figure 2.2 (left) for the example of Germanium Ge. The blue parabola represents the mass excess of $A = 76$ isobars with odd numbers of protons and neutrons, whereas the red parabola stands for the isotopes with even numbers. The smaller the masses of the isotopes are, the larger are their binding energies. The even-even isotopes are shifted towards larger binding energies with respect to the odd-odd isotopes due to the pairing interaction. Being an even-even isotope, Ge would decay in a single β -decay to the isotope with odd numbers Arsenic As, illustrated by the dotted line. However, since the binding energy of As is smaller compared to Ge, this process requires additional energy and is consequently energetically forbidden. Therefore, Ge decays over $2\nu\beta\beta$ to the even-even isotope Selenium Se. After the first observation in 1987, double β -decay has been measured for 12 different nuclei. The very long half lives are between $10^{18} - 10^{22}$ y [GP12].

Neutrinoless double β -decay, abbreviated as $0\nu\beta\beta$, is an alternative decay mode, in which the nucleus decays without the emission of neutrinos



It was first proposed by Furry in 1939 [Fur39] following the theory of Majorana, who showed that neutrinos could be their own antiparticles. In this hypothetical interaction, a massive Majorana-type virtual neutrino is exchanged inside the nucleus. However, this process violates lepton number conservation and therefore requires an extension of the standard model. The observation of $0\nu\beta\beta$ gives access to the absolute scale of the Majorana neutrino mass $m_{\beta\beta}$, written in eq. 2.20, because its decay amplitude and therefore the half life depends on the former.

$$m_{\beta\beta} = \left| \sum_{i=1}^3 U_{ei}^2 m_{\nu_i} \right| \quad (2.20)$$

This effective electron neutrino mass is the coherent sum over all neutrino mass eigenstates, weighted by the electron neutrino elements of the PMNS matrix. However, due to complex phases in the PMNS matrix, cancellations are possible.

The experimental signature of $0\nu\beta\beta$ is a monoenergetic peak at the energy of two electrons, shown in figure 2.2 (right). The electrons receive the full decay energy in $0\nu\beta\beta$, whereas in $2\nu\beta\beta$ the decay energy is continuously distributed among the two electrons and two neutrinos. At the present stage, neutrinoless double β -decay has not been observed yet. The current best upper limits on the Majorana neutrino mass comes from the KamLAND-Zen experiment for the Xe isotope [G⁺16] and from the GERDA experiment for the Ge isotope [A⁺18a] and lie within 61 meV-164 meV (Xe) and 120 meV-260 meV (Ge).

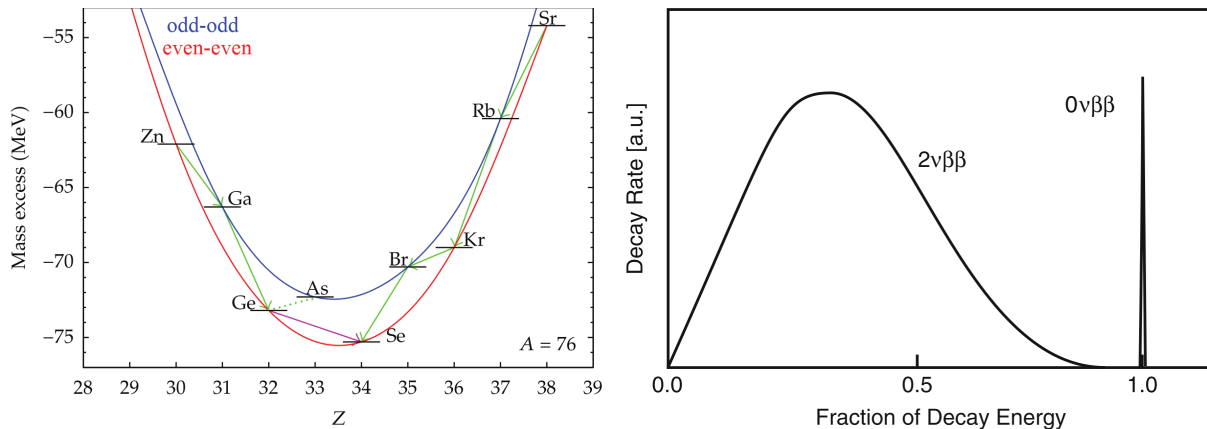


Figure 2.2: Left: Representation of the mass excesses and therefore binding energies of $A = 76$ isobars. Isotopes with even numbers of protons and neutrons lie on the red parabola, whereas isotopes with odd numbers are located along the blue parabola. The green arrows depict single β -decay. Since the former is energetically forbidden for Ge, this isotope undergoes double β -decay. Adapted from [GP12]. Right: Energy spectra of double β -decay ($2\nu\beta\beta$) and neutrinoless double β -decay ($0\nu\beta\beta$). Double β -decay has a continuous energy spectrum, whereas $0\nu\beta\beta$ manifests itself as a monoenergetic peak. Taken from [PRS⁺15].

2.3.3 Single β -Decay

Fermi Theory

During single β^- -decay, a neutron decays weakly into a proton while releasing an electron, an electron antineutrino, further on simply referred to as neutrino, and a surplus energy Q

$$n \rightarrow p + e^- + \bar{\nu}_e + Q. \quad (2.21)$$

The surplus energy is distributed among the decay products: The proton receives the recoil energy E_{rec} , the neutrino and the electron share the endpoint energy

$$E_0 = Q - E_{\text{rec}} = E_e + E_\nu. \quad (2.22)$$

Consequently, the energies of electron and neutrino are connected by energy conservation. Even if the neutrino is created without any kinetic energy, the energy available for the electron will differ from the endpoint energy by the rest mass of the neutrino. In more general words: The effective electron antineutrino mass leaves an imprint on the energy spectrum of the β -electron. The effective electron antineutrino mass is defined as the incoherent sum of the three neutrino mass eigenstates

$$m_\beta = \sqrt{\sum_{i=1}^3 |U_{ei}|^2 \cdot m_i^2}. \quad (2.23)$$

Figure 2.3 (left) depicts the differential energy spectrum of the electron, assuming a neutrino mass of zero. The imprint of m_β on the β -spectrum is visualized in figure 2.3 (right) in the close vicinity of the endpoint, where it is most prominent.

The differential spectrum, obtained by the Fermi theory, is given by

$$\frac{d\Gamma}{dE} = C \cdot F(Z, E) \cdot p \cdot (E + m_e) \cdot (E_0 - E) \cdot \sqrt{(E_0 - E)^2 - m_\nu^2} \cdot \Theta(E_0 - E - m_\nu) \quad (2.24)$$

with the kinetic energy of the electron E and its momentum p . $F(Z, E)$ corresponds to the Fermi function, taking electromagnetic interactions between outgoing electron and daughter nucleus with atomic number Z into account. The Heavyside function Θ ensures energy conservation. The constant C comprises the Fermi constant G_F , the Cabbibo angle θ_c and the nuclear matrix element \mathcal{M}_{nuc} . [OW08]

$$C = \frac{G_F^2 \cdot \cos^2 \theta_c}{2\pi^3} \cdot |\mathcal{M}_{\text{nuc}}|^2. \quad (2.25)$$

By taking advantage of the neutrino mass imprint on the spectrum, the absolute scale of the neutrino mass can be determined by measuring the β -spectrum. The small magnitude of the neutrino mass signal makes this an extremely difficult venture. The current best upper limit of 2 eV (95 % C.L.) is set by the Mainz [K⁺05] and Troitsk experiment [A⁺11]. The KATRIN experiment, described in detail in the following chapter, is the next generation single β -decay experiment.

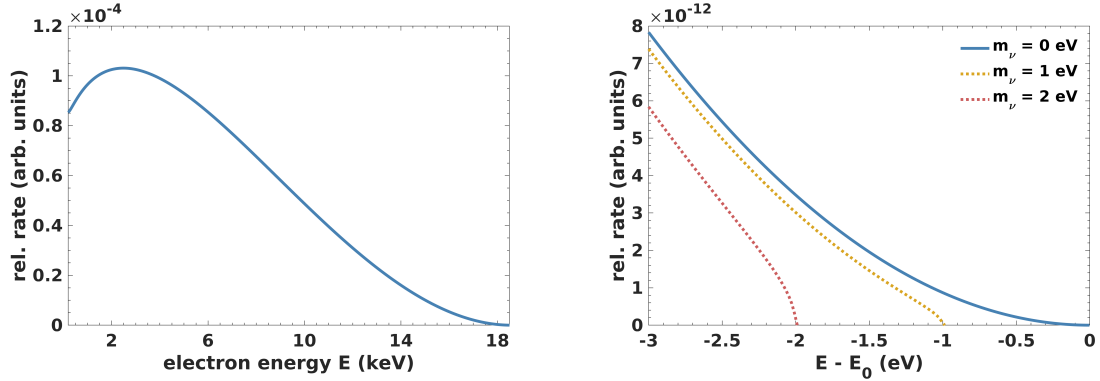


Figure 2.3: Differential β -spectrum assuming different neutrino mass. The imprint of the neutrino mass is most visible in the close vicinity of the endpoint energy E_0 .

Theoretical Corrections

Theoretical corrections to the differential β -decay spectrum arise at the particle, nuclear, atomic levels. In addition to the conventional relativistic Fermi function $F(Z, E)$ the following effects can be included.

- Radiative corrections: Electromagnetic contributions within the interaction from virtual and real photons.
- Screening: The Coulomb field of the daughter nucleus is screened by the 1s-orbital electrons.
- Recoil effects: Effect of finite nuclear mass in the energy dependent phase space.
- Finite structure of the nucleus: Corrections to Coulomb field of daughter nucleus due to its finite nuclear size and proper convolution of the lepton and nucleonic wave functions through the nuclear volume.
- Recoil of Coulomb field: Correction to Coulomb field, due to non stationary nucleus.
- Orbital-electron interactions: Interchange between the β -particle and the orbital electron.

Further details and the corresponding formulas can be found in [K⁺18].

Tritium Isotope

The Mainz and Troitsk as well as the [KATRIN](#) experiment use tritium to study β -decay. Tritium is a suitable candidate under several aspects [[Mer12](#)].

1. Being a superallowed β^- -decay, the decay of tritium has a short lifetime of $T_{1/2} = 12.3$ a. This leads to high statistics at rather low source densities.
2. Tritium has the second lowest endpoint $E_0 \approx 18.6$ keV of all β -emitters. This leads to an increased relative count rate close to the endpoint compared to isotopes with higher E_0 . Additionally, a low endpoint has technical advantages, because it requires lower voltage of the electrostatic filter, described in [3.1](#).

Chapter 3

The KATRIN Experiment

The Karlsruhe TRItium Neurino (**KATRIN**) experiment is the next generation tritium β -decay experiment designed to measure the effective electron antineutrino mass m_ν to an unprecedented sensitivity of 0.2eV^1 (90% C.L.). Aiming to improve the sensitivity one order of magnitude with respect to its predecessor experiments in Mainz [K⁺05] and Troitsk [A⁺11], the **KATRIN** experiment has pushed the established measurement technologies to their limits and is well equipped with a high luminosity tritium source and an excellent energy resolution to pursue this project.

In Section 3.1, an overview of the experimental setup and the working principle of the main components of the **KATRIN** experiment will be given. Section 3.2 addresses the modeling of the integral tritium β -spectrum. Section 3.3 is devoted to the measurement strategy in the **KATRIN** experiment.

3.1 Experimental Setup

This section gives a brief overview of the experimental setup of the **KATRIN** experiment. The particular focus here is on those components, which are essential for the modeling of the integral spectrum, described in 3.2. For a more detailed description of the experimental setup refer to the **KATRIN** Design Report (TDR) [A⁺b].

The 70m long setup is depicted in figure 3.1. The tritium β -decay takes place in the windowless gaseous tritium source (**WGTS**). The β -electrons are further on guided by the transport section to the pre- and main spectrometer, which work as electrostatic high-pass filters. The focal plane detector (**FPD**) finally counts those electrons, which have energies above a certain threshold.

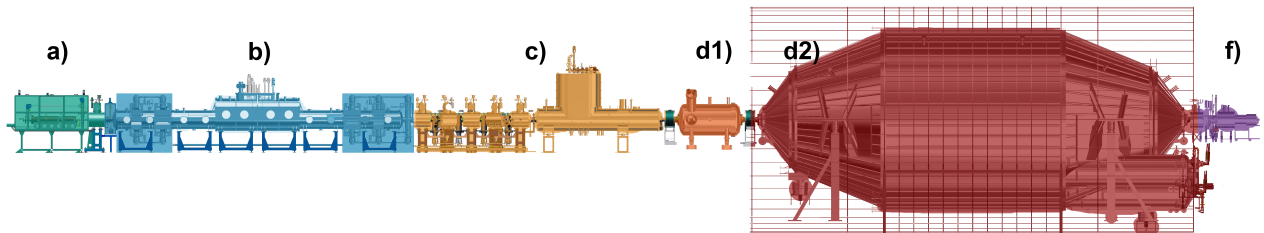


Figure 3.1: Experimental setup of the **KATRIN** experiment: a) rear section b) windowless gaseous tritium source (**WGTS**) c) transport section d1) pre-spectrometer d2) main spectrometer f) focal plane detector (**FPD**). Figure adapted from [KAT].

¹Natural units are used throughout this work: $c = \hbar = 1$.

3.1.1 Rear Section

The rear section is located at one end of the experimental setup. It comprises a gold plated rear wall, which defines the electric potential of the tritium gas in the source. Additionally, it is equipped with calibration and monitoring tools, such as an electron gun [Sch16].

3.1.2 Windowless Gaseous Tritium Source

Tritium gas is injected through capillaries into the middle of a 10 m long steel tube with a inner diameter of 90 mm, the windowless gaseous tritium source (WGTS). The gas is a mixture of mainly T_2 , DT, HT and HH. Streaming freely to both ends, the tritium gas molecules are pumped away by different turbomolecular pump stations before being re-injected again. To ensure a very high tritium purity ($> 95\%$), the gas is continuously refurbished in this closed tritium loop.

The gas column density ρd has a design value of $5 \cdot 10^{17}$ molecules/cm². The combination of high isotopic purity and column density make the WGTS a high luminosity source with a approximate decay rate of 10^{11} s^{-1} . Since variations of the column density are anticipated to be one of the dominant systematic effects, ρd is targeted to be stabilized at the 10^{-3} level.

The source tube is kept at the cryogenic temperature of 27K. Firstly, this reduces molecular motion and therefore the Doppler-shift of the β -electron energy. Secondly, undesired plasma effects of the source are minimized.

Further on, electrons, which are emitted in forward direction, are guided by superconducting solenoid magnets to the transport section. Electrons, propagating in the opposite direction, are absorbed by the rear wall [H⁺17].

3.1.3 Transport Section

The transport section comprises the differential pumping section (DPS) and the cryogenic pumping section (CPS). The goal of the transport section is to guide the β -electron adiabatically from the source to the spectrometers, while eliminating the tritium flow towards the spectrometer.

The differential pumping section reduces the tritium flow by a factor of 10^7 with a series of turbomolecular pumps. The former are not aligned along the beam tube, but tilted by an angle of 20° with respect to each other. This prevents a straight line of sight from the WGTS to the CPS. While β -electrons are magnetically guided along the magnetic field lines through the DPS by five super-conducting magnets, positive ions or molecules are prevented from passing [L⁺11].

The cryogenic pumping section reduces the molecular tritium flow by another seven orders of magnitude. Similar to the DPS, the β -electrons are guided adiabatically by seven superconducting magnets. The second and fourth magnet are inclined by an angle of 15° , which leads neutral molecules and positive ions to hit the walls. Here they are absorbed by a 3 K cold cryogenic pump with an argon frost layer [Rö17].

In total, the transport section reduces the tritium flow by 14 orders of magnitude. This high suppression factor is mandatory to keep the background level in the main spectrometer as low as possible.

3.1.4 Spectrometer Section

The basic idea of the spectrometer section is an integral measurement of the tritium β -spectrum using the established MAC-E filter principle, which combines the technology of magnetic adiabatic collimation (MAC) with an electrostatic filter (E). The spectrometer section comprises the pre- and main spectrometer, both being MAC-E filters.

Firstly, the general working principle of MAC-E filters is described. Secondly, the two spectrometers in the KATRIN experiment are presented.

MAC-E Filter Spectroscopy

At both ends of the spectrometer, two solenoid magnets, the source magnet and pinch magnet, produce strong magnetic guiding fields, shown in figure 3.2 by the green lines. Being emitted isotropically in the β -decay, the electrons enter the spectrometer with an acceptance angle of up to 2π . Due to the Lorentz force, the electrons perform cyclotron motion along the field lines inside the spectrometer, so that their energy is split in a longitudinal and a transversal part with respect to the beam axis:

$$E_e = E_{\perp} + E_{\parallel}. \quad (3.1)$$

A large negative high voltage is applied to the spectrometer vessel forming an electric potential, called retarding potential, depicted in figure 3.2 by the blue arrows, functioning as an electrostatic high-pass filter. Since the direction of the electric field is parallel to the magnetic field lines, the electrostatic energy filter is only sensitive to the longitudinal electron energy component. Therefore, only electrons entering the spectrometer with sufficient longitudinal energy pass the electrostatic barrier and are re-accelerated towards the focal plane detector. However, a neutrino mass measurement requires knowledge of the entire energy. This limitation is overcome with the magnetic adiabatic collimation principle, in which the transversal electron energy component is significantly reduced. Technically, this works as follows.

The magnetic field strength \vec{B} drops towards the center of the spectrometer about four orders of magnitude. The plane inside the spectrometer, in which the minimum of the magnetic field and the maximum of the electric field coincide, is called analyzing plane. The decrease of $|\vec{B}|$ proceeds slowly along the source side of the spectrometer and the analyzing plane, guaranteeing adiabatic motion of the electrons. As long as the gradient of the magnetic field per electron cyclotron motion is sufficiently small, the magnetic moment μ is conserved:

$$\mu \approx \frac{E_{\perp}}{|\vec{B}|} \approx \text{const.} \quad (3.2)$$

Consequently, the transversal energy component of the electron is slowly transformed into a longitudinal one on the way to the analyzing plane. Because of $B_a > 0$, the energy transformation cannot be perfect and the spectrometer remains insensitive to a residual electron energy fraction ΔE . It follows from eq. 3.2, that the relative energy resolution of the electrostatic high-pass filter is given by

$$\frac{\Delta E}{E} = \frac{B_a}{B_{\max}}. \quad (3.3)$$

The larger the difference between B_a and B_{\max} , that means the better the energy resolution, the larger the spectrometer has to be to ensure adiabaticity. Having a nominal energy resolution of only 0.93 eV, the main spectrometer requires a length of 23 m.

In addition to the previously described electrostatic reflection, the magnetic field can be used as well to select certain electrons. In case the magnetic field of the pinch magnet at the detector side B_{\max} is larger than the magnetic field of the source magnet B_s , electrons with emission polar angles larger than θ_{\max} are reflected. This effect is called magnetic mirror effect [A⁺c]. The rejection of electrons with large polar angles is advantageous, because these electrons have traveled a longer distance in the source, which enhances the probability of multiple scattering. The maximal polar angle is given by

$$\theta_{\max} = \arcsin \sqrt{\frac{B_s}{B_{\max}}}. \quad (3.4)$$

Pre- and Main Spectrometer

Being located upstream of the main spectrometer, the pre-spectrometer operates at a retarding potential of -18.3 kV. Therefore, electrons with energies less than $18.3 \text{ keV} - 18.6 \text{ keV} = 300 \text{ eV}$ below the endpoint are not able to pass this pre-spectrometer, which is advantageous because they carry no information about the neutrino mass. Additionally, the electron rate inside the main spectrometer is reduced by seven orders of magnitude [Wan13].

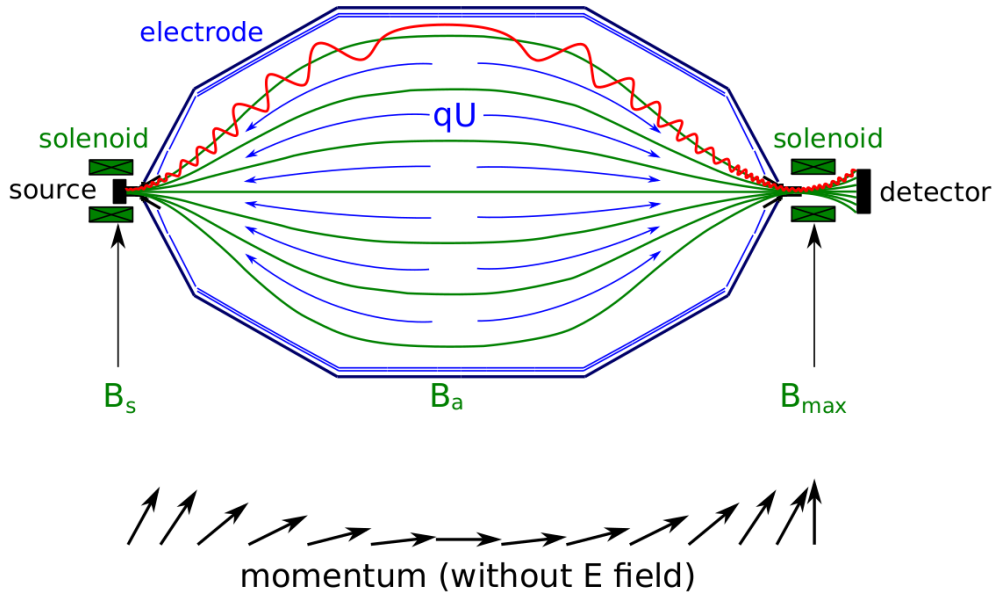


Figure 3.2: Working principle of the MAC-E filter. The green lines illustrate the magnetic field lines from the source magnetic field B_s and pinch magnetic field B_{\max} . Moving in cyclotron motions around the magnetic field lines, the electrons are guided through the spectrometer. Only electrons with sufficient energy to overcome the electric retarding potential barrier, here depicted as the blue arrows, are transmitted to the detector. Figure adapted from [Wan13].

The main spectrometer is located downstream of the pre-spectrometer. Therefore, only electrons with the highest energies are analyzed here. The nominal magnetic field strengths are $B_s = 3.6$ T, $B_{\max} = 6$ T and $B_a = 3$ G, which leads to an excellent energy resolution of 0.93 eV. Table 3.2 gives an overview of the nominal KATRIN settings. To minimize scattering inside the spectrometer, it is operated at ultra-high vacuum of 10^{-11} mbar. Additionally, the main spectrometer is equipped with an inner electrode system, consisting of more than 24,000 wires. In figure 3.2 it is illustrated by the blue lines close to the vessel walls. Set on a lightly more negative electric potential than the spectrometer walls, the inner electrode system blocks muon induced background electrons from the wall [Are16] [Mer12].

3.1.5 Focal Plane Detector

Electrons, which are transmitted through the main spectrometer, are counted by the focal plane detector (FPD). These electrons are post-accelerated on their way to the FPD to increase the detection efficiency. The FPD is a silicon semiconductor detector, segmented in 148 pixels, as depicted in figure 3.3. Each pixel records its own integral β -spectrum. This allows to correct for slight inhomogeneities of the source, magnetic and electric fields. The detection efficiency ϵ_{FPD} , typically about 0.9, is determined by physical effects such as back-scattering, intrinsic detector properties and by the region of interest (ROI). The ROI defines the energy window, measured by the FPD, within which data is analyzed. Due to the post acceleration towards the FPD of several keV, the ROI thresholds are typically above the tritium endpoint.

Finally, the integral spectrum is measured by counting the transmitted electrons at different retarding potentials. The measurement strategy in KATRIN is discussed in section 3.3.

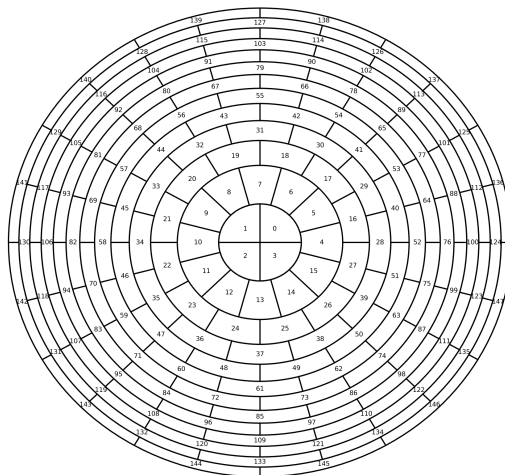


Figure 3.3: The focal plane detector (FPD) is segmented into 148 pixels to correct for inhomogeneities of the source, magnetic and electric fields.

3.2 Model of the Integral Spectrum

This section is devoted to modeling the integral tritium β -spectrum as it is measured by the [KATRIN](#) experiment. Since tritium is stored in molecular form inside the [WGTS](#), the differential β -spectrum is revised in section 3.2.1. In section 3.2.2, the response function of the [KATRIN](#) experiment is discussed. Finally, all components are joined together into an integral spectrum in section 3.2.3.

3.2.1 Final State Distribution

As described in section 2.3.3, after the β -decay the surplus energy is shared between the kinetic energy of the electron, the total energy of the neutrino, the recoil and excitation energy of the daughter molecule. The so-called final state correction of the differential β -spectrum arises from the varying excitation energy of the daughter molecule. In its electronic ground state, the excitation energy of the daughter molecule manifests itself in rotational and vibrational excitations. In addition to that, the electron shells of the daughter molecule have to rearrange themselves into the eigenstates of the daughter atomic ion. Therefore, not only the atomic ground state is populated, but a fraction of the decay ends in states with electronic excitation energy. The first electronic excited state of the daughter molecule ${}^3\text{HeT}^+$ has an excitation energy of 27 eV [[SJF](#)]. The probability distribution, according to which these excitation energies of the daughter molecule are distributed, is called final state distribution (FSD) and is illustrated in figure 3.4 for the T_2 isotopologue. Inside the source, tritium occurs in form of three different tritiated hydrogen isotopologues, namely T_2 , DT and HT. To describe the molecular tritium decay in the [KATRIN](#) experiment, the FSD for each isotopologue and its corresponding daughter molecule has to be known. The correction to the total decay rate $\frac{d\Gamma}{dE}$ is calculated by summing over all possible final states of each daughter system, weighted by the respective concentrations in the [WGTS](#).

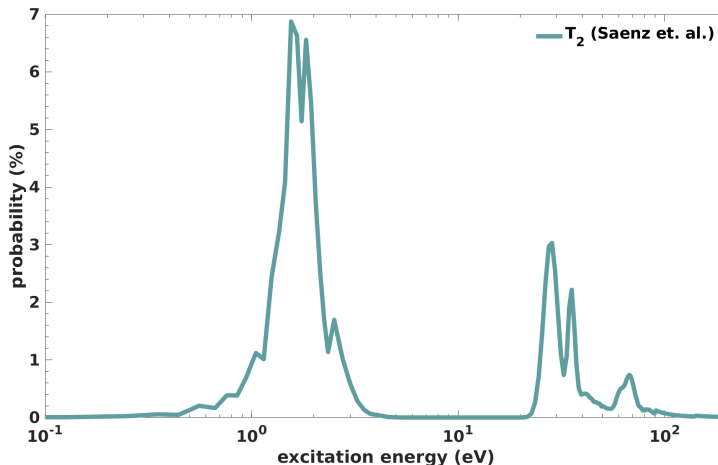


Figure 3.4: Theoretical calculation of the final state distribution for the T_2 isotopologue by Saenz *et al.* [SJF]. The leftmost peak corresponds to the rotational and vibrational excitation of daughter molecule (${}^3\text{HeT}$) $^+$ in the electronic ground state. All energies above the first peak, account for the electronic excited final states.

3.2.2 Response Function

The MAC-E transmission function $T(qU, E)$ describes the probability, that an electron with the starting energy E is able to pass the main spectrometer at the retarding potential qU :

$$T(qU, E) = \begin{cases} 0 & E < qU \\ \frac{1 - \sqrt{1 - \frac{E - qU}{E} \frac{B_s}{B_n} \frac{2}{\gamma + 1}}}{1 - \sqrt{1 - \frac{B_s}{B_{\max}}}} & qU < E < qU + \Delta E \\ 1 & E > qU + \Delta E \end{cases} \quad (3.5)$$

The relativistic factor is denoted by γ . It is analytically derivable [A⁺b]. The transmission function is visualized in figure 3.5 (left). Evidently, the transmission probability increases with increasing surplus energy $E - qU$. Electrons with energies lower than the retarding potential are not able to pass the main spectrometer, while electrons with large surplus energies always overcome the electrostatic potential barrier. However, since not the entire transversal electron energy is transformed into longitudinal energy, the MAC-E filter has a nonzero energy resolution. Electrons with a nonzero starting angle, require a starting angle-dependent amount of surplus energy to make it through the spectrometer. Being averaged over all angles up to θ_{\max} , the transmission function in eq. 3.5 only holds for isotropic emission in the source.

The MAC-E transmission function describes only the spectroscopic properties of the MAC-E filter. However, electrons may interact along their trajectory from the β -decay in the source to the focal plane detector, losing a fraction of their energy.

Due to the rather high column density ρd in the WGTS, electrons have a non-negligible probability to scatter inelastically off tritium molecules in the source section. The inelastic scattering probability for an electron with a starting position z inside the WGTS and an emission angle θ to scatter i times is calculated according to [A⁺c] with the inelastic scattering cross section σ_{inel} :

$$P_i(z, \theta) = \frac{(\lambda(z, \theta) \cdot \sigma_{\text{inel}})^i}{i!} e^{-\lambda(z, \theta) \cdot \sigma_{\text{inel}}}. \quad (3.6)$$

As can be seen in equation 3.6, the scattering probabilities $P_i(z, \theta)$ are Poisson distributed. The effective column density $\lambda(z, \theta)$, takes the path from the starting point to the exit of the source tube with length L into account:

$$\lambda(z, \theta) = \frac{1}{\cos \theta} \int_z^L \rho(z') dz'. \quad (3.7)$$

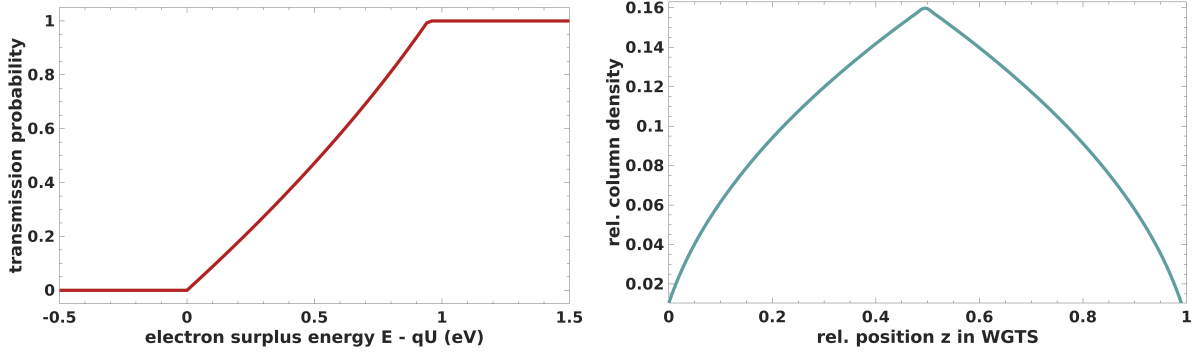


Figure 3.5: Left: **KATRIN** transmission function for nominal settings. Right: Column density profile inside the **WGTS**. The effective column density λ integrates the column density over all starting positions z .

Consequently, electrons with a large starting angle or a starting position close to the rear wall have to travel a long way inside the source and are therefore more likely to undergo several inelastic scatterings on their way out. The column density profile $\rho(z')$ is depicted in figure 3.5 (right). To obtain the mean scattering probability P_i^{inel} , $P_i(z, \theta)$ is integrated over all starting positions and allowed starting angles

$$P_i^{\text{inel}} = \frac{1}{\rho d (1 - \cos \theta_{\max})} \int_0^L dz \int_0^{\theta_{\max}} d\theta \sin \theta \rho(z) P_i(z, \theta). \quad (3.8)$$

Given the nominal $\rho d = 5 \cdot 10^{17}$ molecules/cm², the probability for an electron to scatter at least once is 59%. The scattering probabilities up to ten scatterings for nominal (**TDR**) **KATRIN** settings are given in table 3.6.

Electrons also scatter elastically in the **WGTS**. However, since the elastic scattering cross section is 12 times smaller than the inelastic one, this effect is neglected [**A⁺b**].

i	0	1	2	3	4	5	6	7	8	9	10
P_i^{inel} (%)	41.33	29.27	16.73	7.91	3.18	1.11	0.34	0.09	0.02	0.006	0.001

Table 3.1: Mean inelastic scattering probabilities for nominal **KATRIN** settings.

The energy loss function describes the probability $f(\varepsilon)$ of an electron to loose the energy ε during one inelastic scattering. Convolving the function multiple times with itself, the energy loss function for multiple scattering can be determined. This work uses the empirical energy loss function parameterizations from Aseev *et al.* [**A⁺c**] and Abdurashitov *et al.* [**A⁺a**]. As can be seen in figure 3.6, the parameterizations consist of a Gaussian peak, describing excitation processes, and of a Lorentzian tail, describing the ionization of tritium molecules. The parameterizations employ six parameters, namely the position P and width W of the ionization and excitations peaks as well as the normalization N of the two (eq. 3.9). The parameters describing the excitation part are labeled with index 1, whereas the parameters for the ionization part have index 2. The variable ε_c is chosen dynamically to ensure the continuity of $f(\varepsilon)$.

$$f(\varepsilon) = \begin{cases} N_1 \exp\left(-2 \frac{(\varepsilon - P_1)^2}{W_1^2}\right) & \text{for } \varepsilon \leq \varepsilon_c \\ N_2 \frac{W_2^2}{W_2^2 + 4(\varepsilon - P_2)^2} & \text{for } \varepsilon > \varepsilon_c \end{cases} \quad (3.9)$$

The central values of the two parameterizations and their associated uncertainty treatment is discussed in section 6.5. However, the energy loss functions from literature are not precise enough to fit in the tight systematics budget of **KATRIN**. Therefore, dedicated measurements with a monoenergetic electron gun are scheduled to measure the energy loss function with unprecedented precision.

Finally, the response function $R(E, qU)$, describing both the transmission properties of the main spectrometer as

well as the inelastic scatterings inside the **WGTS** is calculated by the convolution of the transmission function with the energy loss function:

$$R(E, qU) = \int_0^{E-qU} T(E - \varepsilon, qU) \cdot (P_0^{\text{inel}} \delta(\varepsilon) + P_1^{\text{inel}} f(\varepsilon) + P_2^{\text{inel}} [f(\varepsilon) \otimes f(\varepsilon)] + \dots) d\varepsilon. \quad (3.10)$$

The response function for nominal magnetic fields and column density, is shown in figure 3.7.

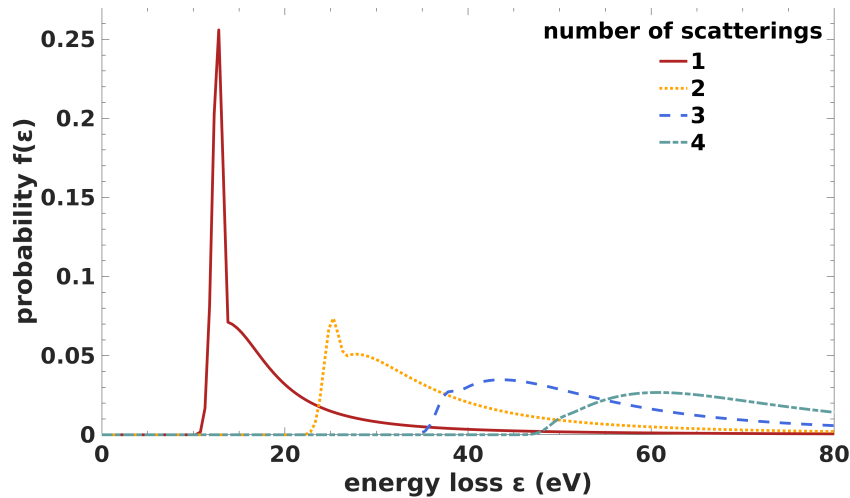


Figure 3.6: Energy loss function parametrization from Abdurashitov *et al.* [A⁺a] for four scatterings.

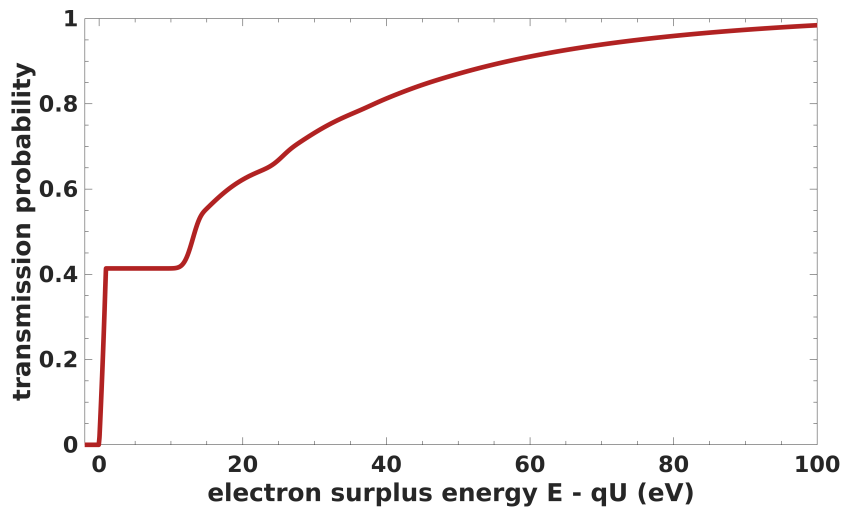


Figure 3.7: Response function for nominal settings.

3.2.3 Integral Spectrum

Once the response function is calculated, it is straight forward to transform a differential into an integral spectrum:

$$S(qU) = N \cdot \int_{qU}^{E_0} \frac{d\Gamma}{dE}(E) \cdot R(E, qU) dE + B. \quad (3.11)$$

The normalization factor N accounts for the number of tritium atoms in the source and the maximal starting angle θ_{\max} . Additionally, a constant background B is added.

Due to small inhomogeneities in the **WGTS** and in the electric and magnetic fields in the analyzing plane, every **FPD** pixels sees a slightly different integral spectrum. In section 4.2, pixel combination techniques are discussed. Figure 3.8 shows an example of an integral spectrum for nominal settings.

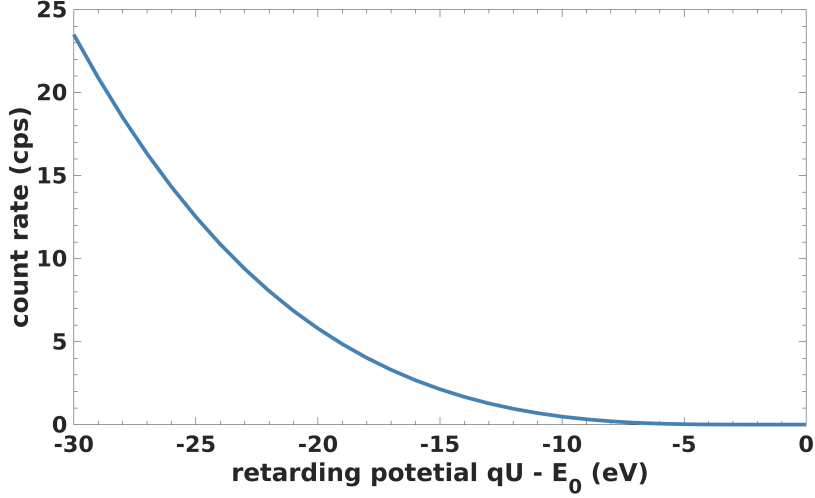


Figure 3.8: Integral spectrum for nominal settings. The nominal settings are given in table 3.2.

parameter	value
ρd	$5 \cdot 10^{17}$ molecules/cm ²
B_s	3.6 T
B_{\max}	6 T
B_a	3 G
energy resolution $\Delta E/E$	0.93 eV/18575 eV
θ_{\max}	50.77°
FPD efficiency	0.9
amount of FPD pixels	148
tritium purity	0.95
T ₂ mol. fraction	0.9
DT mol. fraction	0.05
HT mol. fraction	0.05
background rate	10 mcps

Table 3.2: Nominal settings of main **KATRIN** parameters. For information on additional parameters refer to [A⁺b].

3.3 Measurement Time Distribution

As can be seen in eq. 3.11, the integral spectrum is a function of retarding potential qU . The set of $q\vec{U}$ values, at which the integral spectrum is detected in one measurement, also referred to as one *run*, is defined by the measurement time distribution (**MTD**). Additionally, the **MTD** determines how much time is spent at each retarding potential set point, so called *subrun*. The nominal **MTD** from the **KATRIN** Design Report is shown in figure 3.9. In principle, the **MTD** could have any arbitrary shape. Aiming for the best neutrino mass sensitivity, most of the measurement time should be spent in the region of the integral spectrum, in which the neutrino mass imprint is the strongest. The **MTD** optimization in the light of higher backgrounds is discussed in section 8.2.

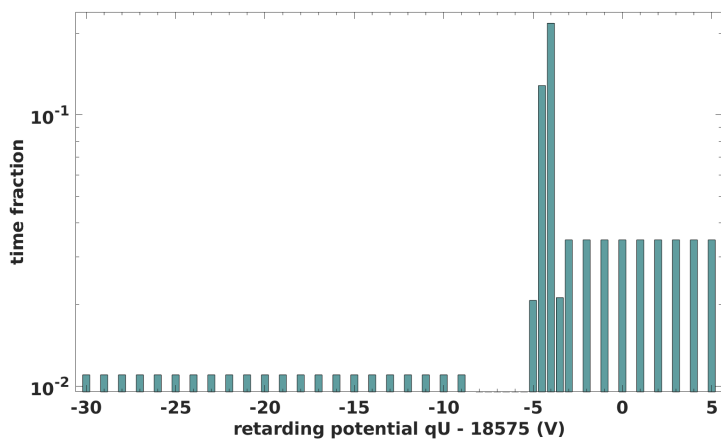


Figure 3.9: Design Report MTD, optimized for an energy interval of $[E_0 - 30 \text{ eV}, E_0 + 5 \text{ eV}]$ and nominal KATRIN settings.

Chapter 4

Analysis Software and Strategy

This chapter is devoted to a brief introduction to the analysis software [Samak](#) and the analysis strategy. Section [4.1](#) addresses the software, which is used throughout this thesis. The analysis strategies, such as pixel and run combination, are presented in sections [4.2](#) and [4.3](#).

4.1 Samak

The acronym [Samak](#) stands for Simulation and Analysis with MATLAB[®] for [KATRIN](#). [Samak](#) is devoted to analyze tritium β -spectra measured by the [KATRIN](#) experiment. For this purpose, [Samak](#) contains the following main features:

1. Interface with run summaries¹:
To analyze [KATRIN](#) data, [Samak](#) is able to process the run summaries provided by the [KATRIN](#) data taking group. All operational parameters can be retrieved and displayed.
2. Model of tritium β -spectrum:
Integral tritium β -spectra can be modeled according to section [3.2](#). For data analysis, the model input parameters can be directly read from a run summary. Additionally, [Samak](#) is able to generate Monte Carlo data for any desired set of input parameters.
3. Analysis of tritium β -spectrum:
[Samak](#) is able to analyze both [KATRIN](#) as well as [MC](#) data. The main fit parameters in this work are the neutrino mass squared m_ν^2 , the effective endpoint $E_{0\text{eff}}$, the signal normalization N and the background B . They are inferred by comparing the data points \vec{x} to the modeled expectation values for each bin $\vec{\mu}$ using a χ^2 -statistic as described in chapter [5](#). Additionally, the normalizations of ground state N_{GS} and excited states N_{ES} within the final state distribution are introduced as two additional fit parameters. Two different minimizers, namely `fminuc`, a MATLAB[®] based minimizer, and `minuit`, a minimizer developed at CERN [[Jam94](#)], are available. Confidence intervals can be constructed, both with statistic and systematic uncertainties with the methods described in section [5.2](#).
4. Systematic Uncertainties:
Systematic effects are included by covariance matrices as well as with pull terms, described in detail in sections [5.4](#) and [6](#). They can be applied both in simulations as well as in the data analysis.

Being written entirely in MATLAB[®], [Samak](#) is highly vectorized and parallelizable.

¹A run summary contains all information about the experiment during one run. Next to the number of counts and the [MTD](#), also slow control parameters such as the column density and the isotopologue concentration is given.

4.2 FPD Pixel Combination

In nominal operation mode, the tritium activity in the [KATRIN](#) experiments is very high. This implies a spatially extended source to keep the column density low. The latter is required to avoid multiple scatterings. Due to inhomogeneities in the source and the magnetic field strength in the analyzing plane, every pixel sees a slightly different integral β -spectrum. This is illustrated in the left graph in figure [4.1](#).

For simplicity, it is desired to combine the pixels in order to publish one fit result covering the information of all pixels. This can be achieved either on the level of the integral spectra or at the level of the fit results.

Furthermore, depending on the tritium activity in the [WGTS](#), a single pixel may have low statistics for retarding potentials close to the endpoint. During the first tritium campaign for example, described in section [7](#), the tritium activity was reduced such that an average three hour run had less than three counts per pixel in this energy region. However, in order to perform a χ^2 -fit, as described in [5.1](#), a sufficient large number of counts are needed to ensure an at least approximately Gaussian pdf. An increase of the analyzed statistics can be archived by combining pixels and runs. The first is presented in this section, whereas the following section ([4.3](#)) addresses the latter.

Single-Pixel and Multi-Pixel Fit

In case the number of counts in every pixel is large enough, a single-pixel or a multi-pixel fit can be performed. For both analysis types, one integral spectrum per pixel is calculated. In a single pixel fit, the pixel-wise integral spectra are fit independently one after the other, resulting in n_{pixel} values for all fit parameters. In contrast to that, all spectra are fit simultaneously in a multi-pixel fit. Furthermore, all pixels share a common endpoint and neutrino mass, while the signal normalization and the background remains pixel-wise. Being natural constants, m_ν^2 and E are the same for all pixels. However, N and B may depend for example on the flux tube volume, seen by one pixel, and are therefore pixel dependent. In case the work function differs from pixel to pixel, the effective endpoint is pixel dependent as well.

Being the most computationally expensive, the multi-pixel fit is the most accurate analysis strategy. The modeling of the response function takes all available information into account. However, due to lacking statistics during the first tritium campaign, neither the single-pixel nor the multi-pixel fit is performed in this work.

Uniform Fit

To combine the n_{pixel} integral spectra, they can be summed to one single spectrum as shown in the middle graph in figure [4.1](#). This stacked spectrum is further on estimated in the fit. For this, one would like to avoid the calculation of n_{pixel} individual integral spectra, since this is more computational expensive than the estimation of just a single averaged spectrum. However, since every pixel sees a slightly different magnetic field in the analyzing plane, every pixel requires its own corresponding response function. The model, describing the stacked spectrum, therefore employs the average of n_{pixel} response functions. A fit to a stacked spectrum is further on referred to as *uniform* fit. All fits presented in this work are uniform.

Ring Fit

Another approach to combine pixels is the segmentation of the [FPD](#) into 13 rings. Each [FPD](#) ring sees approximately the same flux tube volume. As shown in figure [4.1](#) (right), the integral spectra within one ring are summed into one spectrum per ring. Similar to the uniform fit, the modeled integral spectrum employs an average response function. However, in this segmentation one integral spectrum is calculated per ring. Whereas all information on azimuthal fluctuations are lost, this segmentation type allows the investigation of radial variations of the fit parameters. Being mentioned for completeness, this segmentation type is not employed in this thesis. For more information on the ring-wise data analysis refer to [\[MG18\]](#).

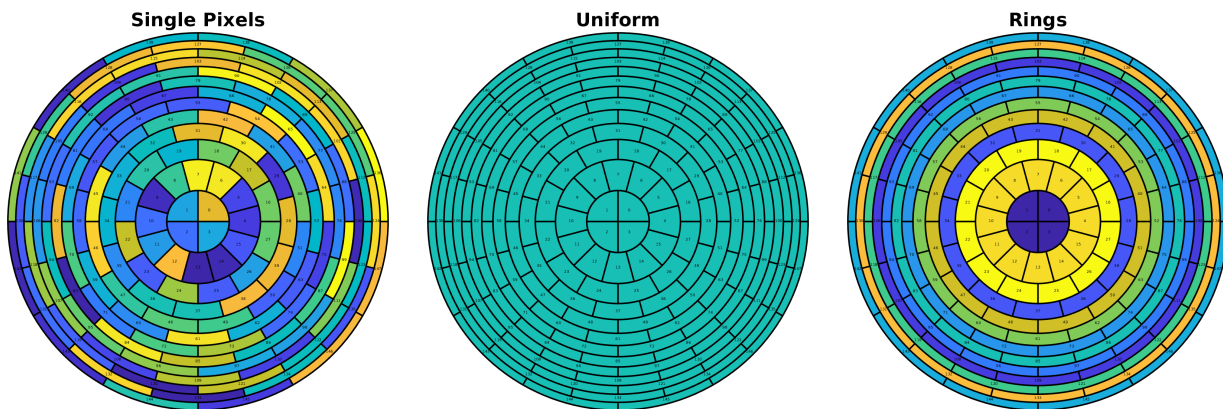


Figure 4.1: Illustration of segmentation types of the focal plane detector. The colors represent different numbers of counts. The color scale is arbitrary. **Left:** The FPD is segmented into 148 pixels. Each pixel measures an independent integral spectrum. For every pixel an integral spectrum is modeled correspondingly. **Center:** The integral spectra of all pixels are combined into one stacked spectrum. Only one integral spectrum for the whole FPD is modeled. **Right:** The FPD is segmented into 13 rings. The integral spectra within one ring are summed to one combined spectrum. Each ring sees approximately the same flux tube volume. One model integral spectrum per ring is calculated.

4.3 Run Combination

KATRIN data consist of a large set of runs², each run comprising typically one to three hours of measurement time. Each run contains a number of measurements carried out at different retarding potentials $\vec{q}\vec{U}$, called *subruns*.

In theory, the values of these retarding potential points shall be identical from one run to another. Given all other parameters are stable, one can then easily sum, or *stack*, the counts of the corresponding $\vec{q}\vec{U}$ of each run. This leads to a single stacked spectrum, that can be analyzed with a model for a single run, in which only the measurement time is scaled accordingly.

In practice, however, the sets of retarding potential values vary slightly from one run to another. Additionally, fluctuations of the molecular isotopologue fractions, for example the molecular DT fraction f_{DT} , and variations of the fraction of time spent at a given subrun $\vec{q}\vec{U}_{frac}$ is observed in the course of several runs. This is treated as follows:

Firstly, all runs have to pass quality criteria based on their $\vec{q}\vec{U}$, isotopologue concentration and ρd values, presented in section 4.3.1. Secondly as described in section 4.3.2, the stacked spectrum is calculated. For that, the single runs are corrected for $\vec{q}\vec{U}_{frac}$ and isotopologues concentration fluctuations. Thereafter they are stacked by summing their counts and averaging the retarding potential values. Finally, the stacked spectrum is modeled based on the averaged parameters of the single runs, explained in section 4.3.3.

The induced systematic uncertainty on the count rate of the integral spectrum is discussed in section 6.7.

4.3.1 Quality Criteria

To ensure the accuracy and robustness of the analysis, the runs have to pass three quality criteria to be stacked. The following criteria are illustrated with runs from the first tritium campaign, which is presented in chapter 7.

1. The subruns within a set of retarding potential values $\vec{q}\vec{U}$ are not allowed to deviate more than a tolerance of 150 meV from the average retarding potentials $\langle \vec{q}\vec{U} \rangle$. The former are defined by the mean of all stacked

²Reminder: A *run* is one scan of the differential tritium spectrum, i.e. one measurement of an integral spectrum. A *subrun* is one measurement within a run at a given retarding potential. For further explanation refer to section 3.3.

runs weighted by their measurement time t

$$\langle \vec{qU} \rangle = \frac{\sum_{r=1}^{N_r} \vec{qU}_r \cdot t_r}{\sum_{r=1}^{N_r} t_r}. \quad (4.1)$$

N_r denotes the number of stacked runs. Since N_r might change when applying one quality criterion after the other, several iterations of all criteria are performed. The qU distribution is depicted in figure 4.2 for 70 runs of the first tritium campaign. The retarding potentials vary within a subrun with a standard deviation between 40-50 meV. In this case only one run is excluded from the stacking based on its qU distribution.

2. The molecular tritium isotopologue fraction is not allowed to deviate more than 3σ from the weighted average. This quality criterion is illustrated in figure 4.3 for the molecular DT concentration. In this example, four runs are excluded from the stacking.
3. Similarly to criterion 2, the column density must not deviate more than 3σ from the weighted average. As shown in figure 4.4, all runs pass this quality criterion in this example.

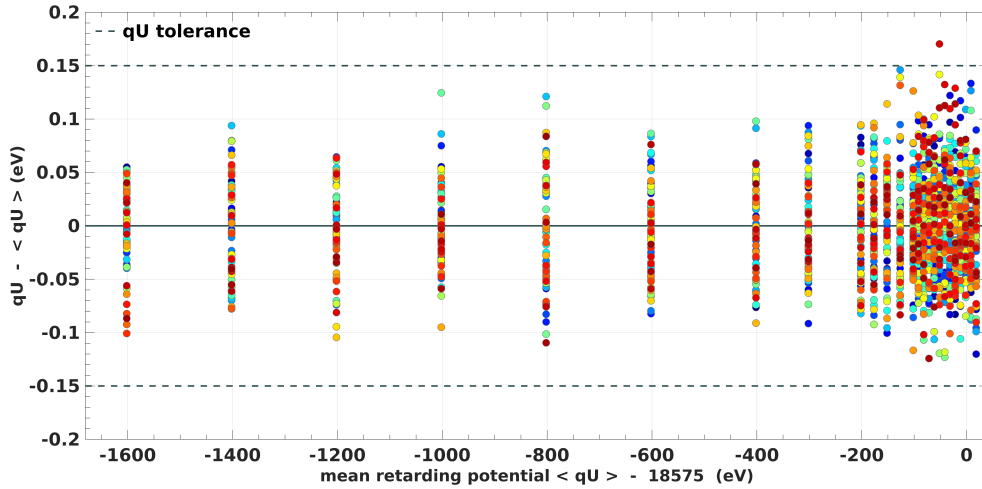


Figure 4.2: Quality criterion 1: Distribution of retarding potentials for 70 runs of the first tritium campaigns.

4.3.2 Stacked Spectrum

All runs, which pass the quality criteria, are combined through stacking. The retarding potential values for the stacked spectrum is the time weighted average $\langle \vec{qU} \rangle$ according eq. 4.1.

In addition to their \vec{qU} , the measurement time distribution of the stacked runs may differ slightly in their \vec{qU}_{frac} . This is illustrated in figure 4.5 for 70 runs of the first tritium campaign. In appendix C.1 the \vec{qU}_{frac} distribution for one subrun is depicted. When more time than in the average run is spent at a given qU , obviously more counts than in the average run is measured at this retarding potential value. If the rate was exactly the same for all runs, this deviation would just scale linearly with the time difference. However, the rate follows the small activity variations from run to run, originating from slightly different isotopologues concentrations in the WGTS. Since the differences in the \vec{qU}_{frac} may not be the same of all subruns, this does not only lead to a different overall normalization with respect to the average spectrum, but also results in a distortion of the integral spectrum with respect to the average spectrum. Therefore, the integral spectra of the single runs \vec{x}_r are corrected for the \vec{qU}_{frac}

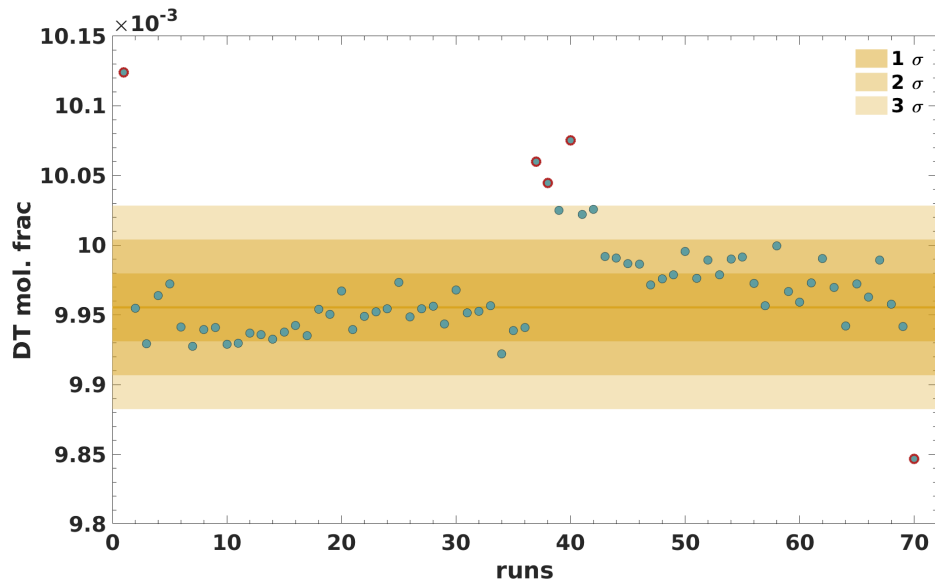


Figure 4.3: Quality criterion 2: Distribution of molecular DT fraction for 70 runs of the first tritium campaigns.

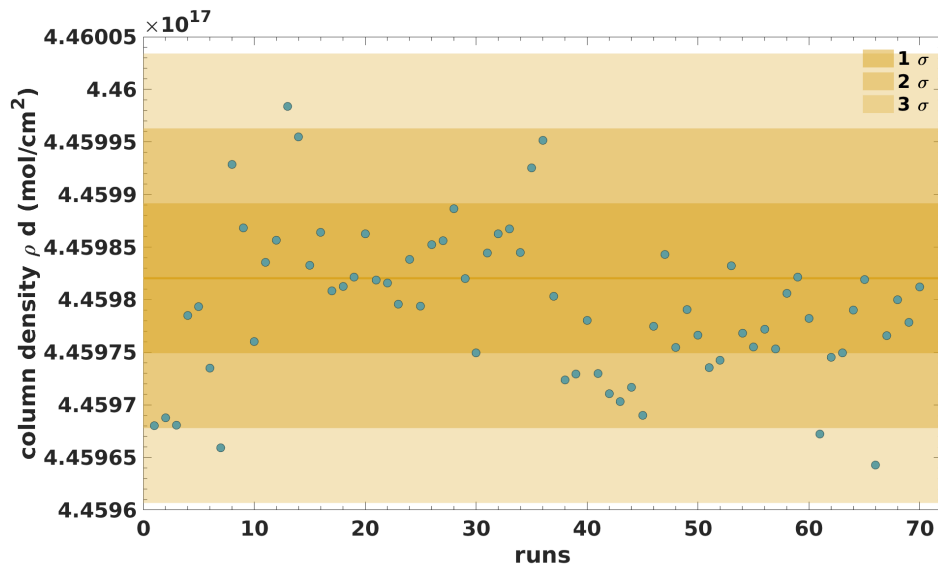


Figure 4.4: Quality criterion 3: Distribution of the column density for 70 runs of the first tritium campaigns.

and isotopologues concentration deviations f_{DT} , f_{T_2} and f_{HT} with respect to the average run before stacking:

$$\vec{x}_{r_{\text{corr}}} = \vec{x}_r \cdot \frac{\langle \vec{qU}_{\text{frac}} \rangle \cdot \langle f_{DT} \rangle \cdot \langle f_{T_2} \rangle \cdot \langle f_{HT} \rangle}{\vec{qU}_{\text{frac}} \cdot f_{DT} \cdot f_{T_2} \cdot f_{HT}}. \quad (4.2)$$

Finally, the corrected counts of the integral spectra are summed into one stacked spectrum

$$\vec{x}_{\text{stacked}} = \sum_{r=1}^{N_r} \vec{x}_{r_{\text{corr}}}. \quad (4.3)$$

This is illustrated for one subrun in figure 4.6. As can be seen in the plot, the stacked subrun has a much smaller statistical uncertainty than the subruns of the single runs.

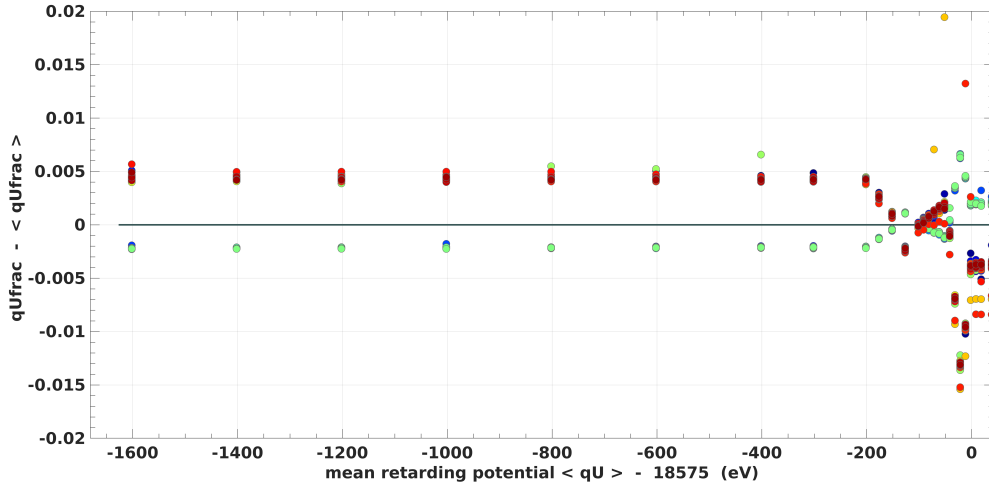


Figure 4.5: Distribution of the fraction of time spent at each subrun qU_{frac} for 70 runs of the first tritium campaigns.

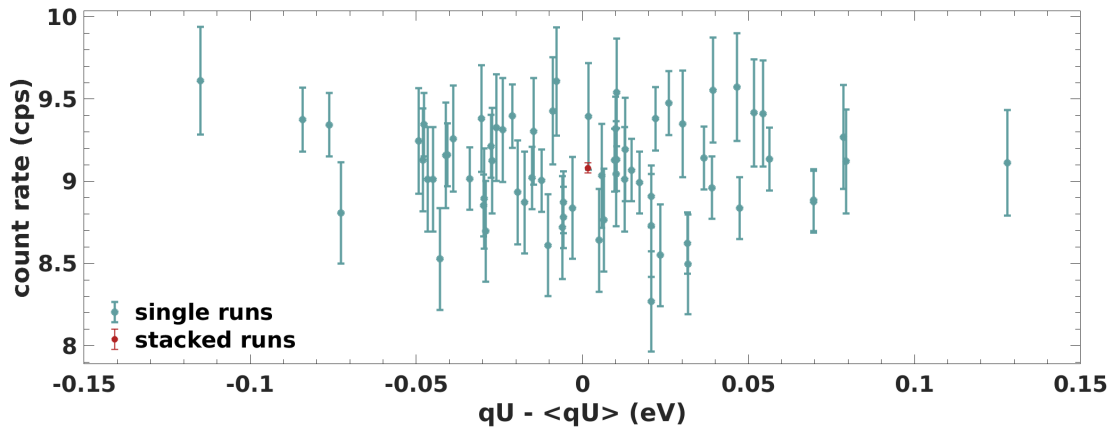


Figure 4.6: Zoom into one subrun of an integral spectrum at $qU \approx 100$ eV below the endpoint. The statistical uncertainty on the subrun measurement of the single runs is much larger than the statistical uncertainty of the stacked subrun. The standard deviation of the qU distribution of this subrun is $\sigma_{qU} \approx 42$ meV.

4.3.3 Model of Stacked Spectrum

To analyze the stacked integral spectrum, it has to be modeled according to section 3.2. The measurement time is the sum of the measurement times of the single runs. All other required input parameters are obtained by averaging the parameters from the single runs, weighted by their respective measurement time. The column density for the stacked model $\langle \rho d \rangle$, for example, is calculated as

$$\langle \rho d \rangle = \frac{\sum_{r=1}^{N_r} \rho d_r \cdot t_r}{\sum_{r=1}^{N_r} t_r}. \quad (4.4)$$

The model integral spectrum of the stacked runs is compared to the sum of the integral spectra of the single run models in figure 4.7 for 64 runs. Since the single run models employ the exact values of $\vec{q}\vec{U}$, $\vec{q}\vec{U}_{\text{frac}}$ and all other input parameters of the single runs, small discrepancies are expected. The residuals, normalized to statistic uncertainties, are larger for retarding potential far away from the endpoint than in its close vicinity. At $qU - 18575 \text{ eV} \approx 1000 \text{ eV}$ the residuals amount to 0.023σ . Given the reduced sensitivity of the first tritium campaign, this deviation is acceptable. The discrepancy originates from the averaging of $\vec{q}\vec{U}$, $\vec{q}\vec{U}_{\text{frac}}$, ρd and f_{DT} . If the former were exactly the same for all runs, the residuals would be reduced to $\approx 10^{-7}$.

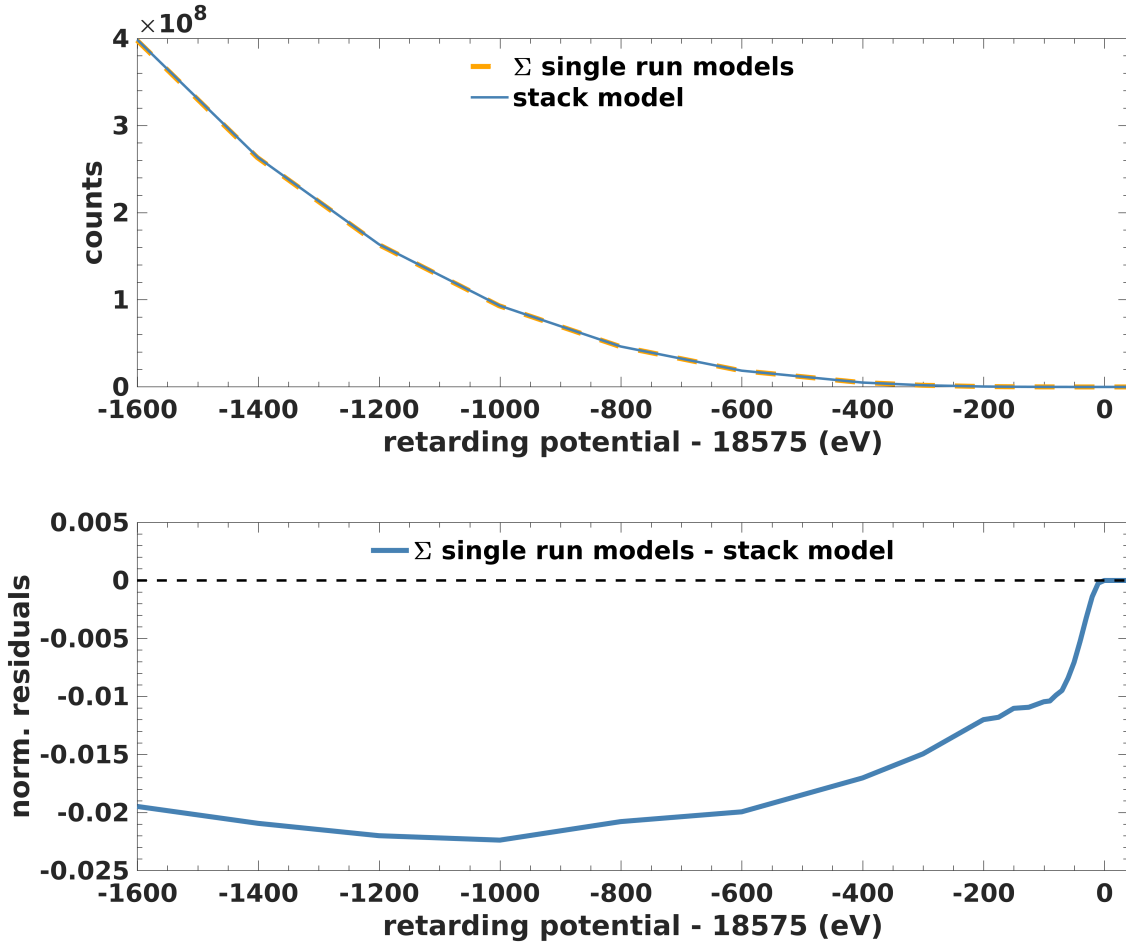


Figure 4.7: Model of stacked spectrum compared to the sum of single run models.

Chapter 5

Statistical Methods

This chapter introduces statistical concepts, relevant for this thesis, by the means of examples. Firstly, section 5.1 explains the inference of parameters from data, such as the neutrino mass in the **KATRIN!** experiment. Secondly, section 5.2 is devoted to confidence intervals. In addition to classical confidence intervals, a special case using the χ^2 -statistic is presented. Furthermore, section 5.3 addresses the propagation of uncertainties. Being a high precision experiment, **KATRIN** requires an accurate description of the influence of all systematic uncertainties, for example uncertainties on the magnetic fields, on the integral spectrum. Two strategies, namely covariance matrices and pull terms are introduced. Being the main tool to assess systematic effects in this thesis, covariance matrices and their estimation through the MultiSim approach is discussed in section 5.4. Finally, the averaging of correlated measurements is discussed in section 5.5.

5.1 Parameter Inference

The **KATRIN** experiment is designed to measure the neutrino mass. However, the neutrino mass cannot be measured directly, but has to be inferred from the integral tritium spectrum. The former is determined by counting the number of electrons for a different retarding potential set points qU . According to the central limit theorem, the probability distribution function (pdf) describing the number of counts at *one* retarding potential, follows for sufficiently large numbers of counts a Gaussian distribution. The measurements at different qUs are independent from each other, that means the measurement at one qU doesn't alter the outcome at the preceding or subsequent qU . Therefore the joint pdf f of the integral spectrum with n retarding potential bins is written as

$$f(\vec{x}) = \frac{1}{(2\pi)^{n/2} \sqrt{\det(M)}} e^{-\frac{1}{2} \overbrace{[(\vec{x} - \vec{\mu})^T M^{-1} (\vec{x} - \vec{\mu})]}^{= \chi^2}} \quad (5.1)$$

with the number of counts per bin \vec{x} and their expectation values $\vec{\mu}$. The covariance matrix M , further discussed in the following sections, takes uncertainties on the integral spectrum into account. In a measurement, \vec{x} corresponds to a set of data points, whereas $\vec{\mu}$ has to be estimated with a model. The model opens up the possibility to determine the neutrino mass, since it depends among other parameters $\vec{\theta}$ on the former:

$$\vec{\mu} = \vec{\mu}(m_\nu^2, \theta_2, \theta_3, \dots). \quad (5.2)$$

The goal of a measurement is the estimation of a set of the model parameters $\vec{\theta}$ of interest, so called fit parameters, in a way that the model describes the data as best as possible. A suitable method for the **KATRIN** data analysis is called method of least squares (LS), which requires Gaussian distributed random variables. The model parameters are estimated by minimizing the squared difference between observed data and model weighted by their correlated uncertainties, so called χ^2 (eq. 5.1) [Cow98].

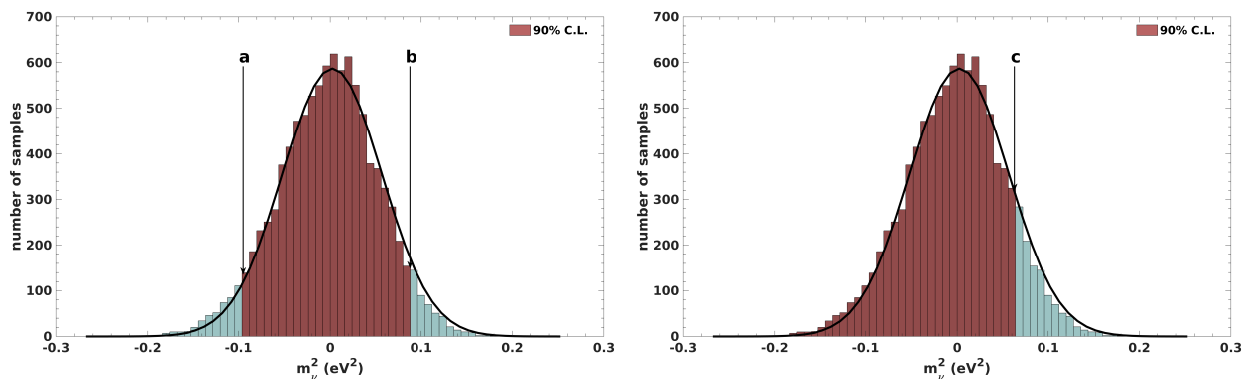


Figure 5.1: Histogram of 10,000 neutrino mass fits to Monte Carlo data for the estimation of $g(\hat{m}_\nu)$. The overlaid black curve represents a Gaussian distribution with a mean and standard deviation inferred from the Monte Carlo data sample. A χ^2 goodness-of-fit test shows, that the neutrino mass estimator \hat{m}_ν is Gaussian distributed with a p-value of 0.61. **Left:** Two-sided confidence interval **Right:** One-sided confidence interval

5.2 Confidence Intervals

Uncertainties on the fit parameters are calculated by constructing confidence intervals at a certain confidence level. In the frequentist framework, a confidence interval is defined as follows: Conducting a measurement $n \rightarrow \infty$ times, the percentage of confidence intervals, which contain the true value, is given by the confidence level. In case of Gaussian distributed estimators, 1σ corresponds to a confidence level of 68.3%. Just as the best estimate of a fit parameter, uncertainty estimates are based on data and are therefore random variables. This means that the true value doesn't have to lie within the confidence interval of one particular measurement [Bar89]. The construction of a confidence interval is illustrated for a neutrino mass fit in the following examples.

5.2.1 Classical Confidence Intervals

The estimator of a fit parameter, in this example the neutrino mass squared \hat{m}_ν^2 , is distributed according to a pdf $g(\hat{m}_\nu^2, m_\nu^2)$. Knowledge of the pdf is crucial for the construction of the confidence interval. In case $g(\hat{m}_\nu^2, m_\nu^2)$ is not known, it can be estimated by fitting the neutrino mass squared to a large sample of MC spectra as illustrated in figure 5.1 for a neutrino mass of zero. A χ^2 goodness of fit test confirms, that the estimator for the neutrino mass squared is Gaussian distributed with a p-value of 0.61.

The central two sided confidence interval, depicted in figure 5.1 (left) as the red area, is inferred from the distance of the quantiles a and b from one each other. The quantiles a and b , at a desired confidence level P , result from the following condition

$$G(a, m_\nu^2) + (1 - G(b, m_\nu^2)) = P \quad (5.3)$$

with the cumulative distribution $G(\hat{m}_\nu^2, m_\nu^2)$ of $g(\hat{m}_\nu^2, m_\nu^2)$. In case an upper limit on the neutrino mass shall be given, a one sided confidence interval is used. As shown in figure 5.1 (right), this is determined

$$G(c, m_\nu^2) = P \quad (5.4)$$

with the quantile c [Cow98].

5.2.2 Confidence Intervals with χ^2 -Statistic

In case the pdf of the estimator \hat{m}_ν^2 is Gaussian, the cumulative probability distribution function is, according to the central limit theorem, Gaussian as well. This leads to the convenient simplification that uncertainties at all

	one sided		two sided	
confidence level	uncertainty $\Delta\hat{m}_\nu^2$	N^2	uncertainty $\Delta\hat{m}_\nu^2$	N^2
90%	$1.282 \sigma_{\hat{m}_\nu^2}$	1.64	$1.645 \sigma_{\hat{m}_\nu^2}$	2.71
95%	$1.645 \sigma_{\hat{m}_\nu^2}$	2.71	$1.960 \sigma_{\hat{m}_\nu^2}$	3.84
99%	$2.326 \sigma_{\hat{m}_\nu^2}$	5.41	$2.576 \sigma_{\hat{m}_\nu^2}$	6.64

Table 5.1: Sensitivity for one and two sided confidence intervals and different confidence levels for one parameter.

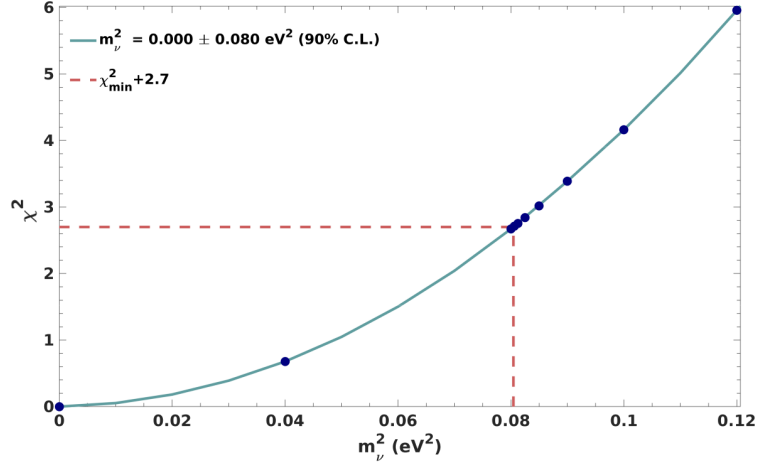


Figure 5.2: Alternative method of sensitivity computation for Gaussian estimators with an Asimov data set. The neutrino mass sensitivity (two sided confidence interval) is obtained according to eq. 5.5.

confidence levels can be expressed in terms of the standard deviation $\sigma_{\hat{m}_\nu^2}$ of the estimator \hat{m}_ν^2 . Using the LS method, the uncertainty $\Delta\hat{m}_\nu^2$ at a given confidence level is calculated with

$$\chi^2(m_\nu^2 \pm \Delta\hat{m}_\nu^2) = \chi_{\min}^2 + N^2. \quad (5.5)$$

The 1σ uncertainty is obtained with $N^2 = 1$. The corresponding values for other confidence levels for one and two sided confidence intervals are given in table 5.1. Figure 5.2 visualizes eq. 5.5 with the example of a neutrino mass fit at 90% confidence level using an Asimov data set¹. Note that this method is also applicable in the case of non-Gaussian estimators, since they become Gaussian in the large sample limit [Cow98].

5.3 Uncertainty Propagation

Statistic uncertainties on the integral spectrum \vec{x} are derived directly from the data

$$\vec{\sigma}_{stat} = \sqrt{\vec{x}}. \quad (5.6)$$

Statistic uncertainties are uncorrelated. Systematic uncertainties on model parameters, which aren't free fit parameters, can be propagated to the integral spectrum in various ways. This work applies two methods.

Firstly, error-prone model parameters can be introduced as nuisance parameters $\vec{\omega}$ in the fit.

$$\vec{\mu} = \vec{\mu}(\vec{\theta}, \vec{\omega}) \quad (5.7)$$

Nuisance parameters are therefore fit parameters, which are not of primary interest. They are usually constrained with a pull term to a certain value range within their uncertainty. This allows the fit to vary the nuisance parameter

¹Asimov data is simulated data without statistic or systematic fluctuations.

within the externally prescribed uncertainty interval $[T^+]$. The pull terms have to be added to the χ^2 function

$$\chi^2 = (\vec{x} - \vec{\mu}(\vec{\theta}, \vec{\omega}))^T M^{-1} (\vec{x} - \vec{\mu}(\vec{\theta}, \vec{\omega})) + \chi_{\text{pulls}}^2(\vec{\omega}, \Delta\vec{\omega}). \quad (5.8)$$

Secondly, systematic uncertainties on model parameters can be propagated with covariance matrices. The covariance matrix M incorporates uncorrelated uncertainties of each bin entry on its diagonal as well as bin-to-bin correlations on its off-diagonal. In case only statistic uncertainties are considered or systematic uncertainties are solely treated with nuisance parameters, M consists only of diagonal elements σ_{stat}^2 . Most of the covariance matrices in this work are estimated with the MultiSim method.

This work focuses the treatment of systematic uncertainty propagation mainly on the covariance matrix approach. Therefore, the former is discussed in detail in the following section.

5.4 Covariance Matrix Approach

5.4.1 MultiSim Method

The MultiSim² approach is a method to propagate uncertainties on a set of correlated variables \vec{a} to a complex function of these variables \vec{b} . In the [KATRIN](#) experiment, for example, the uncertainties on the correlated parameters of the energy loss function \vec{a} , have to be propagated to the integral spectrum \vec{b} . The MultiSim method requires three inputs:

1. The central values of the considered model input parameters \vec{a} . In [KATRIN](#) this translates to the central values of the energy loss function parameters.
2. Their uncertainties $\Delta\vec{a}$ including possible correlations in the form of a covariance matrix M^a . In our example, that means the uncertainties on the energy loss function parameters and the correlations between them.
3. A model, which propagates \vec{a} to \vec{b} . In our example, this is a model of the [KATRIN](#) experiment, which propagates a set of energy loss function parameters to a corresponding integral spectrum.

The output of this approach is a vector of central values \vec{b} , which represents the correlated uncertainties on \vec{b} originating from the uncertainties on \vec{a} . In [KATRIN](#) this translates to a mean integral spectrum and a corresponding covariance matrix. The MultiSim method proceeds in three steps [[Fra](#), [Hue](#)]:

1. A large number N sample set of parameters of interest is created by randomly varying \vec{a} according to a multivariate distribution using the covariance matrix M^a . Thus, correlated parameters are varied simultaneously.
2. All sample sets of correlated parameters \vec{a} are fed into the model, resulting in N samples of \vec{b} . In the example of the energy loss function uncertainty, this means a large number of integral spectra calculated with slightly different energy loss function parameterizations.
3. The covariance matrix M^b is finally calculated using the sample covariance

$$M_{ij}^b = \frac{1}{N-1} \sum_{k=1}^N (b_{ki} - \bar{b}_i)(b_{kj} - \bar{b}_j). \quad (5.9)$$

The mean of the sampled outputs \vec{b} , in the example the mean integral spectrum, is estimated by the sample mean

$$\bar{b}_i = \frac{1}{N} \sum_{k=1}^N b_{ki}. \quad (5.10)$$

²The name comes from the underlying idea: *Multiple* correlated parameters are varied simultaneously in *simulations* to generate sample sets.

Covariance matrices, which take uncertainties from uncorrelated parameters into account, can be calculated separately. Further on, they are added to the total covariance matrix, which takes all independent systematic effects into account.

$$M^b = M^{b_1} + M^{b_2} + \dots \quad (5.11)$$

5.4.2 Convergence Criteria

The sample mean and sample covariance, determining the covariance matrix in 5.9 and 5.10, are consistent estimators, in case the true mean and covariance exist. According to the weak law of large numbers, they converge for $N \rightarrow \infty$ to their true values [Bra14, Cow98]. In practice, however, it is not possible to calculate an infinite number of samples. Therefore, a criterion is required, which determines the minimal number of samples N needed to obtain reliable estimates.

A method to test the sample covariance matrix series for convergence is the Cauchy Convergence Test [BK00]

$$\forall \varepsilon > 0, \exists N_0 \in \mathbb{N}, \forall k > 0, \|M_{N_0+k} - M_{N_0}\| < \varepsilon. \quad (5.12)$$

In words this means that the sample covariance matrix M_N is constructed using N samples. It converges for N_0 samples, when the covariance matrix doesn't change within the arbitrary precision ε when k additional samples are drawn. To investigate the convergence, the Frobenius norm

$$\|M\| = \sqrt{\text{Tr}(M^*M)} \quad (5.13)$$

is used. An example of a convergence test, using the Cauchy convergence criterion, is shown in figure 5.3 (left). For a small number of samples the Frobenius norm of the covariance matrix varies a lot as a function of samples. After about 500 samples, the fluctuations are decreasing rapidly. The convergence tests shows, that in this example at least 500 samples should be used to estimate the covariances. In case a higher precision is required, a more conservative number of more than 3000 samples should be used.

In addition to that, the fractional variance as a function of samples is displayed in figure 5.3 (right). The fractional variance is the sum of all matrix elements M_{ij} divided by their expectation values \bar{b} . Even though the absolute scale is different, fluctuations of the fractional variance decreases in a similar way as the Frobenius norm with increasing sampling size. Therefore both can be used to determine the required sample size.

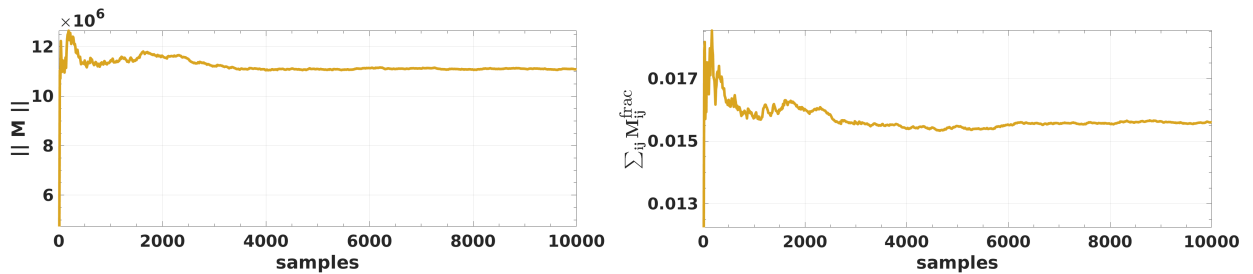


Figure 5.3: Convergence criteria to determine the number of samples. **Left:** Cauchy criterion, Frobenius Norm. **Right:** Fractional variance, sum of matrix elements M_{ij} divided by expectation values \bar{b} .

5.4.3 Fractional Covariance Matrix

Covariance Matrices are calculated, as described in 5.4.1, for a given scenario of central values of \vec{b} . In case some input parameters and therefore \vec{b} change, the covariance matrix has to be recomputed. In toy Monte Carlo (MC) studies or the analysis of similar data sets, this happens very often. Therefore it is beneficial to work with fractional covariance matrices, which are defined by

$$M_{ij} = M_{ij}^{\text{frac}} \bar{b}_i \bar{b}_j. \quad (5.14)$$

The fractional covariance matrix can be reused for a different set of central values \vec{b}' , in case \vec{b} and \vec{b}' differ only in their normalization [Hue]. In the case of KATRIN, scans of the tritium spectrum under similar conditions can be analyzed with the same fractional covariance matrices, even when the scans differ in their measurement time. Note that the covariance matrices in KATRIN, describing systematic uncertainties, which affect only the signal electrons, have to be normalized with the expected integral spectrum without background. A covariance matrix, which describes the uncertainty on the background, has to be normalized with the integral background spectrum accordingly.

An other application of fractional covariance matrices is within the fit itself, in which the covariance matrix is updated in every fit iteration according to the current estimation of \vec{b} .

5.4.4 Decomposition of Covariance Matrices

When only the shape and not the rate of a data set is analyzed, all normalization uncertainties have to be eliminated from the covariance matrices. The neutrino mass in the KATRIN experiment, for example, is determined with the shape of the integral tritium spectrum. The MC prediction is normalized to the data, by introducing the normalization as a free fit parameter. The so called *shape-only* covariance matrix, comprising only shape uncertainties, is extracted from the full covariance matrix as follows:

1. N samples of \vec{b} are calculated by drawing randomly from a multivariate Gaussian distribution with the full covariance matrix M^b . In KATRIN, this translates to N sample integral spectra.
2. Each sample of \vec{b} is normalized with the ratio of the total number of expected entries to the total number of entries within the samples

$$\vec{b}_{\text{shape-only}} = \vec{b} \cdot \frac{\sum_i \bar{b}_i}{\sum_i b_i}. \quad (5.15)$$

That means for KATRIN, that all sample integral spectra are renormalized to the statistics of the mean integral spectrum.

3. The shape-only covariance matrix is calculating, using the sample covariance, from the $\vec{b}_{\text{shape-only}}$ samples.

5.5 Average of Correlated Parameters

In experiments similar measurements are often repeated multiple times. In the KATRIN experiment, for example, the integral spectrum is measured repeatedly. Each measurement can be analyzed on its own, each yielding a result of the parameter of interest y_i . Eventually, it is desired to combine these results and quote only one average value y and corresponding uncertainty σ .

The following section describes with the example of run combination in the KATRIN experiment, how uncorrelated and correlated measurements can be combined.

Combining Uncorrelated Measurements

In the KATRIN experiment, one measurement of one integral spectrum corresponds to one run. All N runs can be fitted independently, yielding N values y_i of the parameter of interest, for example the endpoint of the β -spectrum, and N associated uncertainties σ_i . In the absence of systematic effects, the runs are independent from each other

and the uncertainties σ_i are uncorrelated. In this case, the average value y and its uncertainty σ can be estimated with the least squares (LS) estimators \hat{y} and $\hat{\sigma}[y]$, commonly known as weighted average (eq. 5.16) and standard error of the mean (eq. 5.17).

$$\hat{y} = \frac{\sum_{i=1}^N y_i / \sigma_i^2}{\sum_{j=1}^N 1 / \sigma_j^2} \quad (5.16)$$

$$\hat{\sigma}^2[y] = \frac{1}{\sum_{i=1}^N 1 / \sigma_i^2} \quad (5.17)$$

Combining Correlated Measurements

When the run by run analysis includes systematic effects, the obtained y_i and σ_i are no longer uncorrelated, since the runs share common correlated uncertainties. In this case the measurements can be combined using the following estimators

$$\hat{y} = \sum_{i=1}^N w_i y_i \quad (5.18)$$

$$\hat{\sigma}^2[y] = \sum_{i,j=1}^N w_i V_{ij} w_j. \quad (5.19)$$

The weights w_i are given by

$$w_i = \frac{\sum_{j=1}^N (V^{-1})_{ij}}{\sum_{k,l=1}^N (V^{-1})_{kl}}. \quad (5.20)$$

The covariance matrix V , which is $N \times N$ of size, contains information on the uncertainties of each measurements and their correlation among each other. Equation 5.21 shows the general pattern of a covariance matrix for N measurements. The diagonal elements contain the total variance σ_i^2 of each individual measurement, i.e. the correlated and the uncorrelated part, whereas the off diagonal elements embody only the correlated uncertainties. Mathematically this is expressed as the covariance $cov(y_i, y_j)$ with the correlation coefficient ρ [Cow98].

$$V = \begin{pmatrix} \sigma_1^2 & \rho \sigma_1 \sigma_2 & \dots & \rho \sigma_1 \sigma_N \\ \rho \sigma_1 \sigma_2 & \dots & \dots & \dots \\ \dots & \dots & \dots & \dots \\ \rho \sigma_1 \sigma_N & \dots & \dots & \sigma_N^2 \end{pmatrix} \quad (5.21)$$

With no straight forward statistical method available, the main challenge is the estimation of the covariance matrix V . Since this depends highly on the nature of the systematic effects considered, the concrete estimation of V , describing the run to run correlations in the KATRIN experiment, is performed in the data analysis chapter 7.5.1.

Apart from averaging over runs, another noteworthy scenario is when multiple analyses are performed with a partly shared data set. In the KATRIN experiment, this applies in the investigation of the parameter evolution as a function of fit range (section 7.4.2). Suppose, the measurement has n data points. The measurement result y_i is determined using n_i of these data points and the result y_j uses n_j . In this case the covariance is found to be

$$cov[y_i, y_j] = \frac{c}{\sqrt{n_i n_j}} \cdot \sigma_i \sigma_j \quad (5.22)$$

with the number of common data points c .

Chapter 6

Assessment of Systematic Uncertainties

This chapter describes the assessment of systematic uncertainties in the [KATRIN](#) experiment. Systematic effects, which are treated in this work, originate all along the way from the theoretical tritium spectrum to the integral spectrum measured by the [FPD](#). Starting at the theoretical tritium β -spectrum, uncertainties on the description of the molecular final states have to be taken into account (section [6.2](#)). Additionally, small term theoretical corrections are neglected in this work, which also leads to systematic uncertainties (section [6.3](#)). In the [WGTS](#) uncertainties on the isotopologue concentration (section [6.4](#)) and on inelastic scattering processes are considered (section [6.5](#)). Systematic uncertainties on the energy resolution and background enter in the main spectrometer (sections [6.5](#) and [6.6](#)). Finally, the analysis strategy itself gives rise to a systematic uncertainty (section [6.7](#)).

This chapter is structured as follows: In section [6.1](#), some general remarks about the displayed covariance matrices are made to avoid repetitions later on. Starting from section [6.2](#), the systematic effects are presented. Every systematic effect has a dedicated section. At the beginning of each section, the origin of the corresponding systematic effect is described. Thereafter its assessment through a covariance matrix or a pull term is discussed.

6.1 General Remarks on Displayed Covariance Matrices

For clearer visualization, the magnitudes of some systematic effects are enhanced in the displays with respect to the target values in the Design Report [[A⁺b](#)]. The focus of this chapter is the assessment of each systematic effect, rather than the comparison of their magnitudes. The latter is done in detail in the data analysis of the first tritium campaign in chapter [7](#) as well as in the neutrino mass sensitivity studies in chapter [8](#).

All covariance matrices, except for the background covariance matrix, only describe systematic effects which influence the signal. Therefore, they concentrate on the energy region below the anticipated endpoint of $E_0 = 18575$ eV. Consequently, all entries above the endpoint are zero and thus not depicted in the following.

The fractional covariance matrices may have large entries in the vicinity of the endpoint, where the integral spectrum is close to zero. For the sake of visibility, the endpoint region is excluded in the fractional covariance matrix representations. It is important to note, that these large entries in the close vicinity of the endpoint do not affect the parameter inference with the χ^2 statistic, because the fractional covariance matrix is normalized with the integral spectrum in the fit according to eq. [5.14](#).

All covariance matrices, displayed in this section, are calculated using the *Flat60 MTD*, shown in appendix [A.1](#), if not explicitly noted otherwise.

Furthermore, all covariance matrices, which are estimated with the MultiSim method, are tested for convergence, shown in appendix [B.1](#).

6.2 Molecular Final State Distribution

Description of Systematic Effect

Neutrino mass experiments, using gaseous T_2 sources in the 1980s, demonstrated the importance of an adequate knowledge and uncertainty estimation of the molecular final state distribution (FSD). The experiments at Los Alamos National Laboratory (LANL) and Lawrence Livermore National Laboratory (LLNL) both obtained a signal excess near the endpoint region, which translates into large negative neutrino mass squared. This excess was significant to the 2σ level at LANL [R⁺], and due to improved statistics even at the 6σ level at LLNL [SD]. Both analysis were performed with the description of the final states by Fackler *et al.* [F⁺85]. However, when reevaluating the results using the state of the art FSD calculations by Saenz *et al.* [SJF], the negative neutrino masses are eliminated for both experiments [BPR]. On the one hand this is an impressive experimental confirmation of the theoretical calculation by Saenz *et al.*. On the other hand this emphasizes the need of a reliable error estimation of the FSD calculations, especially with the enhanced sensitivity of the KATRIN experiment.

Uncertainties regarding the final state distribution in the KATRIN data analysis can be divided into three origins. Firstly, uncertainties emerging from the theory describing the molecular β -decay through the use of approximations e.g. the sudden approximation. Secondly, uncertainties coming from the lack of adequate theoretical calculations or measurements for the scenario at hand, e.g. precise calculations for higher excited states or the electronic continuum for measurements far below the endpoint. Thirdly, experimental uncertainties on input parameters for the FSD, mainly the isotopologue concentrations, have to be taken into account. While the former can be monitored independently by LARA and thus uncertainties can be quantified, it is even more challenging to state quantitative uncertainties on theoretical calculations. For this reason these two kinds of systematics are separated. This work focuses on the uncertainties on the theoretical final state distribution.

The FSD for T_2 has been calculated both by Fackler *et al.* [F⁺85] and later by Saenz *et al.* [SJF]. The FSD from Saenz *et al.* is depicted in figure 3.4. As discussed by Bodine *et al.* [BPR] the difference between the calculations for the ground state is found to be very small. Deriving the ground state probability distribution in a semi classical model using mainly zero-point motion as the origin of the ground state broadening, yields a variance of the ground state distribution, that agrees within 4% to *ab initio* theoretical calculations [BPR]. This gives confidence that the ground state distribution is well understood.

In the KATRIN Design Report [A⁺b] an uncertainty on the variance of the ground state of 1% is stated as a goal, which will be taken as a reference point. The normalization uncertainty of ground to excited state population is assumed to be 1% as well. Since KATRIN was originally supposed to measure only down to about 30 eV below the endpoint, excited states don't play a major role in the systematic uncertainty budget in the KATRIN Design Report. However, due to the enhanced background level, an extension of the measurement range towards energies further below the endpoint, entering the energy regime of the excited states, is planned. Therefore it is even more important to point out, that the calculations for higher excited states as well as for the electronic continuum differ substantially from one computation to another and make a proper treatment of the arising systematic uncertainty crucial [BPR]. After the suggestion of [Rob18] an uncertainty of 2-3% on the variance of the FSD for the whole energy range is assumed.

FSD Covariance Matrix and Pull Term

There are two different strategies to include the systematic uncertainty on the molecular final state distribution. Firstly, the correlated normalization uncertainty and the bin-to-bin uncorrelated uncertainty can be incorporated in a covariance matrix, which is described in the first part of the following section. Secondly, the normalizations of ground and excited states can be included as fit parameters. In that case, the covariance matrix is reduced to the bin-to-bin uncorrelated uncertainty of the FSD, whereas the normalization uncertainty is included in the form of a pull term. This approach is discussed in the second part of the following section. The FSD covariance matrix is constructed out of a large sample of integral spectra. Each sample spectrum is calculated with a FSD, which is randomly drawn out of a pool of sample FSDs. These sample FSDs are calculated by varying the normalization between ground state and excited states with respect to their theoretical values according to a Gaussian distribution with a standard deviation of 1%. Additionally bin-to-bin uncorrelated Gaussian fluctuations are applied to the

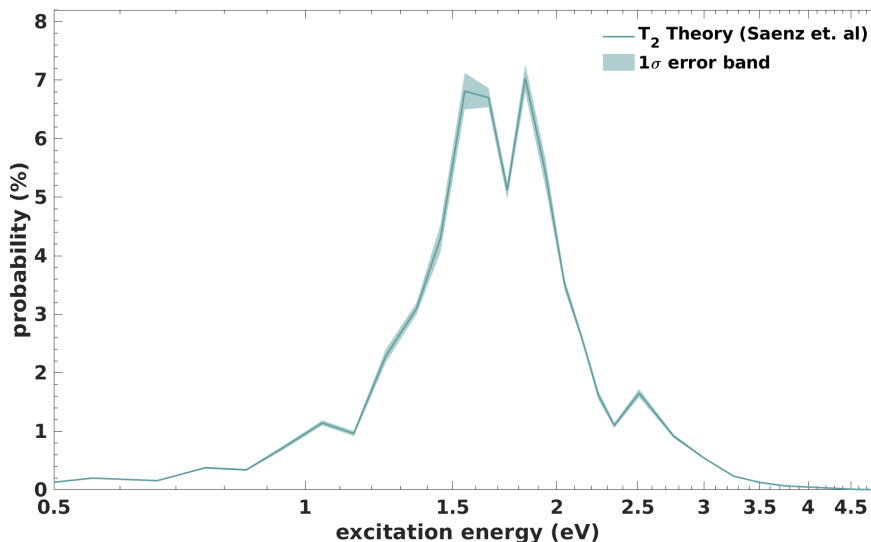


Figure 6.1: 1σ uncertainty band for the ground state distribution for T_2 . The normalization of ground to excited states probability is varied within 1%. The bin-to-bin uncorrelated Gaussian fluctuation of the ground state σ_{Fluct} is 4%, which corresponds to a variation in the variance of the ground state σ_{FSD} of 1.1%.

FSD, keeping the normalization over the complete energy range to one. The intensity σ_{Fluct} of these bin-to-bin uncorrelated fluctuations is chosen as such that the width of the **FSD**, represented by its variance, are distributed with a standard deviation σ_{FSD} of 1% for the ground state and of 2-3% for the whole **FSD**. Figure 6.1 depicts the uncertainty band (1σ) for the ground state, within which the sample spectra are varied. The uncertainty band for the whole spectrum can be found in the appendix B.2.

The intensity σ_{Fluct} of the bin-to-bin uncorrelated fluctuations for the ground state is determined by increasing σ_{Fluct} stepwise from 1-6%, while keeping the normalization uncertainty fixed to 1%. Figure 6.2 (left) shows the distribution of the **FSD** widths σ^2 for a fluctuations intensity σ_{Fluct} of 4%. Sampling with the respective fluctuation intensity results in a mean value of 0.192 eV^2 and a relative standard deviation of $\sigma_{FSD} = 1.1\%$. The evolution σ_{FSD} as a function of fluctuation intensity is shown in figure 6.2 (right). Aiming for an uncertainty on the width of the **FSD** σ_{FSD} of 1%, the bin-to-bin uncorrelated uncertainty for the ground state results to be between 3.5 and 4%. The same procedure is repeated for the whole **FSD**, including the excited states. The normalization uncertainty is fixed again to 1% and in addition to that the σ_{Fluct} of the ground state distribution is bound to 4%. For the determination of σ_{Fluct} for the excited states, σ_{Fluct} is varied between 1% and 30%.

Figure B.2 (left) displays the variance distribution for a fluctuation $\sigma_{Fluct} = 20\%$ and figure B.2 (right) quantifies the σ_{FSD} dependence on σ_{Fluct} . In order to obtain an uncertainty between 2% and 3% on the width of the **FSD** for the whole energy range, the bin-to-bin uncorrelated fluctuation of the final state distribution has to be between 15% and 25%. For all following calculations, the normalization uncertainty is taken to be 1%, $\sigma_{Fluct} = 4\%$ for the ground state and 18% for the excited states. The resulting covariance and correlation matrices are depicted in figure 6.3.

Alternatively, the normalizations of ground state N_{GS} and excited states N_{ES} within the final state distribution can be introduced as two additional fit parameters. They are always fit jointly with a pull term on their sum

$$\chi_{\text{pulls}}^2 = \left(\frac{N_{GS} + N_{ES}}{\Delta(N_{GS} + N_{ES})} \right)^2 + \left(\frac{N_{GS}}{\Delta N_{GS}} \right)^2. \quad (6.1)$$

Since the **FSD** can be interpreted as the probability distribution function of populated states, it should sum up to 1. However, the sum of the theoretical **FSD** from [SJF] used in this work lacks about $2 \cdot 10^{-3}$. Therefore the uncertainty on the sum is assumed to be $\Delta(N_{GS} + N_{ES}) = 2 \cdot 10^{-3}$. The second pull term denotes the uncertainty on the normalization with $\Delta N_{GS} = 1 \cdot 10^{-2}$. Even though the two **FSD** fit parameters are inferred in the fit, they

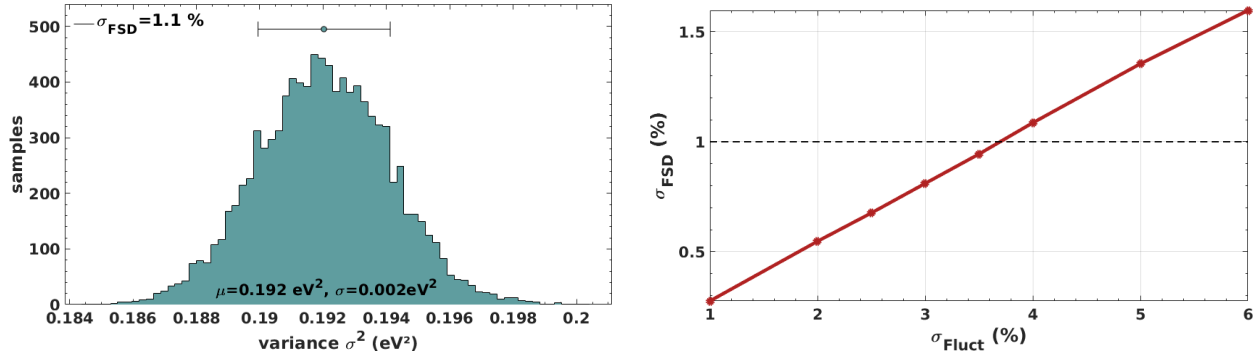


Figure 6.2: **Left:** Histogram of the ground state variance σ^2 for 10,000 samples. The normalization uncertainty from ground to excited states is 1%. The intensity of the uncorrelated Gaussian bin-to-bin fluctuation σ_{Fluct} is 4%. This results in a mean variance of the ground state of 0.192 eV^2 . The relative variation of this variance is 1.1%. **Right:** Standard deviation of the ground state variance σ_{FSD} as a function of σ_{Fluct} . In order to obtain an uncertainty of 1% on the ground state variance, the bin-to-bin uncorrelated uncertainty has to be between 3.5 and 4%.

do not contribute new degrees of freedom, because they are accompanied by the pull term described above. If not denoted otherwise, the FSD normalizations are fixed throughout this work.

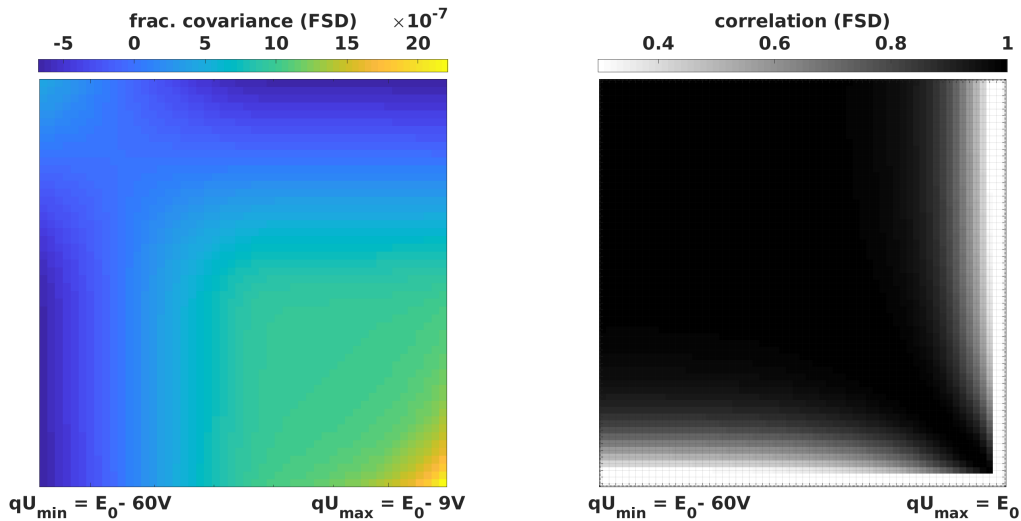


Figure 6.3: Molecular final states. **Left:** Matrix representation of fractional shape-only covariance matrix M_{frac}^{FSD} . The measurement range is limited between 60V and 9V below the anticipated endpoint at $qU = 18575 \text{ V}$ for better visibility. **Right:** Matrix representation of correlation matrix for the whole signal range.

6.3 Theoretical Corrections

Description of Systematic Effect

As described in section 2.3.3, several theoretical corrections have to be applied to the differential spectrum. Since their inclusion may be computationally expensive, theoretical corrections are often neglected in the calculation

of the differential spectrum. When doing so, their exclusion is considered as a systematic uncertainty in the data analysis.

Theoretical Corrections Covariance Matrix

The covariance matrix for the theoretical corrections M^{TC} is determined by comparing the integral spectrum without any theoretical correction S^{NC} to the spectrum with the all corrections S^{TC} .

$$M_{ij}^{\text{TC}} = (S_i^{\text{TC}} - S_i^{\text{NC}})(S_j^{\text{TC}} - S_j^{\text{NC}}) \quad (6.2)$$

As can be seen in figure 6.4 (top), the difference is at order of $2 \cdot 10^{-4}$. The dominant contribution comes from radiative corrections. All other theoretical corrections have a minor impact between 10^{-13} and 10^{-8} , as can be seen in figure B.4 in the appendix. The covariance and correlation matrix is shown in figure 6.4 (bottom).

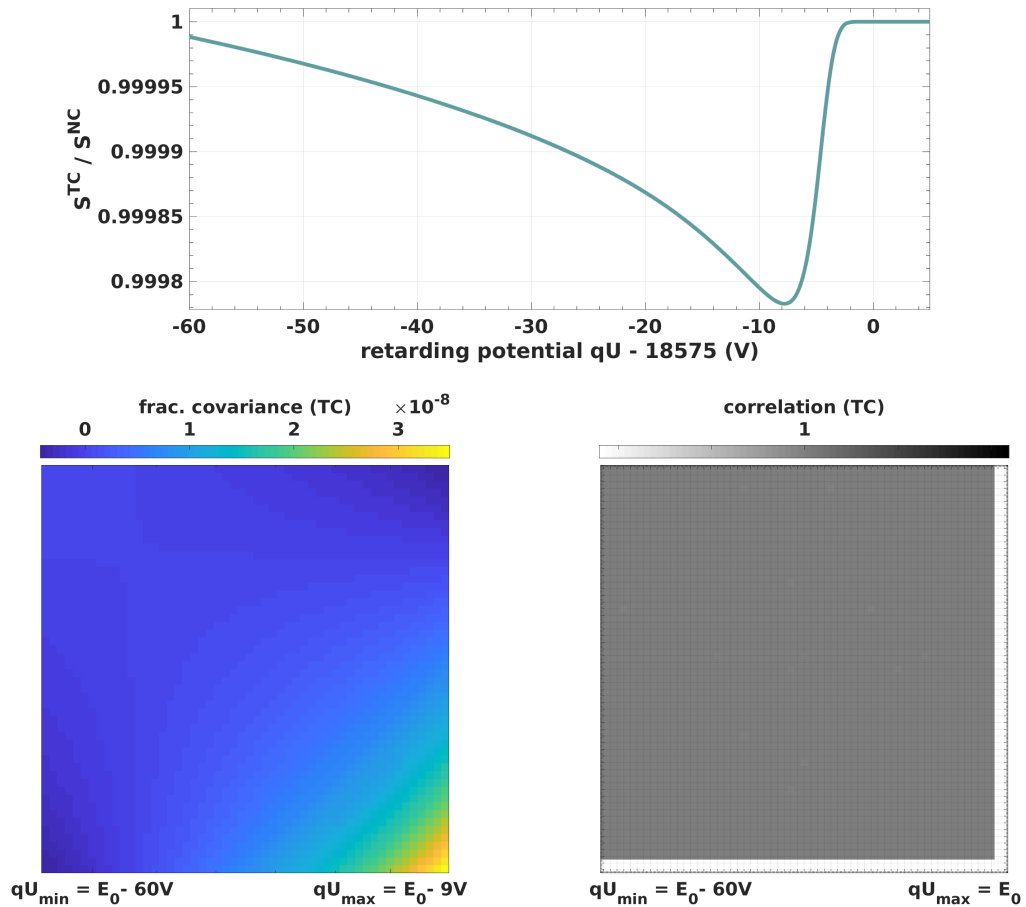


Figure 6.4: Theoretical Corrections. **Top:** Ratio of integral spectrum with theoretical corrections S^{TC} to spectrum without theoretical corrections S^{NC} . **Bottom Left:** Matrix representation of fractional shape-only covariance matrix M_{frac}^{TC} . **Bottom Right:** Correlation matrix for the whole signal energy range.

6.4 Tritium Activity Fluctuations

Description of Systematic Effect

The tritium activity inside the [WGTS](#) is directly proportional to the column density and the fraction of tritium nuclei, so called tritium purity. Activity fluctuations over the timescale from run to run, do not affect the neutrino mass sensitivity, because the normalization of the integral spectrum is a free fit parameter for each run. In contrast to that are activity fluctuations from within one run a systematic effect, which cannot be covered by the overall fit normalization. In case the activity fluctuations occur from subrun to subrun, that means from one retarding potential set point to the next on, they impose an uncorrelated systematic uncertainty on each qU bin. Since in most cases the column density stability is much better than the tritium purity stability, only the latter is considered in the construction of the corresponding covariance matrix. The isotopologue composition inside the [WGTS](#) is determined with [LARA](#).

TASR Covariance Matrix

Since the tritium activity fluctuations per subrun ([TASR](#)) impose an uncorrelated uncertainty on each measurement point, the sample spectra are calculated by introducing a bin-to-bin uncorrelated Gaussian variation on the integral spectra. The fractional shape-only covariance matrix is depicted in figure 6.5 (left). While the relative statistical uncertainty decreases with decreasing retarding potential, the fractional [TASR](#) covariance stays constant. Since the uncertainties are uncorrelated by design, the covariance matrix consists only of diagonal elements. The correlation matrix on the right of figure 6.5 confirms, that the [TASR](#) covariance matrix has no bin-to-bin correlations.

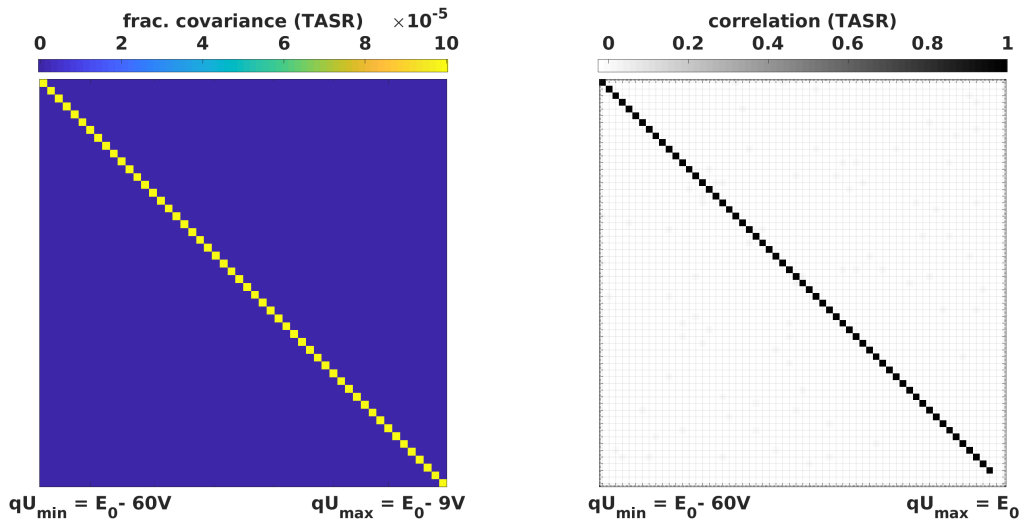


Figure 6.5: Tritium activity fluctuations per subrun. **Left:** Matrix representation of fractional shape-only covariance matrix M_{frac}^{TASR} for $\sigma_{TASR} = 1\%$. For the sake of visibility, the measurement range is limited between 60 V and 9 V below the anticipated endpoint at $qU = 18575$ V. **Right:** [TASR](#) correlation matrix for the whole energy range.

6.5 Response Function

Description of Systematic Effect

The response function describes transmission properties of the main spectrometer as well as inelastic scattering processes in the [WGTS](#). Being a complex function, a number of systematic uncertainties have to propagate through

it. The building elements of the response function are measurable quantities. Therefore, their uncertainty estimations are based on measurements performed with **KATRIN** and its predecessor experiment. In the following, the assessment of the response function's elements are shortly presented.

Magnetic Fields All three magnetic field uncertainties, namely the magnetic field in the analyzing plane ΔB_a , the magnetic field of the pinch magnet ΔB_{\max} and the magnetic field of the source magnet ΔB_{\max} enter in the transmission function (eq. 3.5). In addition to that, the ratio B_s/B_{\max} determines the maximal transmission angle θ_{\max} , which influences the inelastic scattering probabilities (eq. 3.6). Thus, both parts of the response function are affected by uncertainties on the magnetic fields.

Direct measurements of the magnetic fields inside the main spectrometer are not possible after the installation of the inner electrode system and the commissioning measurements of the main spectrometer at ultra-high vacuum [**E+**]. Therefore the magnetic fields have to be estimated with detailed simulations. As a basis for this, measurements inside the main spectrometer were conducted during the installation of the inner electrode system [**Rei13**]. Additionally, the magnetic field outside the main spectrometer can be measured with high-precision Bartington magnetometers, installed around the main spectrometer [**G+**]. Deviances between measurements and simulations provide a handle on the systematic magnetic fields uncertainties.

Column Density and Inelastic Scattering Cross Section The column density of the source ρd and the inelastic scattering cross section σ_{inel} affect the scattering probabilities. Since they always appear as the product $\rho d \cdot \sigma_{\text{inel}}$, their uncertainties are treated simultaneously. $\rho d \cdot \sigma_{\text{inel}}$ can be determined in different ways, for example by measuring the response function in dedicated electron gun measurements [**A+b**]. The mono-energetic electrons pass the **WGTS** and scatter inelastically on tritium gas. The scattering probabilities and thus $\rho d \cdot \sigma_{\text{inel}}$ can be inferred by comparing the rates, measured with the **FPD**, at different retarding potentials. Note, that a precise measurement of the energy loss function is needed before hand.

Energy Loss Function As described in section 3.2, two different parameterizations for the energy loss function are used in this thesis. While both measurements have been carried out at the "Troitsk ν mass set-up", different target molecules have been used. Aseev *et al.* observed scattering on gaseous T_2 , whereas Abdurashitov *et al.* investigated gaseous H_2 and D_2 . The fit result for the latter is averaged over the two isotopologues.

The parametrization formula is given in equation 3.9. The parameter values and their uncorrelated uncertainties are stated in table 6.1. The correlation matrix, only available for the Abdurashitov *et al.* parametrization, is depicted in figure 6.6.

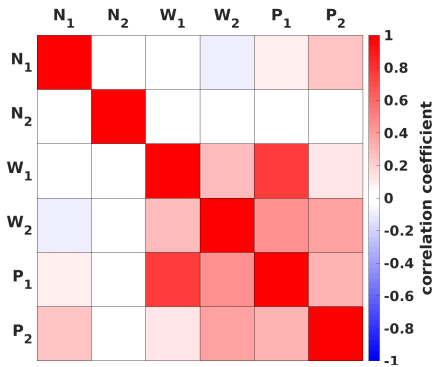


Figure 6.6: Correlation matrix for Abdurashitov *et al.* parametrization.

	Aseev <i>et al.</i>	Abdurashitov <i>et al.</i>
P_1	12.6 eV fixed	(12.695 ± 0.0017) eV
W_1	(1.85 ± 0.02) eV	(1.22 ± 0.05) eV
P_2	(14.30 ± 0.02) eV	(13.29 ± 0.18) eV
W_2	(12.5 ± 0.1) eV	(11.99 ± 0.13) eV
N_1	(0.204 ± 0.001) eV ⁻¹	(0.252 ± 0.0105) eV ⁻¹
N_2	(0.0556 ± 0.0003) eV ⁻¹	0.070 eV ⁻¹

Table 6.1: Energy Loss Function Parameters und Uncorrelated Uncertainties from Aseev *et al.* [**A+c**] and Abdurashitov *et al.* [**A+a**]

Response Function Covariance Matrix

The magnetic fields and $\rho d\sigma_{\text{inel}}$ are varied simultaneously according to Gaussian distributions. The standard deviation of each distribution is the corresponding uncertainty on the varied parameter. The sample distribution of magnetic fields strength B_s , for example, is depicted in figure 6.7 (left).

The correlated energy loss function parameters are varied according to their covariance matrix from a multivariate Gaussian distribution. Figure 6.9 (top) shows the energy loss function with 1σ -error band for up to ten scatterings using Aseev *et al.*. The two parameterizations are compared for the two scatterings in figure 6.9 (bottom). They differ not only in their central values, but also in their uncertainties. The uncertainties, estimated by Abdurashitov *et al.*, are larger than those from Aseev *et al.*. On the one hand this comes presumably from the fact, that the position of the excitation peak P_1 is a free fit parameter in Abdurashitov *et al.*, whereas it is fixed in Aseev *et al.*. On the other hand is the correlation matrix only available for Abdurashitov *et al.*. Therefore, the Abdurashitov *et al.* parametrization and uncertainty treatment is considered more reliable.

Sample response functions are calculated by randomly drawing sets of parameters. The 1σ -error band is shown in figure 6.7 (right). To illustrate the response function sampling, intermediate results, such as scattering probability and the transmission function sampling, is shown in appendix B.3. The response function uncertainties are further on propagated to the integral spectrum. The final covariance and correlation matrix, estimated with the sample integral spectra, is shown in figure 6.8.

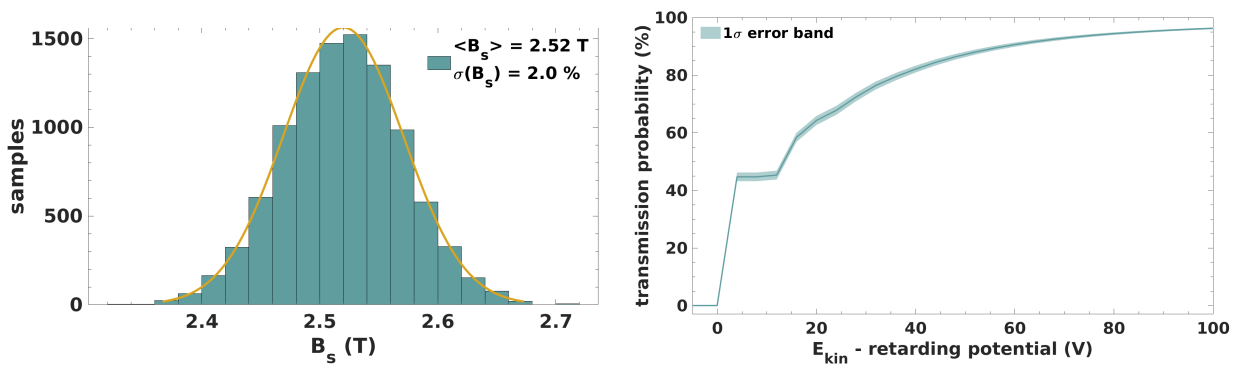


Figure 6.7: Left: Distribution of Sample B_s . Right: Response function with 1σ -error band. There is 2% uncertainty on the magnetic fields and 5% on $\rho d\sigma$.

6.6 Background

Description of Systematic Effect

During tritium measurements the background rate is determined by setting the retarding potential above the tritium endpoint. In this configuration tritium β -electrons aren't able to reach the FPD due to lacking energy. Consequently, only background electrons are detected. However, it isn't possible to measure the background rate for lower retarding potentials during tritium measurements. Dedicated background measurements showed that the background rate is vessel potential dependent [Har15]. Nevertheless, in the energy window, which is relevant for neutrino mass measurements, the background rate doesn't deviate significantly from the flat hypothesis [Blo18]. However, the statistical uncertainty on the background rate is large due to the low background rate. In this analysis a systematic uncertainty on the background is introduced, covering a possible deviance from the flat hypothesis. By design, this uncertainty is fully correlated from measurement point to measurement point.

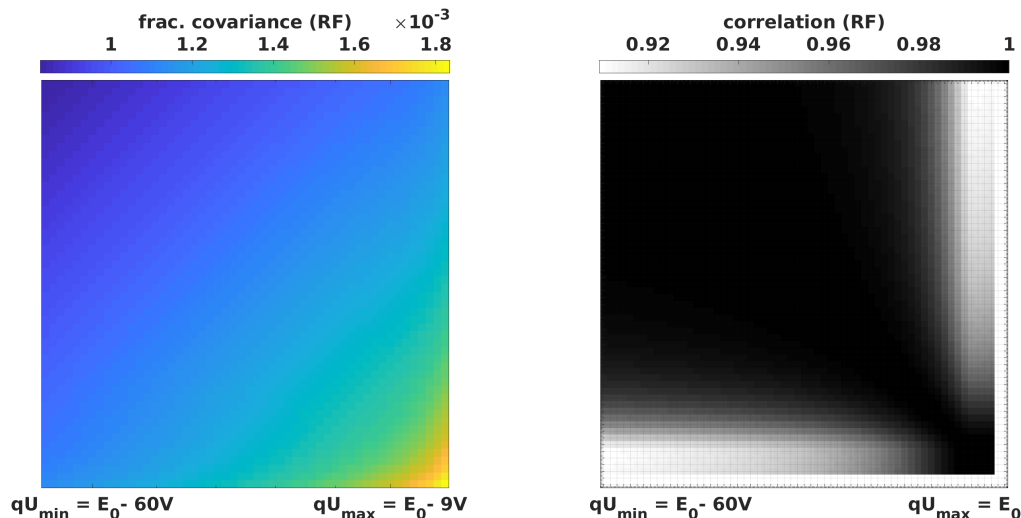


Figure 6.8: Response function. **Left:** Matrix representation of fractional shape-only covariance matrix M_{frac}^{RF} . There is 2% uncertainty on the magnetic fields and 5% on $\rho d\sigma$. The Abdurashitov *et al.* energy loss function uncertainties are used. Large entries in the close vicinity to the endpoint of the fractional covariance are excluded for better visibility by limiting the energy range to 9 eV below the endpoint. **Right:** Correlation matrix for the whole signal energy range.

Background Covariance Matrix

The background rate is determined solely using retarding energies above the anticipated endpoint. The background spectra are sampled by adding Gaussian fluctuations to a given background level. Every spectrum is further on fit using a linear regression allowing also for background slopes. Figure 6.10 depicts one sample spectrum and a fit to illustrate the sampling method. Fits, which result in negative background rates or which give a p-value of less than 5% are excluded from the sampling. The covariance matrix for the full energy range, shown in figure 6.11 (left), is estimated from the background fits using a sample estimator. This systematic uncertainty depends on the statistical error of the data points at retarding potentials above the endpoint. Therefore it decreases with cumulated measurement time. The two figures 6.11 (right) depict the background spectrum with a 1σ -error band for 45 days of measurement time.

Using the *Flat60* MTD, the systematic variation of the background is smaller than the statistical uncertainty, which makes this effect negligible. When measuring at retarding potentials far below the endpoint, as illustrated in the bottom right figure, even a small background slope leads to a significant variation in the background rate. In this case, the systematic uncertainty is even larger than the statistical. The MTD used for this calculation has been employed in the first tritium campaign. However, during the first tritium campaign the statistical uncertainty was much larger due to the reduced tritium activity and the limited measurement time of much less than 45 days. Therefore the uncertainty on the background slope was negligible with respect to the statistical uncertainty and other systematic effects as well.

6.7 Run Combination - Stacking

Description of Systematic Effect

To decrease the statistic uncertainty on the integral spectrum and to simplify the analysis, the spectra of N_r runs can be combined through stacking. As explained in section 4.3, this induces a systematic uncertainty due to small differences in the retarding potentials of the combined runs.

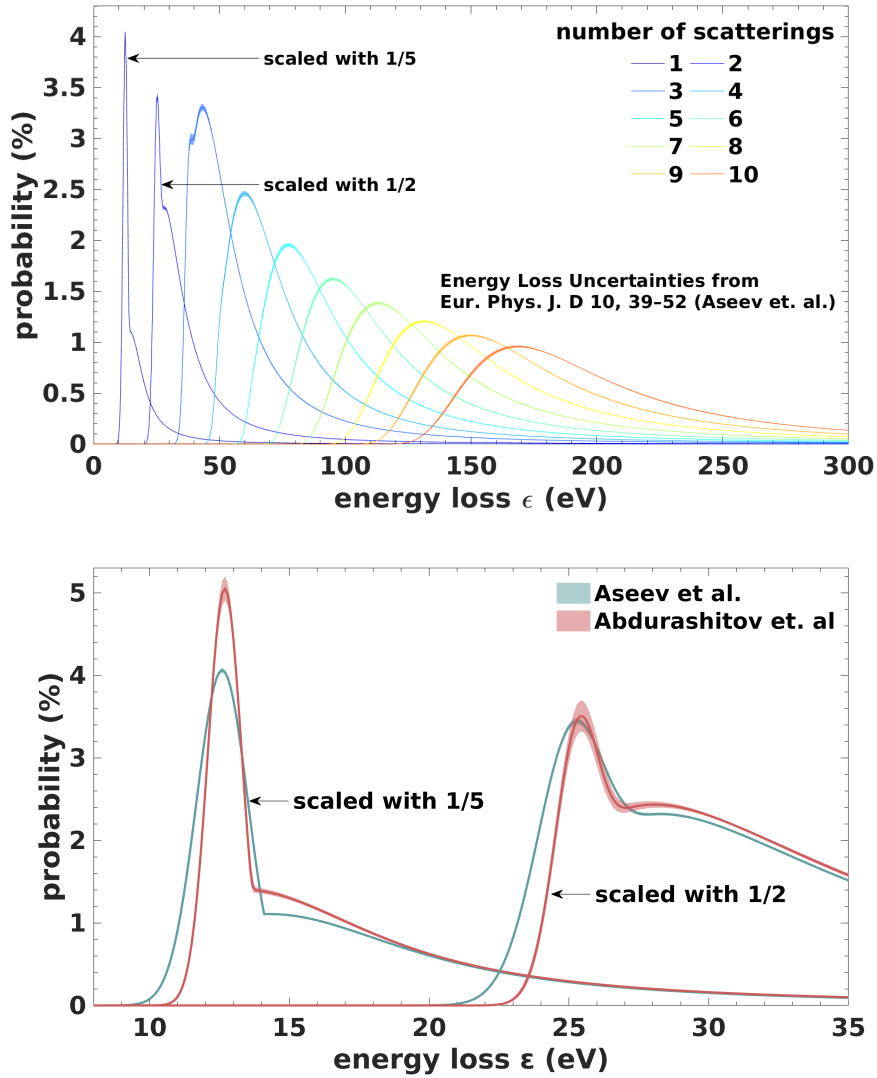


Figure 6.9: Top: Energy loss function with 1σ -error band. The Aseev *et al.* parametrization is used. **Bottom:** Comparison of the energy loss function parameterizations for two scatterings.

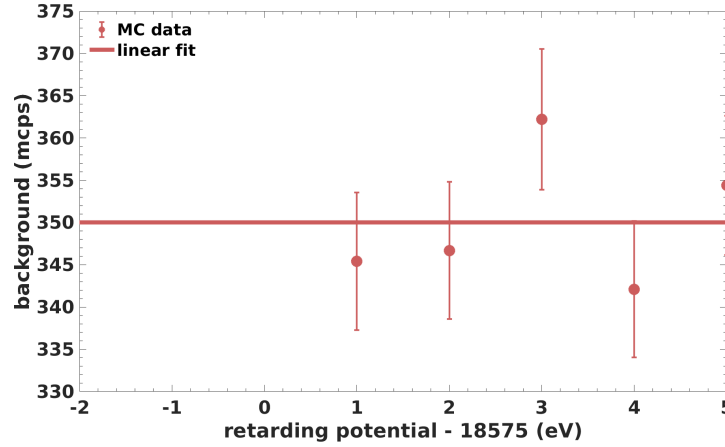


Figure 6.10: Example of background spectrum and fit. The MC data is generated by adding Gaussian fluctuations to a constant background rate of 350 mcps. Further on, the background spectrum is fit using a linear regression. In this example the background fit yields $B = (-2 \cdot 10^{-7} \cdot qU + 350)$ mcps.

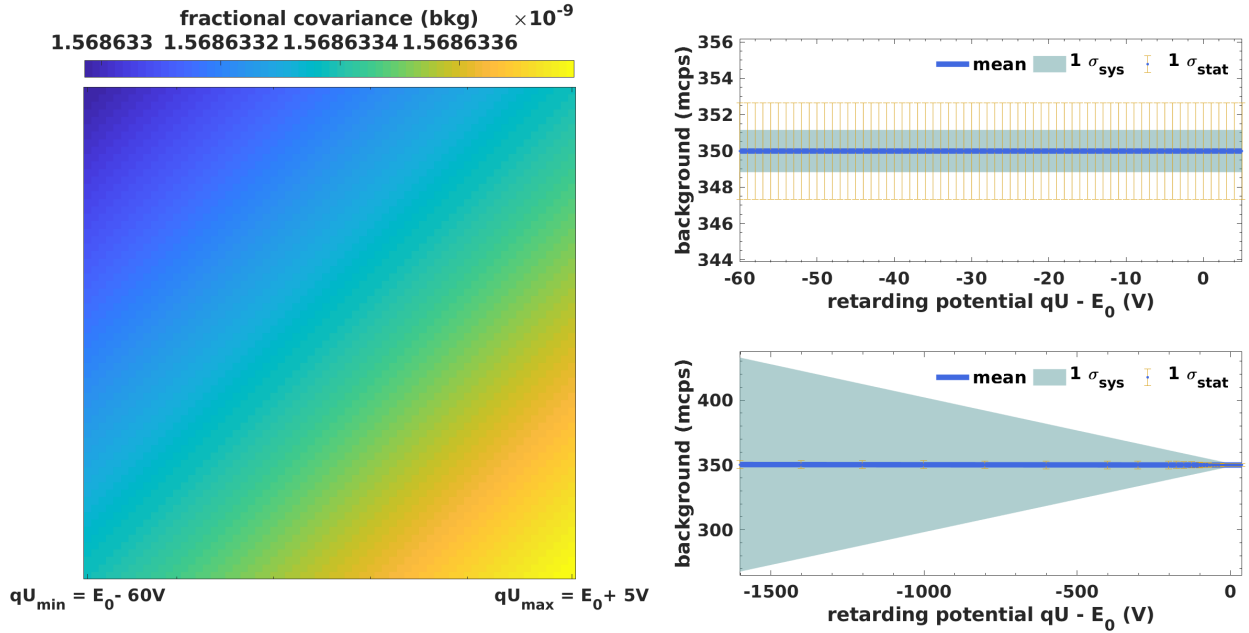


Figure 6.11: Left: Matrix representation of fractional covariance matrix M_{frac}^{Bkg} for the systematic uncertainty on the background rate for 45 days of measurement time using the *Flat60* MTD. Top Right: Integral background spectrum with 1σ -error band using the *Flat60* MTD. Bottom Right: Integral background spectrum with 1σ -error band using a MTD from the first tritium campaign. The smallest retarding potential reaches 1.6 keV below the endpoint.

Stacking Covariance Matrix

The stacking covariance matrix is calculated for a number of runs N_r , which shall be stacked. The retarding potentials are varied according a uniform distribution within a certain boundaries $[qU_{\min}, qU_{\max}]$. In addition to different qU , the runs also vary slightly in other parameters, for example in the column density. To take this into account, these parameters are randomly varied as well.

Further on, N_r integral spectra are calculated, randomly drawing sets of qU values. A sample stacked integral spectra is calculated by summing these N_r integral spectra. The fractional shape-only covariance matrix, determined with a large number of sample stacked integral spectra, is shown in figure 6.12. The only noteworthy entries lie on the diagonal. The off-diagonal terms are in the order of 10^{-9} . Therefore, run combination through stacking does not induce significant covariances. The correlation matrix on the right shows a checkerboard-like pattern in addition to a fully correlated diagonal.

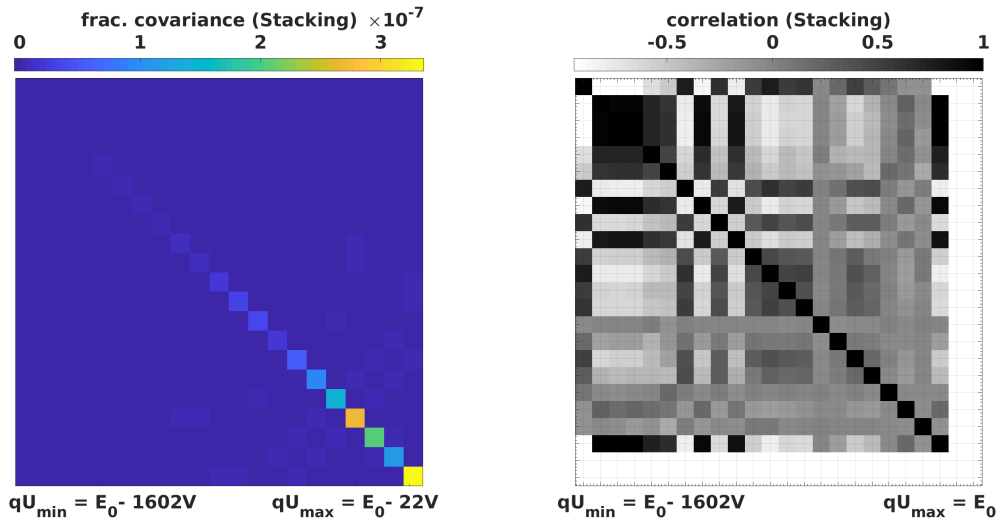


Figure 6.12: Run combination - stacking. **Left:** Matrix representation of fractional shape-only covariance matrix $M_{\text{frac}}^{\text{Stacking}}$. The **MTD** is **Right:** Correlation matrix for the whole energy range.

Chapter 7

First Tritium Campaign

The [KATRIN](#) experiment performed first commissioning measurements with tritium in 2018. Tritium gas was injected for the first time into the [WGTS](#) on May 18. This was followed by measurements of the integral β -decay spectrum from June 5 to June 20, referred to as *first tritium campaign*. This campaign had two main goals: Firstly, the demonstration of a global system stability to the 0.1% level and secondly, the investigation of the impact of systematic effects on the integral β -spectrum.

Due to the systematic uncertainty on the work function difference between the source and the main spectrometer ΔqU , an effective endpoint $E_{0,\text{eff}} = E_0 + \Delta qU$ is considered in this analysis. While the expected work function difference is zero, the uncertainty on the former is in the order of $|\Delta qU| \approx 0.5$ eV.

7.1 Description of Data

This work analyzes a set of runs¹ with similar operational parameters, for example the column density. In total 64 runs are studied with a cumulated measurement time of about 4.9 days. The column density inside the [WGTS](#) was approximately $4.56 \cdot 10^{17}$ molecules per cm^2 , which translates to 90% of its nominal value with respect to $[A^+b]$. In fully operational mode, i.e. nominal operational parameters, T_2 will be the dominant tritium isotopologue inside the [WGTS](#). However, in the tritium commissioning measurements, a different gas composition was employed due to the desired reduction of the tritium activity to 0.5% nominal activity. As stated in table 7.1, DT was the most abundant isotopologue. Due to hardware limitations, the magnetic field strengths of the source B_s and pinch magnet B_{max} were set to 70% of their nominal values. Table 7.1 summarizes all [KATRIN](#) parameters, which were not nominal during the first tritium campaign.

All operational parameters were stable over time within their specifications with respect to the [TDR](#). Figure 7.1 shows, for example, the measured column density over the course of 117 hours. The distribution of ρd has a relative standard deviation of as little as $1.5 \cdot 10^{-5}$, which exceeds its requirement by two orders of magnitude. The ρd values are provided by source pressure measurements coupled to a thermodynamical model. Even though they may not represent the true absolute ρd values, the relative fluctuations are quantitatively correct assuming the pressure measurements are fully representative for the whole [WGTS](#).

The two outer [FPD](#) rings are excluded from the data analysis, because they measure a significant decreased count rate compared to the remaining pixels, as shown in figure 7.2. According to $[A^+18b]$, this is caused by a slight misalignment of the flux tube. Being shadowed by the forward beam monitor, pixels 100, 112 and 123 are excluded as well.

The measurement time distribution ([MTD](#)), shown in appendix A.1, was specially designed for the first tritium measurements. The reduced tritium activity allowed measurements at retarding potentials up to 1602 eV below the anticipated endpoint, where the rate of the tritium β -spectrum is about five orders of magnitude higher than in the close vicinity of the endpoint. In future neutrino mass measurements with nominal tritium concentration

¹Reminder: A run, also referred to as scan, is one measurement of the integral tritium β -spectrum. An up scan is a run, which begins at retarding potentials far below the endpoint and ends with qU above the endpoint. Down scans have the reversed scan direction.

parameter	value
ρd	$4.56 \cdot 10^{17} \text{ mol/cm}^2$
B_s	2.52 T
B_{max}	4.2 T
B_a	6.3 G
energy resolution $\Delta E/E$	2.79 eV/18575 eV
amount of FPD pixels	121
DT mol. fraction	0.01
T ₂ mol. fraction	$\approx 10^{-5}$
HT mol. fraction	$\approx 10^{-4}$
MTD range	$[E_0 - 1602 \text{ eV}, E_0 + 38 \text{ eV}]$

Table 7.1: Average KATRIN parameters during the tritium commissioning measurements for all stable up and down scans with 90% column density. All other parameters are nominal. An overview of the nominal values is given in table 3.2.

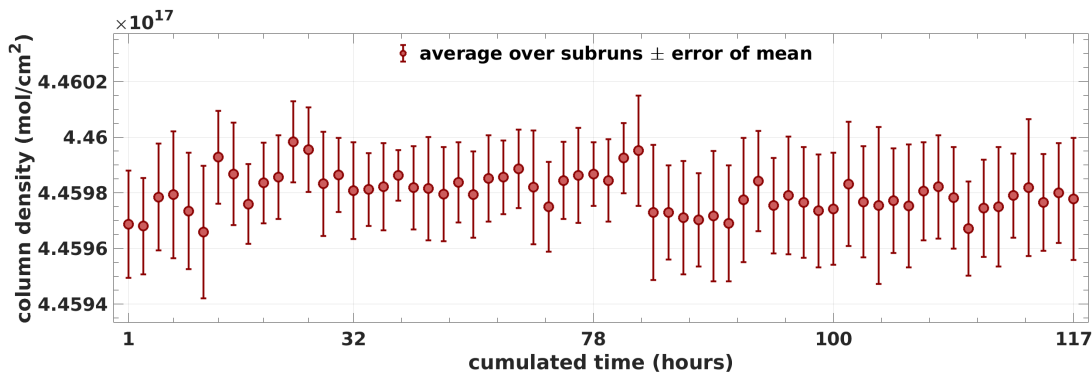


Figure 7.1: Column density as a function of measurement time. The column density is stable over the course of 4.9 days within $\sigma_{rel} = 1.5 \cdot 10^{-5}$.

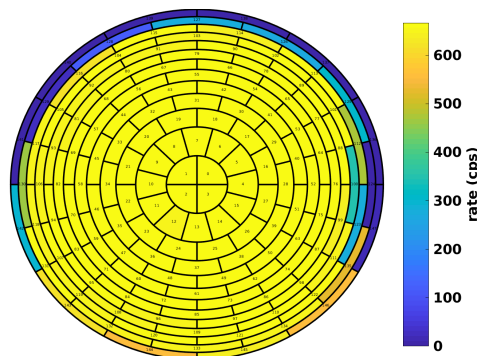


Figure 7.2: FPD pixel map. The pixelwise count rate for one run is depicted for a retarding potential of 1602 eV below the anticipated endpoint. Parts of the two outer rings and the pixels 100, 112 and 123 have a significant lower count rate than the rest of the FPD.

this will not be possible due to DAQ limitations. Additionally, the region far below the endpoint is significantly more affected by systematic effects. In theory, the same MTD was used for each run. In practice, the MTDs differ slightly in their retarding potential values from run to run. The mean standard deviation is 44 meV.

For some analyses in this work, only parts of the measured spectra are considered. The main three energy windows with respect to the anticipated endpoint are the long range $[-1600 \text{ eV}, +40 \text{ eV}]$, the medium range $[-400 \text{ eV}, +40 \text{ eV}]$ and the short range $[-200 \text{ eV}, +40 \text{ eV}]$.

7.2 Systematic Uncertainty Budget

The understanding of the KATRIN apparatus is not yet at its final level. Future commissioning measurements will improve the knowledge of the system continuously over the full measurement time. Therefore, the systematic uncertainty budget used in the data analysis of the first tritium campaign exceeds the design values from the TDR. Table 7.2 summarizes the relative systematic uncertainties on the effects considered. The uncertainties are motivated as follows:

1. Column density and inelastic scattering cross section:

As described in 6.5, column density ρd and inelastic scattering cross section σ_{inel} always appear jointly in the response function model. Therefore, future electron gun measurement will determine the product $\rho d \cdot \sigma_{\text{inel}}$ and its associated uncertainty simultaneously. However, since the electron gun was only installed after the first tritium campaign, this treatment cannot be applied with the data at hand. The uncertainties are therefore estimated separately for the first tritium measurements.

i) Column Density

As can be seen in figure 7.1, ρd is stable over time to a precision of $1.5 \cdot 10^{-5}$. However, the absolute value of the column density, cannot be determined with such an accuracy due to the lacking electron gun. The uncertainty on the absolute value of ρd is estimated to be 2.2% by the WGTS hardware group [BG19].

ii) Inelastic scattering cross section

The systematic uncertainty on σ_{inel} is conservatively estimated to be of 2%, based on the deviance of the two theoretical calculations from Liu in 1973 [Liu73] and 1987 [Liu87].

2. Energy loss function:

The treatment of the energy loss function uncertainty is presented in 6.5. The default energy loss function parametrization in the data analysis of this work is from Abdurashitov *et al.* [A+a].

3. Magnetic field strengths:

The uncertainty on the magnetic field strength in the analyzing plane B_a is assumed to be 1%, whereas the uncertainties on the fields of the two solenoid magnets B_s and B_{max} is estimated to be 2%. These estimates are based on the deviance of Kassiopeia² simulations to measurements of the high precision Bartington magnetometers near the analyzing plane [BB18].

4. Molecular final state distribution (FSD)

The treatment of the FSD uncertainty is presented in 6.2.

5. Tritium activity fluctuations per subrun (TASR)

The tritium fluctuations per subrun are assumed to be 0.5%, estimated by the LARA group.

6. Stacking:

The systematic uncertainty based on run stacking has a data driven input. The standard deviations of the qU distribution of the stacked runs is retrieved from the data files and passed to the covariance matrix calculation.

²Kassiopeia is a simulation package for the KATRIN experiment. It comprises the generation, tracking and detection of particles.

parameter	relative uncertainty
ρd	2.2%
σ_{inel}	2%
energy loss function	Abdurashitov <i>et al.</i>
B_a	1%
B_s, B_{max}	2%
FSD	1% normalization, 1%(2%) variance ground (+ excited) states
TASR	0.5%
theoretical corrections	ON / OFF
stacking	data driven

Table 7.2: Relative systematic uncertainties on main **KATRIN** input parameters for the first tritium campaign 2018.

7.3 Expected Sensitivity

The expected sensitivities on the neutrino mass and the endpoint are estimated using a toy **MC** simulation. The confidence intervals are constructed by with a fit to an Asimov data set with a χ^2 -statistic, described in section 5.2.2. Calculated for a measurement time of 4.9 days, the same operational parameters and the same systematics budget like the 64 analyzed runs, the sensitivities can be later on compared with the fit results of the data analysis. The medium energy range is considered.

As illustrated in figure 7.3 by the white dashed bar, the statistical neutrino mass sensitivity at 90% C.L. is about 4.4 eV. The broad stacked bar represents the neutrino mass sensitivities, when switching on one systematic effect after the other. The broad red bar, for instance depicts the sensitivity considering **TASR** uncertainties next to statistic uncertainties. The sensitivity of the broad yellow bar includes the **FSD** uncertainties on top of the former two and so on. Furthermore, the narrower bars show the impact of individual systematic effects, combined only with statistical uncertainties. The uncertainty due to the tritium activity fluctuations per subrun and the uncertainty on $\rho d \cdot \sigma_{\text{inel}}$ are the dominant systematic effects, exceeding even the statistical uncertainty.

The total neutrino mass sensitivity amounts to 6.2 eV at 90% confidence level. As the statistics of the first tritium commissioning is low with respect to the final one and the operational parameters, especially the column density, are not yet known at their targeted precision, the neutrino mass determination is not the goal of these measurements. Upon decision of the **KATRIN** collaboration, the neutrino mass is fixed to zero throughout the analysis of the first tritium data.

Furthermore, the sensitivity on the endpoint is calculated as shown in figure 7.4. The graphical representation is the same as in the previously presented neutrino mass sensitivity plot. Starting with a statistical sensitivity of 46 meV, the total sensitivity amounts to 224 meV. Consequently, the first tritium commissioning campaign is systematics dominated with respect to the endpoint. The largest contribution comes from the uncertainty on the product of column density and inelastic scattering cross section $\rho d \cdot \sigma_{\text{inel}}$. Second and third are the final state distribution and the magnetic fields. Of minor influence and therefore not displayed in figure 7.4 are uncertainties on the background slope and on the theoretical corrections.

The endpoint is the main physical parameter of interest in this analysis. Being strongly correlated to the neutrino mass, the endpoint is a good proxy to estimate the impact of systematic effects on the neutrino mass for future measurement campaigns.

7.4 Data Analysis with Statistic Uncertainties

Before investigating the impact of systematic effects on the β -spectrum, an analysis using only statistical uncertainties is performed. The χ^2 -formula in eq. 5.8, reduces therefore to

$$\chi^2 = \sum_i \frac{(x_i - \mu_i(m_\nu^2 = 0, E_{0\text{eff}}, N, B))^2}{\sigma_i^2} \quad (7.1)$$

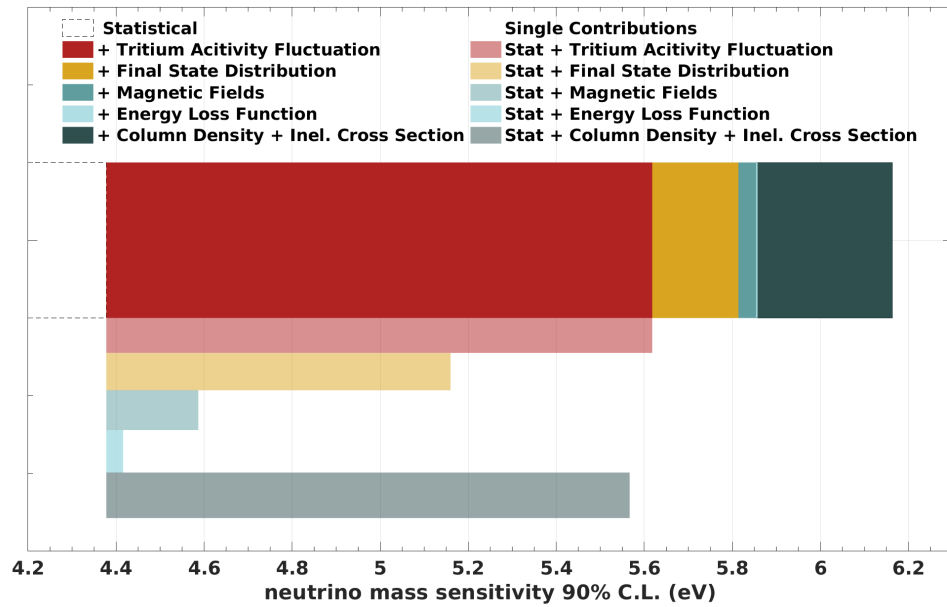


Figure 7.3: Neutrino mass sensitivity at 90% C.L. including systematic effects step by step. The total sensitivity is 6.2 eV.

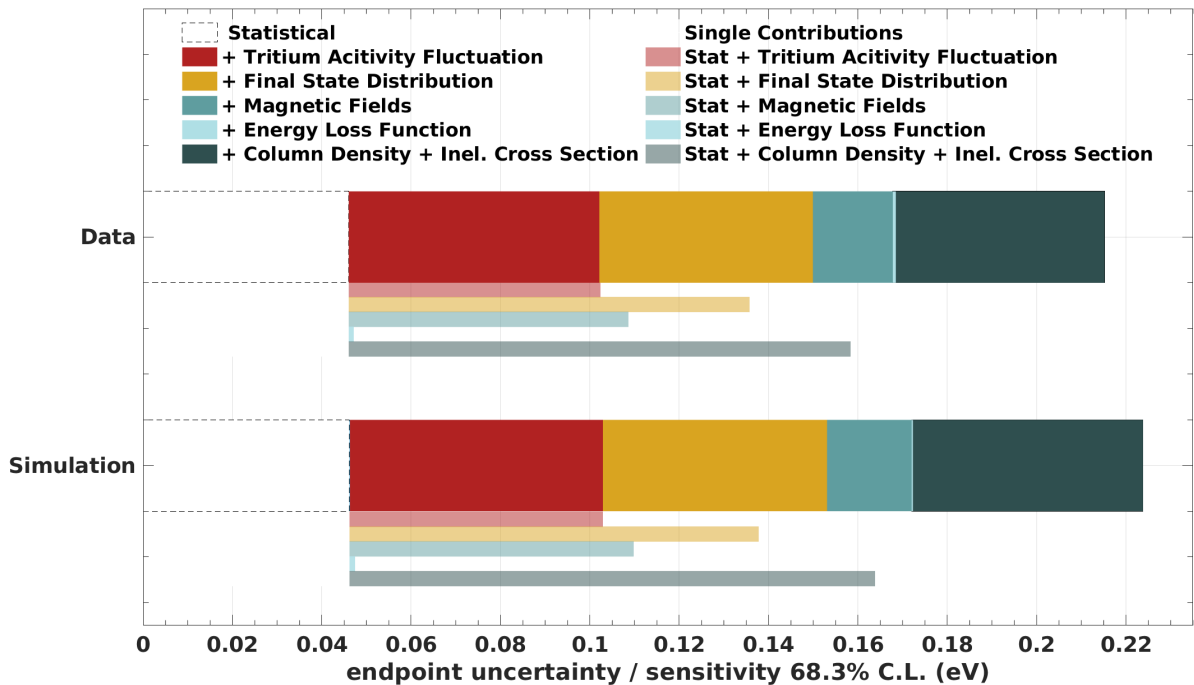


Figure 7.4: The lower bar shows the endpoint sensitivity at 1σ (68.3%) C.L., while the upper bars illustrates the 1σ -uncertainty on the endpoint inferred from data. Systematic effects are included step by step. The total sensitivity amounts to 224 meV. The total uncertainty is 214 meV.

with the statistical standard deviation $\sigma_i = \sqrt{x_i}$. Due to the low sensitivity on the neutrino mass, presented in section 7.3, m_ν^2 is fixed to zero throughout the data analysis.

An example of a fit to a single run using the medium energy range is shown in figure 7.5. Having a p-value of 0.82, the fit describes the data well and the residuals are distributed around zero without any pattern.

In the first part of this section the parameter stability of these single run fits as a function of measurement time is investigated. Thereafter, the parameter evolution with respect to the analyzed energy range is presented. Both sections conclude, that under some circumstances systematic effects have to be taken into account.

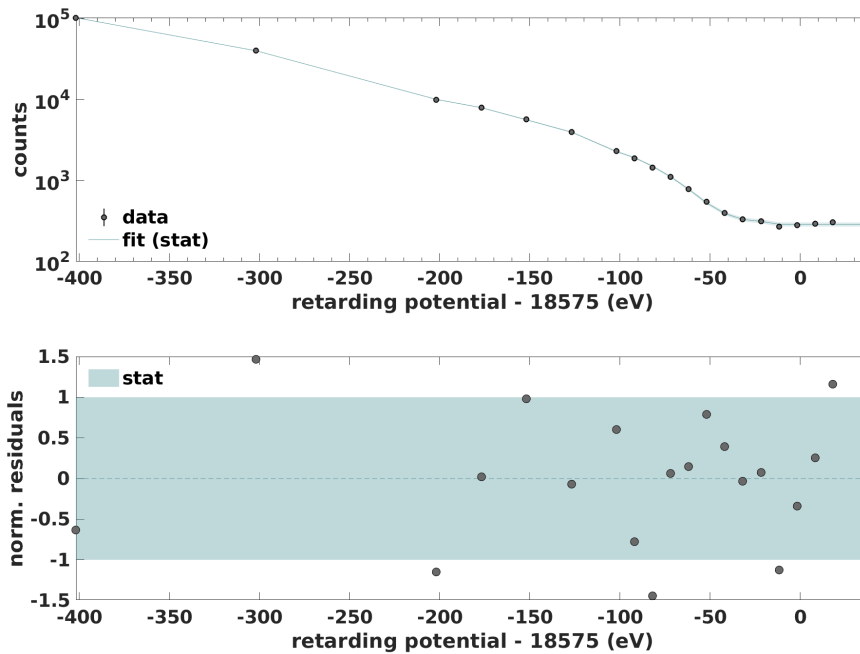


Figure 7.5: Example of a fit to one three-hour-run in the medium energy range using only statistical uncertainties. The small χ^2 of only 11.7 at 17 degrees of freedoms indicates, that the model describes the data well within statistical uncertainties.

7.4.1 Parameter Stability over Measurement Time with Statistic Uncertainties

To investigate the fit parameter stability over time, all runs are fit one by one using statistical uncertainties only. All three energy ranges are considered. The corresponding fit results for the medium energy range are shown in figure 7.6. No obvious trend over time is observed for any fit parameter. However, one run has a significantly higher background rate.

Furthermore, to quantify their stability, a constant is fit to each time evolution and the goodness-of-fit, using the χ^2 statistic, is calculated. As can be seen in table 7.3, the time dependencies of the effective endpoint and the background rate are consistent with statistical fluctuations for all energy ranges. However, the p-value for the effective endpoint decreases from short to medium range. In contrast to that, the goodness-of-fit for the background rate is roughly constant. Since the background rate is mostly determined by measurements at retarding potentials above the endpoint, the extension to larger energies ranges doesn't alter the fit result significantly.

The p-value for the signal normalization drops drastically from short to long range. Being especially sensitive to fluctuations of the tritium activity, a slightly different *true* molecular DT concentration or column density than the input value leads to a normalization factor, which differs significantly from unity, due to the very high number of counts. In case the deviation between actual and expected tritium activity is different from run to run, the

normalization factor is not stable over time. Being most sensitive to the normalization, the long range reflects this instability the strongest in its p-value. On the one hand, when the deviation between actual and expected tritium activity originates solely from the DT concentration, this bias affects only the normalization of the integral spectrum. Since all information on the endpoint is comprised in the shape of the integral spectrum, this systematic bias does not alter the endpoint sensitivity. On the other hand, when the instable normalization factor comes from a systematic uncertainty on the column density and therefore on the inelastic scattering inside the WGTS, the shape of the integral spectrum is affected. Presumably, the unstable normalization factor originates from a systematic uncertainty on the molecular DT concentration, because the former had a nominal value of only 0.5%. The LARA system, which monitors the isotopologue concentration, is not designed to measure at such low concentrations.

	200 eV		400 eV		1600 eV	
	χ^2 (63 dof)	p-value	χ^2 (63 dof)	p-value	χ^2 (63 dof)	p-value
$E_{0,\text{eff}}$	49.6	0.89	64.5	0.42	64.4	0.43
B	74.6	0.15	76.5	0.12	72.2	0.20
N	55.4	0.74	75.6	0.13	≈ 7000	0.00

Table 7.3: Goodness-of-fit with the χ^2 statistic. A constant is fit to each parameter as a function of measurement time. The run-wise variations of effective endpoint $E_{0,\text{eff}}$ and background rate B are consistent with statistical fluctuations for all energy ranges. The time evolution of the signal normalization N requires the consideration of systematic uncertainties.

7.4.2 Parameter Stability over Measurement Range with Statistic Uncertainties

To check the parameter stability over analyzed measurement range, the three fit parameters are determined multiple times using different energy ranges using only statistical uncertainties. All 64 runs are combined through stacking. Therefore, the statistic in this analysis corresponds to approximately 4.9 days of measurement time. The upper limit of the analysis window is fixed to 38 eV above the endpoint, whereas the lower energy limit can take values between 1602 eV and 127 eV below the endpoint. Figure 7.7 depicts the fit results as a function of lower energy limit.

Firstly, the p-values in the bottom right plot demonstrate, that statistical uncertainties are not sufficient to cover the deviances in fits using the longer energy ranges. Further then 177 eV below the endpoint, the p-values are below the critical value of 5%.

Secondly, the effective endpoint and the signal normalization show a strong energy range dependence. Both are rather flat for the long ranges. For energy ranges with a lower limit of less than 300 eV below the endpoint, the curves show a rapid increase or decrease. As explained previously, the background rate doesn't have such a strong fit energy range dependence. To quantify this instability over energy range, a constant is fit to each parameter evolution and the goodness-of-fit is calculated. Since each energy range shares partly the same data, the fit results are strongly correlated. The corresponding correlation matrix is calculated according to equation 5.22 and is depicted in appendix C.2. Table 7.4 confirms that the variations of the effective endpoint and the signal normalization as a function of energy range are not consistent with statistical fluctuations.

To conclude, both the small p-values for the large energy ranges as well as the strong energy range dependence of the fit results demonstrate, that systematic effects have to be taken into account for energy ranges, which reach further than 177 eV below the endpoint.

7.5 Data Analysis with Statistic and Systematic Uncertainties

The previous section concludes, that the fit parameter evolutions as a function of measurement time and range are inconsistent with statistical fluctuations for large energy ranges. To resolve these inconsistencies and to perform a more adequate analysis, systematic uncertainties are taken into account in the following sections.

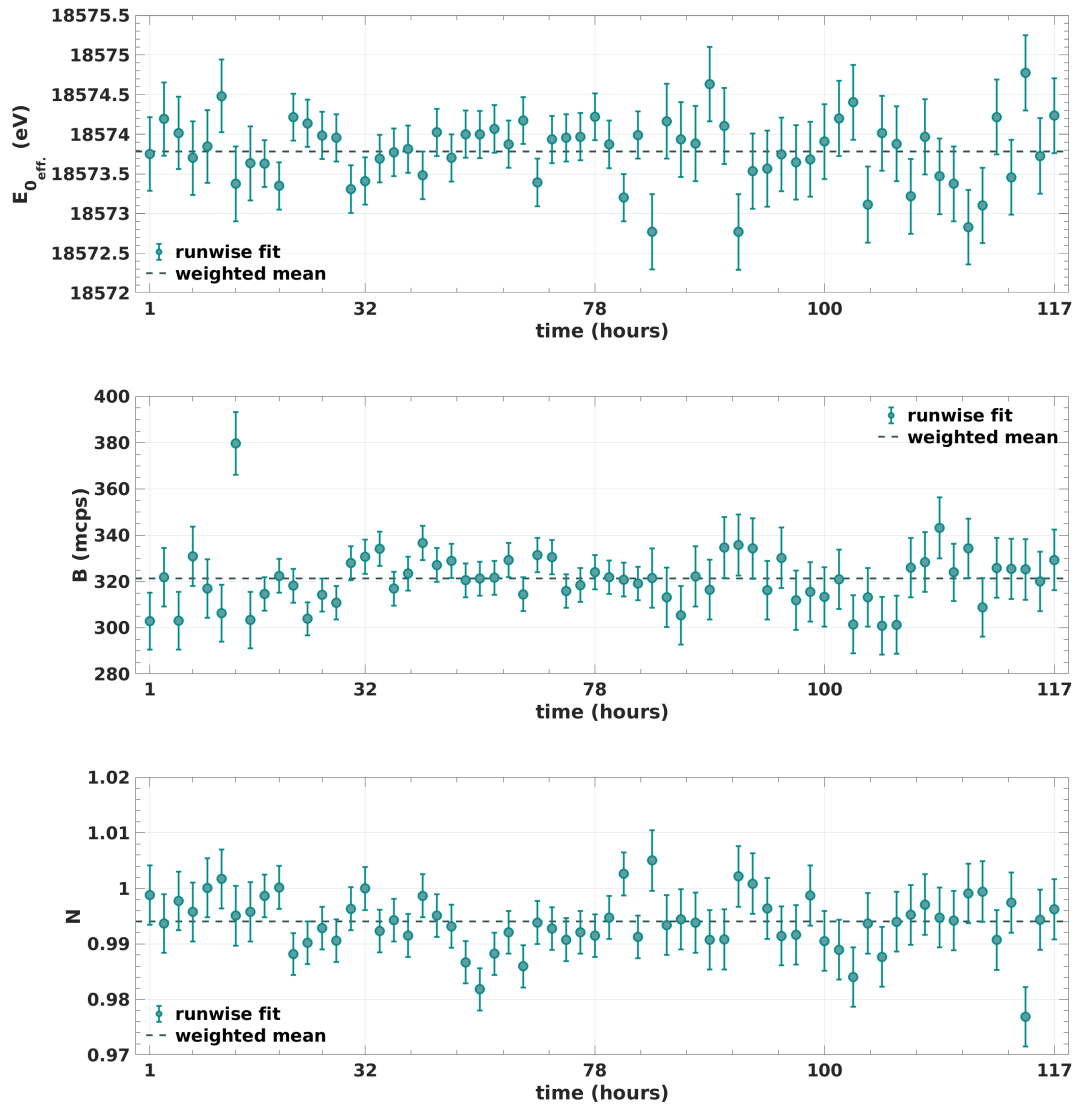


Figure 7.6: Stability of statistical fit results over time for the 400 eV range. **Top:** Effective endpoint. **Center:** Background rate **Bottom:** Signal normalization

	χ^2 (11 dof)	p-value
$E_{0\text{eff}}$	289	0.00
B	12.7	0.31
N	738	0.00

Table 7.4: Goodness-of-fit test with the χ^2 statistic. A constant is fit to all parameter evolutions in figure 7.7 using the correlation matrix depicted in appendix C.2. The variations of effective endpoint and normalization as a function of energy range are not consistent with statistical fluctuations.

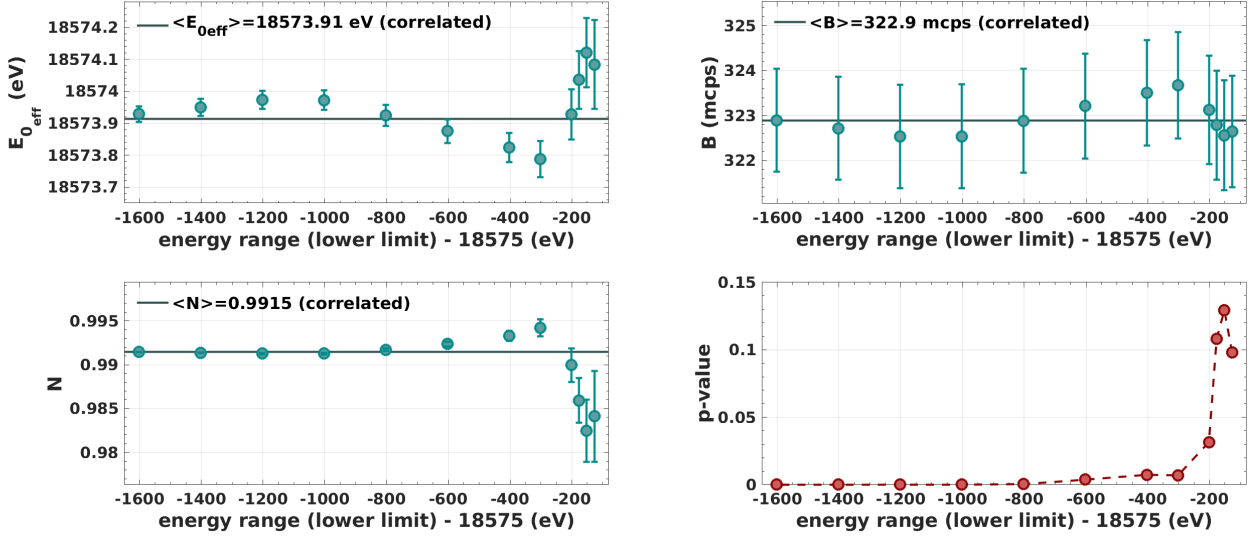


Figure 7.7: Fit results of the effective endpoint, background rate, signal normalization and the corresponding p-value as a function of energy range. The upper threshold of the analyzed energy window is fixed to 38 eV above the endpoint, whereas the lower threshold takes values between 1602 eV and 127 eV below the endpoint. The effective endpoint and the signal normalization show a strong energy range dependence.

7.5.1 Parameter Stability over Measurement Time including Systematic Uncertainties

The parameter stability over measurement time including systematic effects is investigated. Figure 7.8 shows the evolution of the effective endpoint over the course of 117 non-consecutive hours for the medium measurement range. The corresponding plots for the background rate and signal normalization can be found in appendix C.3. The variations over time are quantified by a goodness-of-fit test, calculating the deviances between the single fit results and the weighted average according to eq. 5.18.

In contrast to the analysis using only statistic uncertainties, the runwise fit results are correlated due to their common systematic uncertainties. This has to be taken into account when combining the fit results. Next to statistical uncertainties, systematic uncertainties arising from tritium activity fluctuations per subrun are fully uncorrelated from run to run. In contrast to that, systematic uncertainties originating from the FSD and theoretical corrections are fully correlated from run to run. Furthermore, systematics from the response function, that means column density, inelastic scattering cross section, magnetic fields and energy loss function, lead to partly correlated uncertainties.

The covariance matrix V in eq. 5.21, describing the run to run correlations, is split into a fully uncorrelated and partly correlated part

$$V = V_{\text{fu}} + V_{\text{pc}}. \quad (7.2)$$

The fully uncorrelated covariance matrix comprises only diagonal elements, describing the statistic uncertainty and the systematic uncertainty from the TASR. V_{pc} is devoted to the remaining systematic effects.

The dotted lines in figure 7.8 depict the mean values of the effective endpoint, assuming correlation coefficients ρ in V_{pc} between zero and one. The deviation between $\rho = 0$ (blue line) and $\rho = 1$ (red line) amounts to $\Delta E_{0\text{eff}} = 0.23 \text{ eV}$. Since the response function uncertainties are expected to be highly correlated from run to run, the correlation coefficient is estimated to be $\rho = 0.9$. However, as can be seen in figure 7.8, the mean $E_{0\text{eff}}$ with large correlation coefficients lie above most of the single run fit values. Additionally, the corresponding χ^2 are increasing with increasing ρ . This is a known phenomenon in statistics and is a hint that the correlated uncertainties are overestimated [Cow98].

To investigate the parameter stability as a function of measurement time, the single run fit results are compared

with the uncorrelated averages. The results are summarized in table 7.5. The endpoint and the background variations over time are consistent with their associated uncertainties. The signal normalization has a good p-value for the short and medium range. However, the normalization is not stable over time with respect to its uncertainty for the long range. As discussed in section 7.4.1, this originates presumably from the systematic uncertainty on the DT concentration. Since this analysis employs shape-only covariance matrices, systematic uncertainties which affect only the overall normalization and consequently not the shape of the integral spectrum are not taken into account.

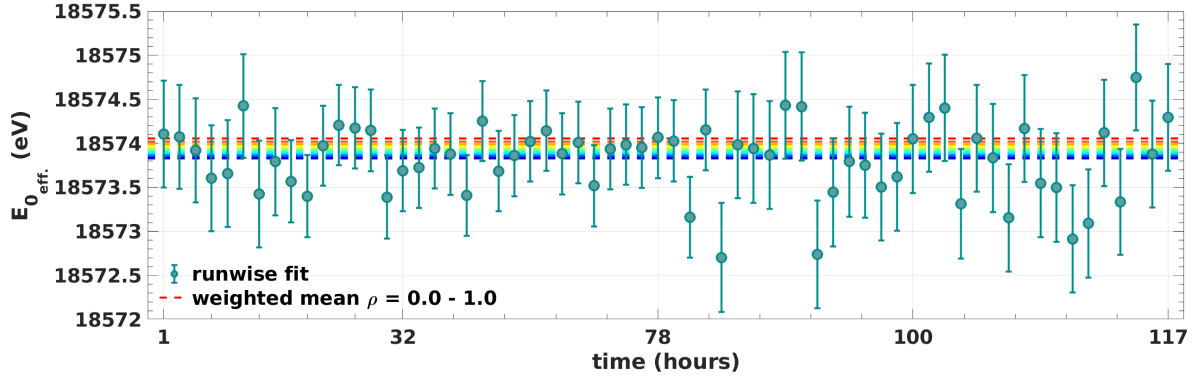


Figure 7.8: Stability of effective endpoint over time for the 400 eV range including statistic and systematic uncertainties. The correlated average is calculated assuming correlation coefficients between $\rho = 0$ (blue line) and $\rho = 1$ (red line).

	200 eV		400 eV		1600 eV	
	χ^2 (63 dof)	p-value	χ^2 (63 dof)	p-value	χ^2 (63 dof)	p-value
$E_{0\text{eff}}$	42.2	0.98	33.8	1.00	25.7	1.00
B	74.4	0.15	75.4	0.14	73.6	0.16
N	44.5	0.96	30.6	1.00	3837.7	0.00

Table 7.5: Goodness-of-fit with the χ^2 statistic. The uncorrelated means are taken as reference values.

7.5.2 Parameter Stability over Measurement Range including Systematic Uncertainties

With the same method as in section 7.4.2, the parameter stability as a function of the measurement range is investigated. In addition to statistic uncertainties, systematic effects are taken into account as well. The results of the three free fit parameters and the p-value are shown in figure 7.9. The stability over the measurement range is quantified in goodness-of-fit tests, summarized in table 7.6.

The p-values in figure 7.9 are, in contrast to section 7.4.2, for all energy ranges above the critical value of 5%. The larger the energy range, the better is the p-value. This appears to be rather unrealistic, because the integral spectrum is substantially more affected by systematic uncertainties for retarding potentials far away from the endpoint. The very large p-value of $p = 0.94$ for the long energy range indicates, that systematic uncertainties may be overestimated in this energy region.

Opposed to the analysis with statistic uncertainties, the effective endpoint and the signal normalization are stable within their total uncertainties as a function of fit range in addition to the background rate. This is reflected by the p-values in table 7.6. However, a remaining issue cannot be resolved by the inclusion of systematic effects: All fit range evolutions show patterns. The parameters are stable from 1600 eV until about 300 eV below the endpoint.

Thereafter they either increase or decrease monotonically. A runs test³ rejects the null hypothesis, that the fit parameters are randomly distributed around their average with a significance of more than 95 %.

This unresolved issue points either towards unaccounted systematic effects in the data or systematic uncertainties in the model. Since the modeling focused on the energy region relevant for the neutrino mass measurement (< 100 eV below E_0), it is expected to find discrepancies between model and data in the long and medium energy range. Therefore, the data points far away from the endpoint cannot be used to conclude whether the model is good enough for future neutrino mass campaigns. However, this former can only happen to limited extent due to the limited statistic close to the endpoint.

	χ^2 (11 dof)	p-value
$E_{0\text{eff}}$	0.75	1.00
B	0.21	1.00
N	11.5	0.40

Table 7.6: Goodness-of-fit test with the χ^2 statistic. Like in section 7.4.2 but systematic uncertainties included, a constant is fit to all parameter evolutions in figure 7.9 using the correlation matrix depicted in appendix C.2.

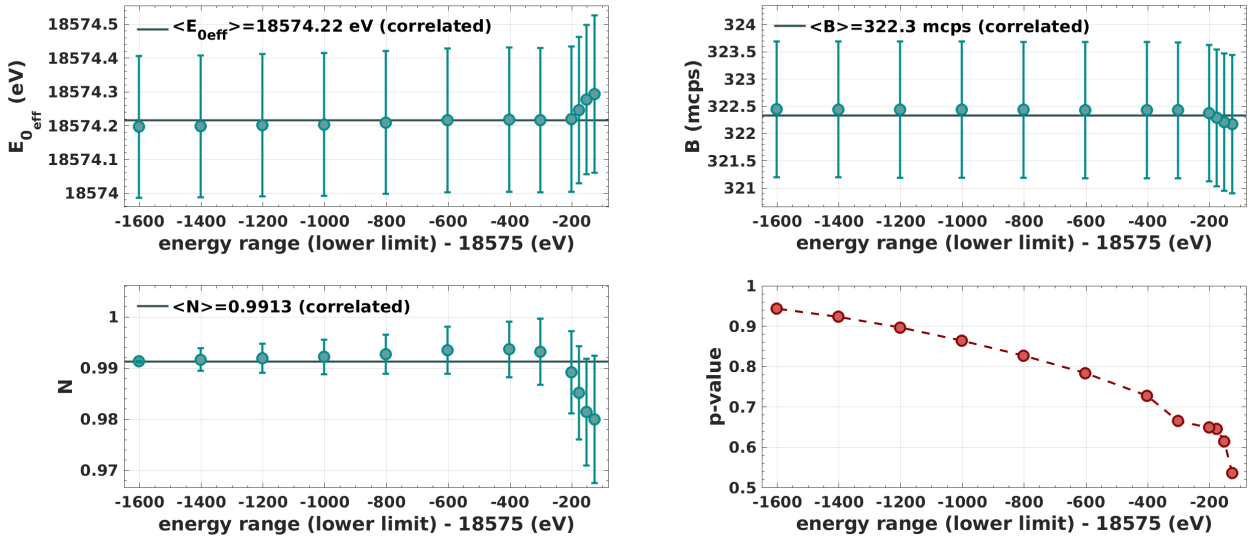


Figure 7.9: Fit results of the effective endpoint, background rate, signal normalization and the corresponding p-value as a function of energy range under the inclusion of systematic effects. The upper threshold of the analyzed energy window is fixed to 40 eV above the endpoint, whereas the lower threshold takes values between 1600 eV and 127 eV below the endpoint.

7.5.3 Comparison of Run Combination Methods

In sections 7.4.1 and 7.5.1, 64 runs are fit one after the other. In order to retrieve one joint result of each the fit parameter, the fit results are averaged according to eq. 5.16 and their uncertainties combined according to eq. 5.17. An alternative way of combining the runs and obtaining one common set of fit results is through stacking, as described in section 4.3. The 64 runs are selected, as such that all pass the quality criteria. The results for both methods are given in table 7.7.

³The runs test is a statistical test to check whether a sequence of data points is randomly distributed. For that, the data points are classified into two categories. Adjacent data points within the same category form a *run*. In order to be randomly distributed, the sequence must not have too many or too few runs [AH08].

Considering only statistic uncertainties, the error of the mean of all parameters is the same as the uncertainty estimated through the fit to the stacked spectrum. The central values, however, vary slightly between the run combination methods.

When additionally taking systematic uncertainties into account, the weighted average depends on the run to run correlation coefficient ρ , as described in the previous section. This dependency is illustrated in figure 7.10 for the effective endpoint. The central value of the mean effective endpoint as well as its associated uncertainty increases with increasing correlation coefficient. For all ρ , the average is smaller than the endpoint obtained from the stacked spectrum. However, for the expected correlation coefficient $\rho = 0.9$, the deviation is not significant within the uncertainties.

Further investigations whether this shift stays insignificant facing smaller statistic and systematic uncertainties will be performed with the data of the upcoming measurement campaign in March 2019.

		Average $\rho = 0$	Average $\rho = 0.9$	Stacked
stat only	$E_{0\text{eff}}$	$(18573.78 \pm 0.05) \text{ eV}$		$(18573.82 \pm 0.05) \text{ eV}$
	B	$(321.3 \pm 1.2) \text{ mcps}$		$(323.5 \pm 1.2) \text{ mcps}$
	N	$(0.9941 \pm 6 \cdot 10^{-4})$		$(0.9933 \pm 6 \cdot 10^{-4})$
stat + sys	$E_{0\text{eff}}$	$(18573.83 \pm 0.06) \text{ eV}$	$(18574.03 \pm 0.33) \text{ eV}$	$(18574.22 \pm 0.21) \text{ eV}$
	B	$(321.4 \pm 1.2) \text{ mcps}$	$(321.4 \pm 1.6) \text{ mcps}$	$(322.4 \pm 1.3) \text{ mcps}$
	N	(0.994 ± 0.001)	(0.991 ± 0.005)	(0.994 ± 0.005)

Table 7.7: Comparison of fit results using different run combination methods. The three fit parameters are obtained using the medium range and 64 runs. Statistic and systematic uncertainties are taken into account.

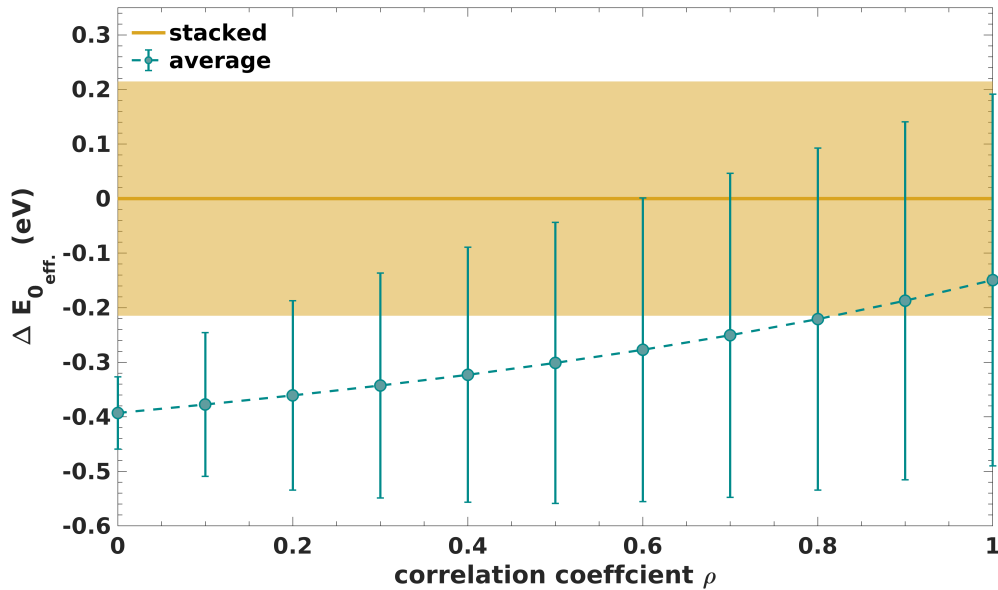


Figure 7.10: Comparison of run combination methods. The orange line depicts the effective endpoint and its uncertainty obtained from the fit to the stacked spectrum. The green points are the average effective endpoint as a function of the run to run correlation coefficient ρ with respect to the stacked fit result: $\Delta E_{0\text{eff}} = E_{0\text{eff}}^{\text{average}} - E_{0\text{eff}}^{\text{stacked}}$. While the medium energy range is chosen for display, the same trend is observed for the long and short energy range as well.

7.5.4 Impact of Different Energy Loss Function Parameterizations on Endpoint

The determination of the energy loss function, which is essential to accurately model the inelastic scattering of electrons on tritium molecules in the source, is one of the key tasks of the ongoing analysis of the electron gun commissioning measurements from October 2018. However, as discussed in section 3.2 and 6.5, currently two parameterizations of the energy loss function are available. To check the impact of the different parameterizations on the endpoint, the stacked spectrum of 64 runs using the medium range is fit twice: Once using the parametrization from Abdurashitov *et al.* and once employing Aseev *et al.*. The fit results are written in table 7.8.

Considering only statistic uncertainties, the effective endpoint using Abdurashitov *et al.* is 130 meV larger compared to Aseev *et al.*. This deviance corresponds to almost 3σ . Additionally, the Abdurashitov *et al.* parametrization yields a better χ^2 than Aseev *et al.*. However, since only statistic uncertainties are taken into account, both p-values are much lower than the critical value of 0.05.

When including systematic effects, the effective endpoint using Abdurashitov *et al.* is about 30 meV smaller than Aseev *et al.*. Note, that this is the opposite behavior compared the fit with only statistic uncertainties. However, due to the increased uncertainty on $E_{0\text{eff}}$, this deviation is no longer significant. As before, the χ^2 is better when using Abdurashitov *et al.* compared to Aseev *et al.*.

This gives confidence to use the Abdurashitov *et al.* parametrization as the default for the first tritium data analysis rather than the older parametrization. As demonstrated, the Abdurashitov *et al.* energy loss function improves the χ^2 of the fit on the one hand and on the other hand, as discussed in section 6.5, provides this parametrization is a more consistent uncertainty treatment.

		Abdurashitov <i>et al.</i>	Aseev <i>et al.</i>
stat only	$E_{0\text{eff}}$	18573.82 ± 0.05 eV	18573.69 ± 0.05 eV
	χ^2 (17 dof)	34.4	45.1
stat + sys	$E_{0\text{eff}}$	18574.22 ± 0.21 eV	18574.25 ± 0.21 eV
	χ^2 (17 dof)	13.1	15.2

Table 7.8: Impact of different energy loss function parameterizations on endpoint.

7.5.5 Impact of Systematic Effects on Effective Endpoint

The value of the effective endpoint as well as its uncertainty increase when including systematic uncertainties. Being the key parameter of interest of the first tritium campaign, this behavior is investigated in more detail by switching on systematic effects one after the other.

The central value for the effective endpoint is shown in figure 7.11. For each point a different covariance matrix is used. While the leftmost point takes only statistic uncertainties into account, all other fits are performed considering a single systematic effect in addition to statistic uncertainties. The rightmost point uses the combined covariance matrix, including all uncertainties from table 7.2. While the theoretical corrections and the energy loss function have little impact on $E_{0\text{eff}}$, all other systematic effects pull the effective endpoint towards higher values. Being the dominant systematic effect, the product of column density and inelastic scattering cross section has the largest impact. The overall shift, considering all systematic effects, amounts to 0.39 eV, which is almost twice as large as the associated uncertainty on $E_{0\text{eff}}$.

The uncertainties on the effective endpoint are depicted in figure 7.4 as the upper bar. Comparing the two bars, it becomes evident that the uncertainties, obtained through fits to data, are very similar to the expected sensitivities, described in section 7.3. As a rule of thumb, the systematic effects which have a large contribution to the uncertainty on the effective endpoint, give rise to large $E_{0\text{eff}}$ shift as well.

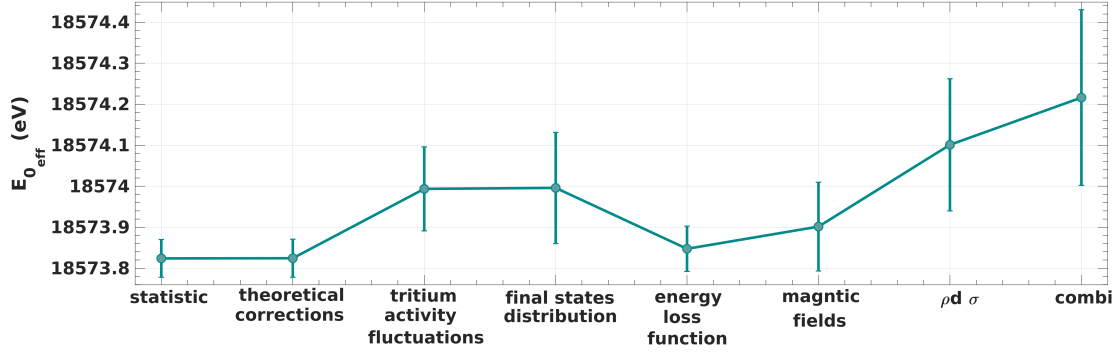


Figure 7.11: Fit results for the effective endpoint. All fits employ the medium range of 64 stacked runs.

7.5.6 Impact of Final State Distribution on Fit

To check the influence of the final state distribution on the fit, the stacked spectrum is fit using the medium range multiple times, assuming models with different **FSD**. Since the gas composition inside the **WGTS** contains almost exclusively DT, only the **FSD** for DT is varied. Systematic uncertainties are taken into account according to table 7.2. The fit results are summarized in table 7.9.

As presented before, the fit to the stacked spectrum using the default **FSD** results in a good p-value of 0.73 and an effective endpoint of 18574.22 eV. When excluding the excited states (ES), the model is no longer able to describe the data well. In addition, all three fit parameters shift significantly. The same is observed when modeling the integral spectrum without any **FSD**. Consequently, the hypotheses that there are no excited states or no final state distribution at all are rejected.

Surprisingly, when using the **FSD** for a different isotopologue than DT, namely for HT or T_2 , to describe the tritium β -decay of DT, the p-values are better compared to the default **FSD**. Note that the **FSD** for HT and T_2 come from a different calculation than the **FSD** for DT. Furthermore, the fit yields an effective endpoint, which is 0.25 eV (HT) to 0.20 eV (T_2) larger with respect to DT. As can be seen in appendix C.4, this shift too large to originate solely from the slightly different recoil energies of the three isotopologues. Additionally, this endpoint shift cannot be reproduced in the same way in a simulation: An Asimov data set with largely enhanced statistics is calculated with the **FSD** for DT. This integral spectrum is fit using a model, which assumes the **FSD** for T_2 . In case only statistic uncertainties are considered, the estimated endpoint is shifted by up to 0.55 eV with respect to the value in the Asimov data. For very short energy ranges of less than 60 eV below the endpoint, this shift is diminished to less than 0.01 eV. This implies that the observed endpoint shift in the simulation originates dominantly from differences in the description of the excited states. However, when including the **FSD** covariance matrix in the Asimov fit, the endpoint shift is as little as -0.02 eV for large energy ranges and even less for shorter ranges. Consequently, the endpoint shift observed in the data analysis, is still to be understood.

In addition to using different precalculated **FSD**, the normalization factor of the ground state probability N_{GS} and the normalization factor of the excited states N_{ES} are introduced as free fit parameters. They are accompanied by a pull term in the χ^2 formula, as described in section 6.2. In order not to account twice for the **FSD** normalization uncertainty, the **FSD** covariance matrix contains only the uncertainty on the **FSD** variance. Improving the p-value, the fit obtains slightly larger values for both normalization factors compared to the default values in the precalculated **FSD**:

$$\text{Default: } N_{\text{GS}} = (57.31 \pm 1.00)\% \quad , \quad N_{\text{ES}} = (40.06 \pm 1.00)\% \quad (7.3)$$

$$\text{Fit: } N_{\text{GS}} = (56.58 \pm 0.89)\% \quad , \quad N_{\text{ES}} = (40.80 \pm 0.90)\% \quad (7.4)$$

Furthermore, the endpoint is shifted by 70 meV.

This study demonstrates that the **FSD** has a crucial impact on the endpoint and therefore also on the neutrino mass in future measurement campaigns. The development of a more adequate description of the **FSD** is ongoing.

model FSD	p-value	χ^2 (17 dof)	$E_{0\text{eff}}$	B	N
DT FSD	0.73	13.1	18574.22 eV	322 mcps	0.99
DT FSD + FSD Fit	0.75	12.7	18574.29 eV	322 mcps	0.99
DT FSD (w/o ES)	0.00	360.0	18571.44 eV	328 mcps	1.50
NO FSD	0.00	400.4	18569.89 eV	328 mcps	0.92
HT FSD	0.90	10.0	18574.47 eV	322 mcps	0.99
T ₂ FSD	0.90	10.1	18574.42 eV	322 mcps	0.99

Table 7.9: Fit to medium range of 64 stacked runs including systematic effects. The integral spectrum is modeled using different final state distributions.

7.5.7 Determination of Column Density from Integral Spectrum

The systematic uncertainty of 2.2% on the column density is much larger than the targeted precision of 0.1%, as discussed in section 7.2. Due to the lacking electron gun, $\rho d \cdot \sigma_{\text{inel}}$ cannot be measured directly but has to be inferred by comparing observables like the vessel pressure to thermodynamical gas models. However, as depicted in figure 7.1, the column density is stable within $1.5 \cdot 10^{-5}$ over the course of several days. Although very accurate, the column density determination is not yet very precise.

Beside thermodynamical gas simulations, the integral spectrum itself provides a handle on the column density. Since ρd is not implemented yet as a free fit parameter in *Samak*, the integral spectrum is fit multiple times assuming different column densities. This procedure is further on referred to as *column density scan*. Since the other fit parameters are free to vary and adjust at a different values, a column density scan is equivalent to a manually performed fit of the column density. By fitting a polynomial to the third power to the resulting χ^2 curve, the column density is determined as shown in figure 7.12 (top).

However, one has to keep in mind that the column density is strongly correlated with the signal normalization. Before fitting, the differential spectrum is normalized with an initial normalization factor N_i , which is proportional to the column density next to a set of other parameters, for example the tritium decay constant. When fitting, the free fit parameter N is able to modify the initial normalization. The effective normalization factor of the differential spectrum is consequently

$$N_{\text{eff}} = N_i \cdot N. \quad (7.5)$$

Therefore, the fit parameter N is anticorrelated to the ρd in the column density scan: A too large ρd in the model can be compensated to great extent by a reduced N in the fit. This is shown in the example of one column density scan in figure 7.12 (bottom right). Additionally, correlations with the effective endpoint and the background rate are observed.

Figure 7.13 depicts the expected sensitivity on the column density for different energy ranges, obtained through fits on an Asimov data set according to section 5.2.2. The systematic uncertainty budget corresponds to table 7.2. Since ρd shall be determined, the uncertainty on ρd is not taken into account. The best sensitivity of about 5% is obtained by including all data points far away from the endpoint. For energy ranges with a lower limit more than $qU - 18575 = -200$ eV, the sensitivity worsens drastically. Compared to the systematic uncertainty of 2.2% given by the *WGTS* hardware group, the expected column density sensitivity is rather large.

Thereafter, the same procedure is applied to the integral spectrum of 64 runs for varying energy ranges, as can be seen in figure 7.14. The retrieved uncertainties on ρd are similar to the estimated sensitivities. In this case the central values deviate between the analysis using only statistic uncertainties and the analysis including systematic uncertainties. For all energy ranges including data points further than 300 eV away from the endpoint, the column density including systematic effects is larger than the column density considering only statistic uncertainties. The column density scan, which takes the full energy range into account, yields a column density which is 0.2% lower (stat) and 5.1% larger (stat + sys) compared to the expected value of $\rho d = 4.56 \cdot 10^{17}$ mol/cm². Similar to section 7.5.2, the results of the column density scans show a fit range dependence. Following the argumentation of section 7.5.2, more data at retarding potentials close to the endpoint is needed for further investigation.

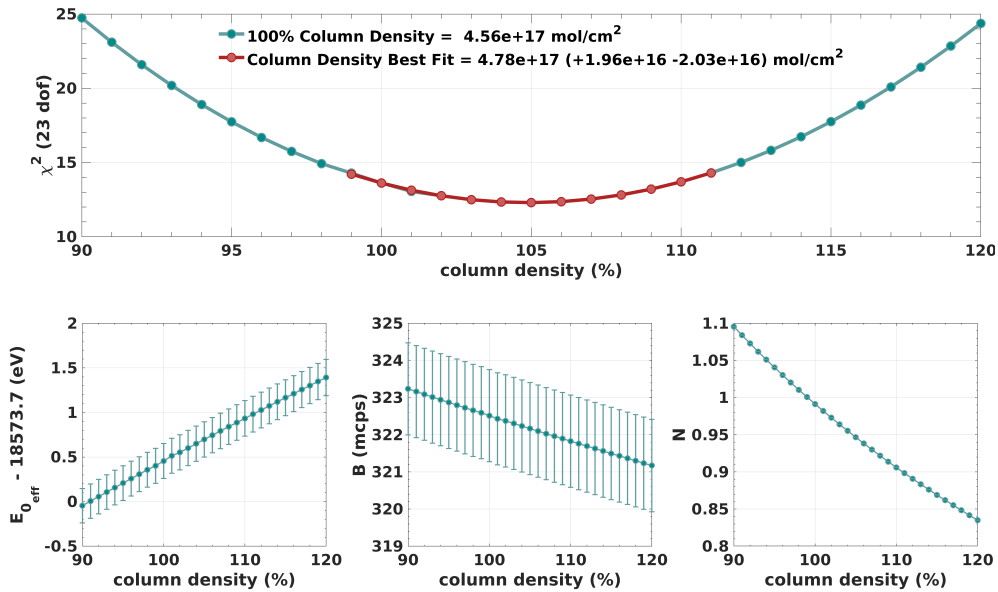


Figure 7.12: Determination of ρd by fitting the integral spectrum several times assuming different column densities. **Top:** Minimum χ^2 as a function of column density. The minimum is obtained by fitting a polynomial to the third power to the curve. **Bottom:** Fit parameters as a function of column density.

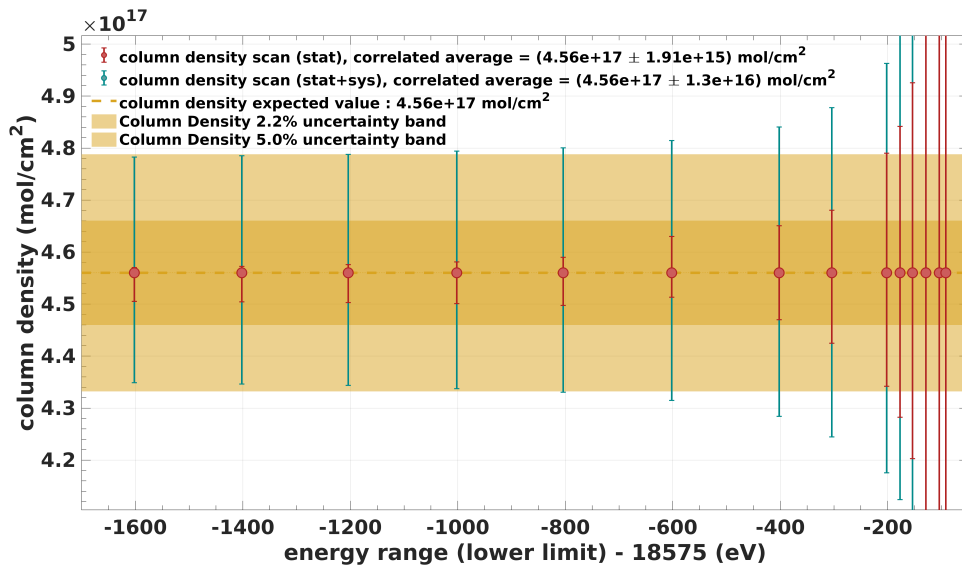


Figure 7.13: Estimation of column density sensitivity for different energy ranges on MC data mimicking first tritium runs.

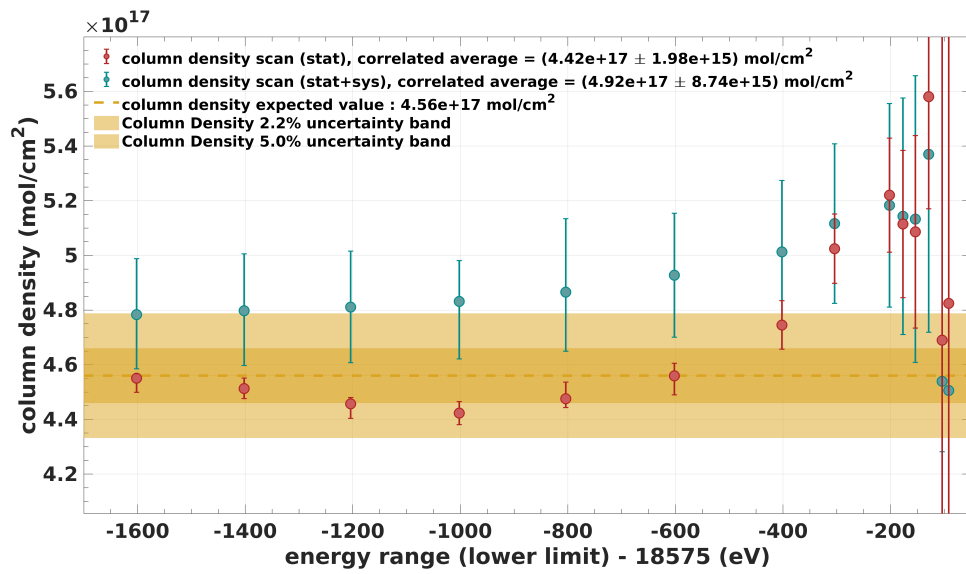


Figure 7.14: Column densities, obtained through column density scans, for different energy ranges on first tritium data.

Chapter 8

KATRIN Neutrino Mass Sensitivity

Sensitivity studies are a powerful tool during the design of an experiment. Simulations show which set of [KATRIN](#) parameters is needed to yield the desired neutrino mass sensitivity of 200 meV at 90% confidence. Additionally, sensitivity studies tell us to which precision these parameters ought to be determined. This was done to great extent in the Design Report [[A⁺b](#)] before the construction of [KATRIN](#). Along the way of construction and commissioning, it became clear that some important parameters changed with respect to the Design Report. An overview of the nominal settings is given in table [3.2](#). The most prominent example is the background, which was anticipated to be 10 mcps. First measurements with the main spectrometer revealed a significantly higher background in the order of a few hundred mcps. In order to improve the sensitivity under the changed scenario, the adjustable [KATRIN](#) parameters, for example the magnetic field settings or the measurement time distribution ([MTD](#)), are adapted to the new situation with the help of simulations. In this analysis, the [KATRIN](#) neutrino mass sensitivity is calculated for different background scenarios, including systematic effects using the covariance matrices described in section [6](#). Furthermore, different measurement strategies with regard to [MTDs](#) and measurement energy ranges are investigated. A matching covariance matrix is calculated for every background level, [MTD](#), energy range and systematic budget correspondingly.

This chapter is structured as follows. Firstly, the elevated background level and attempts of its reduction are discussed. Secondly, the utilized measurement time distributions are presented, following a discussion on the systematic uncertainty budget. Results of the sensitivity calculations are shown in section [8.4-8.6](#), starting with the reproduction of the Design Report sensitivity as the benchmark scenario. Afterwards, the sensitivities for the most recent background level are shown. In the final section of this chapter, an intermediate background level, which was observed during [SDS](#) measurements, is investigated and compared to previous studies.

8.1 Elevated Background

A large fraction of background electrons, reaching the detector within the same energy window as the electrons from the tritium β -decay, have their origin in the walls of the main spectrometer vessel. The walls suffer from a large unanticipated ^{210}Pb contamination. Highly excited atoms, called Rydberg atoms, are formed through α -decay in the decay chain of ^{210}Pb . Driven by the recoil energy from the decay, these excited atoms are able to reach the inner part of the spectrometer vessel. Since they do not carry any electronic charge, the inner electrode system is not able to prevent their entering into the spectrometer vessel. Further on, the Rydberg atoms are ionized by room-temperature thermal radiation. If the electron is emitted near the analyzing plane, it will be accelerated towards the focal plane detector by the retarding potential to a similar kinetic energy as the tritium β -electrons. Consequently, background electrons, originating from Rydberg atoms, have the same signature in the [FSD](#) as β -electrons [[Har15](#)].

Dedicated background measurements in the course of the [SDS](#) campaigns have shown, that a large component of the background rate is proportional to the volume V of the main spectrometer's flux tube. The volume, on the other hand, is approximately inverse proportional to the magnetic field in the analyzing plane B_a , which is

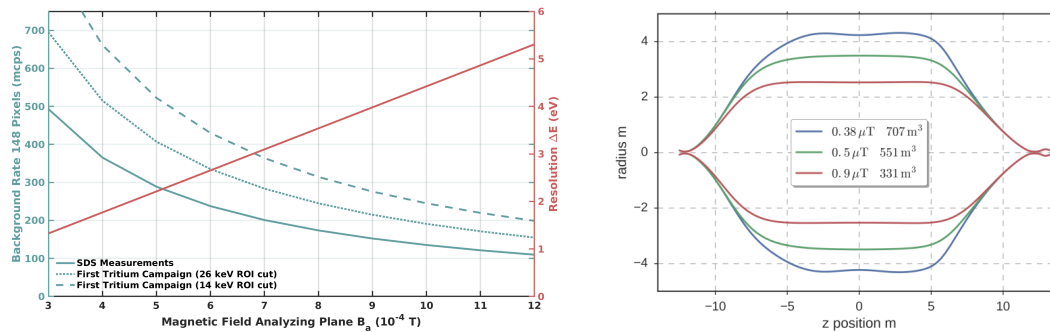


Figure 8.1: **Left:** Relationship between magnetic field in the analyzing plane B_a , background rate and energy resolution. The solid blue curve shows the background parametrization, performed by [Tro18], scaled to 70% magnetic field strength of the source and pinch magnet. The remaining two blue curves depict the background parametrization of [Tro18] scaled to the background level, observed during the first tritium campaign. The dotted line shows the background rate for a ROI energy cut of [26 keV, 32 keV] and the dashed for the wider [14 keV, 32 keV] ROI cut. The red line illustrates the dependency of the energy resolution on B_a for 70% magnetic field strength of the source and pinch magnet and a retarding energy of 18575 eV. **Right:** Main spectrometer flux tube dimension and volume for three different magnetic fields in the analyzing plane B_a . Taken from [Tro18]

illustrated in figure 8.1 (right).

$$\text{Background} \propto V \propto \frac{1}{B_a} + \text{const.} \quad (8.1)$$

Thus, the volume and therefore the background rate, can be reduced by increasing B_a . Further details about the background measurement and the background parametrization can be found in [Tro18]. Aside from the background reduction, higher magnetic field strengths in the analyzing plane lead to an increased energy resolution ΔE of the main spectrometer.

$$\frac{\Delta E}{E} = \frac{B_a}{B_{\text{max}}} \quad (8.2)$$

The interplay between background rate and energy resolution under varying B_a is depicted in figure 8.1 (left). Consequently, B_a has to be adapted to the new scenario with respect to the design value of 3 μ T in a way that the background rate is reduced while the energy resolution is kept at an acceptable level. This is conducted in section 8.6.1.

However, the background rate observed in the commissioning measurements of the first tritium campaign in June 2018 is higher than in the previous SDS measurements. At $B_a = 6$ G the background rate for 148 pixels increases from 235 mcps to 430 mcps [Pol]. This elevated background rate is shown in figure 8.1 (left) for two different region of interest (ROI) energy cuts. The upper ROI threshold is fixed to 32 keV, whereas the lower threshold varies between the two values of 14 keV and 26 keV. The narrower analysis window of [26 keV, 32 keV] yields a lower background rate than the wider window of [14 keV, 32 keV], since more background is excluded from the data. The drawback of a narrow ROI cut is that signal is cut away as well, which translates into a reduced FPD coverage¹. which is a reduced effective efficiency of the FPD as illustrated in figure 8.2. The background parametrization from [Tro18] is scaled to the level of the first tritium campaign for the following analysis.

8.2 Measurement Time Distribution

The neutrino mass sensitivity depends strongly on the measurement time distribution (MTD). Obviously, in order to determine the neutrino mass, KATRIN has to measure the β -spectrum in an energy region, in which it is most

¹The FPD coverage is a parameter, which describes the signal loss due to the ROI cut. In this analysis, the FPD coverage is implemented effectively as a reduced FPD efficiency: reduced efficiency = coverage \cdot efficiency.

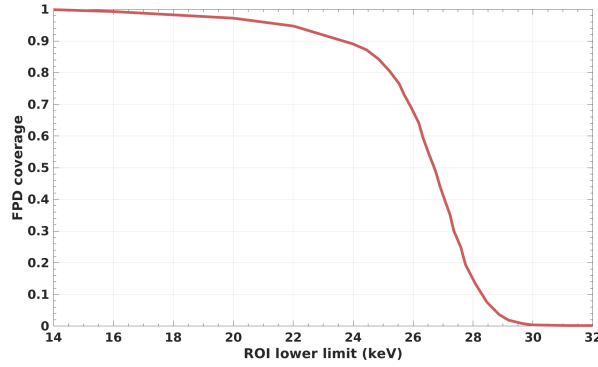


Figure 8.2: Coverage of the focal plane detector (FPD) as a function of lower limit of the ROI energy cut. The upper limit of the ROI is fixed at 32 keV. The narrower the analysis window, the more signal is excluded from the data. Thus the FPD coverage is decreasing with increasing lower ROI threshold [Eno18].

sensitive to the imprint of the neutrino mass. The neutrino mass signal in the spectrum depends on the neutrino mass itself, but also on the KATRIN settings. Therefore, every new scenario, for example an increased background rate or a different magnetic field configuration, requires its own customized MTD. The adjustment of the MTD follows closely the change of the neutrino mass signal. Figure 8.3 depicts the neutrino mass signal in the integral spectrum for different background and magnetic field configurations. The higher the background, the smaller is the neutrino mass signal in the spectrum. In addition to that, shifts the neutrino mass towards energies farther away from the endpoint with increasing magnetic field strength in the analyzing plane B_a . Consequently, it is desirable to construct MTDs, which are optimized with respect to the given set of KATRIN parameters. On the other hand, it is required that the MTDs are robust to slight variations of the former. Exemplary, undetected shifts of the work function or a rise of the background rate should not alter the sensitivity significantly.

The MTD, proposed in the Design Report, was optimized for the nominal KATRIN settings and a background level of 10 mcps. This MTD, reaching 30 eV below the anticipated endpoint, is used for the benchmark calculation of the Design Report sensitivities and can be found in the appendix A.1. However, this MTD cannot be used for realistic sensitivity studies regarding the elevated background rate. As can be seen in figure 8.3, the neutrino mass signal is shifted farther away from the endpoint with increasing background. Therefore the time spent very close to the endpoint has to be redistributed to lower retarding potentials, where the neutrino mass signal, given the elevated background level, is most visible. The MTDs used in such a calculation, have to be adapted and optimized to every new scenario accordingly. In the following, two kinds of MTDs, obtained with different optimization techniques, are considered.

Firstly, *KaFit* MTDs, which were optimized in previous work by M. Kleesiek [Kle14] for the background level, observed during SDS measurements. The idea is to link the neutrino mass sensitivity with a MTD, which has fixed high voltage set points but a variable distribution of measurement time per high voltage bin. The MTD is optimized with respect to its sensitivity using Markov Chain Monte Carlo method. Note, that these MTDs were originally optimized for 100% magnetic field strength, i.e. a magnetic field of $B_s = 3.6$ T at the source and of $B_{\max} = 6$ T at the pinch magnet, whereas in this study 70% magnetic field strengths are used to account for current hardware limitations. The *KaFit* MTDs are adapted to the reduced magnetic field strength manually [Beh]. An example of such a MTD is depicted in figure A.1.

Secondly, *IsoStat*⁺ MTD, which are optimized with the Samak framework in this work. The *IsoStat*⁺ MTDs consist of three components. The basis is a measurement time distribution, which is proportional to the inverse rate of the integrated tritium spectrum. This ensures approximately the same amount of measured electrons for each high voltage setting. The second component is proportional to the expected neutrino mass signal, that means the ratio of integrated spectra with and without a neutrino mass ($m_\nu = 0.5$ eV). Consequently, more time is spent in the energy window, in which KATRIN is most sensitive to the neutrino mass. Additionally, a number of bins are added above the endpoint, to determine the background. The weights, with which these three components enter the MTD, are variable. The *IsoStat*⁺ MTD is further optimized by calculating the sensitivity, including systematic

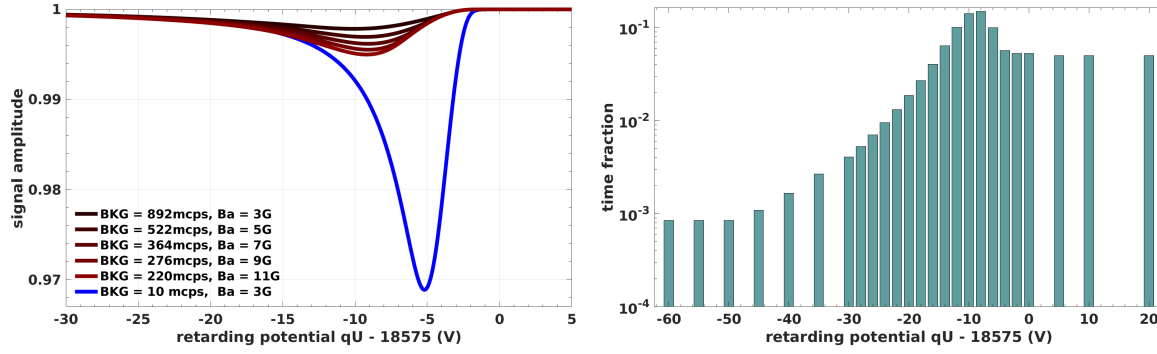


Figure 8.3: **Left:** The neutrino mass signal is the ratio between an integral spectrum with a neutrino mass of 0.5 eV to an integral spectrum without a neutrino mass. The blue line depicts the neutrino mass signal for nominal *KATRIN* settings from the Design Report. The nominal settings are given in table 3.2. The other curves show the signal amplitudes for different magnetic field strengths in the analyzing plane B_a . The background rate is scaled to the background level of the first tritium campaign, using a ROI lower energy threshold of 14 keV. The higher the background rate, the smaller is the signal amplitude. Furthermore, the maximum of the neutrino mass signal shifts farther away from the endpoint with increasing B_a . **Right:** *IsoStat⁺* MTD, optimized for an energy range of $[E_0 - 60 \text{ eV}, E_0 + 20 \text{ eV}]$, a magnetic field strength in the analyzing plane of $B_a = 7$ G and 70% magnetic field strength of the pinch and source magnets. All other settings are nominal. The MTD consists of three components with different weights: the inverse rate of the integrated tritium spectrum, the neutrino mass signal inside the spectrum and bins above the endpoint for the background determination. The MTD is optimized by minimizing the sensitivity for variable weights.

effects, by varying the weights. Exemplary an *IsoStat⁺* MTD is shown in figure 8.3 and A.1. For 60 eV, the widest energy range considered, the *IsoStat⁺* MTDs spent less than 1% of the measurement time at retarding energies more than 30 eV below the endpoint, whereas the *KaFit* MTDs spent significantly more time, approximately 5.5%, in this energy region.

8.3 Systematic Uncertainty Budget

The uncertainties on systematic effects, used for the sensitivity calculations, are motivated as follows. For the full measurement time, the uncertainty budget is oriented on the Design Report goals. However, to achieve this kind of precision, further commissioning measurements are still to be done. Exemplary, the uncertainty on the product of column density and inelastic scattering cross section $\rho d\sigma_{\text{inel}}$ during the first commissioning measurement with tritium was estimated to be approximately 5%. The large deviation from the final goal of 0.1% can be traced back to the lack of an electron gun during this measurement, which allows the precise determination as well as the monitoring of $\rho d\sigma_{\text{inel}}$. However, such an electron gun was installed shortly after the tritium commissioning. Consequently, it is expected, that the knowledge of the *KATRIN* apparatus will improve continuously over the total measurement time. Table 8.1 summarizes the systematic uncertainties used for the sensitivity calculation of different measurement intervals.

The uncertainty of $\rho d\sigma_{\text{inel}}$ is conservatively estimated to be 2.1% for the first neutrino mass data taking period with a duration of about one month. For a net measurement time of about one year, it is decreasing to 0.7%, whereas it reaches the lower limit of its design values of 0.1% for the full measurement time of three years. For accumulated measurement times of less than three years, the estimation of the energy loss function uncertainty is performed according to 5.4. Since *KATRIN* has scheduled dedicated, high precision energy loss function measurements in the future, the uncertainty on the energy loss function is assumed to be negligible in this analysis for the full measurement time. The magnetic field strengths of the two solenoid magnets decrease in a similar way to $\rho d\sigma_{\text{inel}}$ over the course of time from 1% to 0.2%. Furthermore, the uncertainty on B_a was characterized by [Erh16] and the final state distribution (FSD) uncertainty is estimated according to section 6.2.

	1 month	1 year	3 years
$\rho d \cdot \sigma_{\text{inel}}$	2.1 %	0.7 %	0.1 %
energy loss function	Aseev <i>et al.</i> and Abdurashitov <i>et al.</i>		negligible
B_s, B_{max}	1.0 %	0.5 %	0.2 %
B_a	$B_a \cdot 3.9 \cdot 10^{-3} + 1.07 \cdot 10^{-6} \text{T}$		
final state distribution (FSD)	1 % normalization, 1 % (2 %) variance ground (+ excited) states		
theoretical corrections	ON / OFF		

Table 8.1: Relative systematic uncertainties on main KATRIN input parameters for three different time stages. The uncertainty budget is decreasing with time, since the knowledge about the system will accumulate during the measurement phases.

8.4 KATRIN Design Report (TDR) Sensitivity

Firstly, the KATRIN Design Report sensitivities [A⁺b] are recalculated with Samak. This serves as a cross check and validation of Samak on the one hand, as well as a first comparison between the different approaches of including systematic effects in sensitivity calculations on the other hand. The Design Report estimates systematic sensitivity contributions by calculating the maximal neutrino mass shift Δm_ν^2 induced by a given systematic effect. This is achieved with a fit to an Asimov data set, which is modeled with the "true" input parameters, using a model, in which one input parameter, e.g. the column density ρd , is systematically shifted by its uncertainty e.g. $\Delta \rho d$. The individual systematic contributions are further on added in quadrature.

$$\sigma_{\text{tot}} = \sqrt{\sigma_{\text{stat}}^2 + \sigma_{\text{sys1}}^2 + \sigma_{\text{sys2}}^2 + \dots} \quad (8.3)$$

In contrast, Samak utilizes the methods described in section 5.2 and 5.4, treating an arbitrary number of systematic effects at once. The covariance matrix V , accounting for systematic uncertainties of the final state distribution, the response function and for statistical uncertainties, for example, amounts to

$$V = V_{\text{FSD}} + V_{\text{RF}} + V_{\text{Stat}}. \quad (8.4)$$

The sensitivity from the Design Report as well as the sensitivities calculated with Samak are depicted in figure 8.4 (left). The upper bar illustrates the TDR sensitivity, whereas the lower bars stands for the Samak sensitivity. The main model input parameters can be found in [A⁺b] (page 218, table 7). The neutrino mass is set to zero and the endpoint energy to 18575 eV. The measurement time distribution, reaching 30 eV below the anticipated endpoint, can be found in the appendix A.1. The white boxes with dashed borders show the statistical sensitivity for a measurement time of three years. The statistical sensitivity in the Design Report is about 7 meV larger than the Samak sensitivity. Since only the main input settings are stated in [A⁺b], it cannot be excluded that some of the input parameters of minor influence on the spectrum, may be slightly different compared to the corresponding Design Report values. Having this in mind, the statistical sensitivities agree well with each other.

The contributions of the systematic sensitivities, estimated with Samak, are illustrated with the colored boxes. The systematic budget corresponds mainly to [A⁺b], except the estimation of the FSD and the energy loss function (chapter 6). The broad stacked bar shows the sensitivity evolution, switching on systematic effects one after the other. For example, the broad red box stands for the sensitivity using statistical uncertainties and uncertainties from the theoretical correction, whereas the broad yellow box, gives the sensitivity taking into account statistical uncertainties, uncertainties from the theoretical correction and the final state distribution, and so on. Since uncertainties, arising from different origins, have to be added quadratically, the lengths of each broad box doesn't scale linearly with its individual contribution. Because of that, the single contributions, using only the uncertainty from statistics and the corresponding systematic effects, are depicted as the thin bars under the broad bar.

In the Design Report the total sensitivity sums up to 202 meV, using a systematics budget of 167 meV. Within this budget, 128 meV originate from identified systematics. The total sensitivity, calculated with Samak comes to 181 meV, with a contribution of 134 meV from systematic uncertainties. Accordingly, the systematic budget estimation with Samak agree with the identified systematics budget from the Design Report. The table of identified

$1\sigma(m_\nu^2)$	TDR	Samak
stat	0.018 eV ²	0.017 eV ²
sys	0.017 eV ²	0.011 eV ²
sys (identified)	0.010 eV ²	
total	0.025 eV ²	0.020 eV ²

Table 8.2: Nominal sensitivities on the neutrino mass squared at 68.3% confidence level. The sensitivities in the middle column are taken from the [KATRIN Design Report \[A⁺b\]](#). In the [TDR](#), systematic uncertainties are estimated by calculating the maximal neutrino mass shift for each systematic effect. The individual contributions are furthermore added in quadrature. In contrast to that, the sensitivities in the rightmost column are obtained with [Samak](#). Here the systematic effects are included at once with covariance matrices.

systematic effects can be found in the [TDR](#). [Samak](#) treats uncertainties from the [FSD](#), all magnetic fields, energy loss function, column density, inelastic cross section and theoretical corrections such as radiative corrections. Thus, not all the uncertainties from [TDR](#) are included in the covariance matrices of this analysis yet. Uncertainties, which are not regarded in this analysis are for example elastic scattering and electric potential distortions in the [WGTS](#). Nevertheless, the small difference between total sensitivities of only 21 meV indicated, that the dominant systematic contributions are estimated correctly in [Samak](#). Furthermore the fundamental difference in the applied methods, may also give rise to different sensitivity values. The [TDR](#) states sensitivities in terms of the neutrino mass squared and 68.3% confidence level. Due to that, the former sensitivities are given in this format in [table 8.2](#) for reference.

The systematic uncertainty from the response function comprises uncertainties on all magnetic fields, the product of column density and inelastic scattering cross section and the energy loss function. Since it's the dominant systematic effect in this analysis, the sensitivity contribution from the response function uncertainty is broken down into it's components, as displayed in [figure 8.4](#) (right). The stack plot reads as follows: Firstly, the thick light blue bar illustrates the sensitivity using statistical and $\rho d\sigma_{\text{inel}}$ uncertainties. Secondly, the thick green bar represents the sensitivity, regarding the former two and the magnetic fields. Thirdly, the thick yellow bar gives the sensitivity when taking all response function components in addition to statistical uncertainties into account. Furthermore, the lower thin bars depict the individual contributions from the response function elements in combination with statistical sensitivity. This breakdown reveals that the dominant contribution comes from the energy loss function uncertainty. Considering only the energy loss function and statistical uncertainties, the neutrino mass sensitivity is 177.7 meV, out of a total response function and statistical contribution of 178.4 meV. [Equations 8.5](#) and [8.3](#) translate this to a systematic sensitivity contribution from the energy loss function alone. The neutrino mass sensitivities have to be squared before entering [eq. 8.3](#), because [KATRIN](#) is only sensitive to m_ν^2 . The systematic sensitivity contribution from the energy loss function is approximately 126 meV. This number is higher than the design goal of less than 57 to 99 meV. Because of that, more precise measurements of the energy loss function will be performed with an electron gun in the upcoming measurement phases.

$$L_{\text{Eloss}}(90\% \text{C.L.}) = \sqrt[4]{(L_{\text{Eloss} + \text{Stat}})^4 - (L_{\text{Stat}})^4} = \sqrt[4]{(177.7 \text{ meV})^4 - (165.1 \text{ meV})^4} = 126.3 \text{ meV} \quad (8.5)$$

8.5 Sensitivity with Current Background Level of 364 mcps

The neutrino mass sensitivity is calculated for the elevated background level, observed during the first tritium campaign 2018, using a [ROI](#) energy window of [14 keV, 32 keV]. For a magnetic field in the analyzing plane of 7 G, this corresponds to a background rate of 364 mcps for the whole [FPD](#) wafer (148 pixels). The [FPD](#) efficiency is taken to be 95% with a coverage of 99.9%, resulting in an effective efficiency of $\epsilon_{\text{FPD}} = 94.05\%$. The two outer rings from the [FPD](#), are excluded from the analysis. Due to hardware limitations, the magnetic field strengths of the two solenoid magnets are at 70% of their nominal value, namely 2.52 T for the source magnet and 4.20 T for the pinch magnet. The magnetic field strength in the analyzing plane is optimized with respect to the trade off between background and energy resolution in [section 8.6](#). For the background scenario observed during the

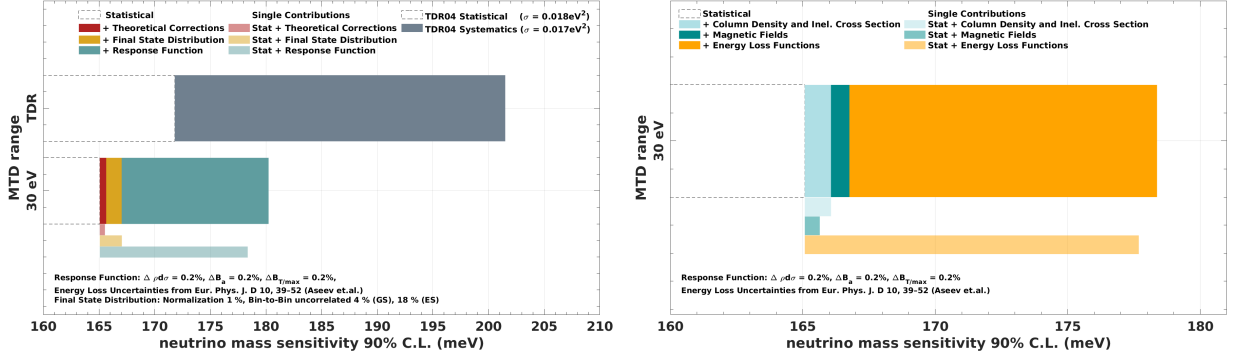


Figure 8.4: Nominal *KATRIN* sensitivity on the neutrino mass at 90% confidence level (C.L.). **Left:** Sensitivity break down of the systematic effects: theoretical corrections, such as radiative corrections, the final state distribution and the response function. The upper bar shows the statistical and total sensitivity according to the Design Report [A⁺b], whereas the colorful bars represent the sensitivities obtained with *Samak*. The statistical uncertainties agree within 7 meV with each other. The contribution of systematic effects estimated with *Samak* agrees with the identified systematics budget from the Design Report. **Right:** Break down of sensitivity contributions from the response function. The response function depends on various parameters: the product of column density ρd and inelastic scattering cross section σ_{inel} , three magnetic fields (B_a, B_{max}, B_s) and the energy loss function parameterization. The uncertainty on the energy loss function gives rise to the dominant contribution.

SDS measurement, the optimal B_a comes to 7 G. Since the optimum is not expected to differ significantly for the background level in this analysis, B_a is set to 7 G. In order to explore possible measuring strategies further, two energy ranges, namely 30 and 60 eV below the anticipated endpoint, are considered using the *IsoStat*⁺ MTD. All *KATRIN* parameters, which differ from their nominal values in [A⁺b], are listed in table 8.3. The systematic uncertainty budget for the different measurement times is taken from table 8.1, if not stated otherwise.

parameter	value
B_s	2.52 T
B_{max}	4.2 T
B_a	7 G
background (148 Pixel)	364 mcps
ϵ_{FPD}	94.05 %
FPD pixels	124
MTD	<i>IsoStat</i> ⁺
energy range	30 eV and 60 eV below E_0

Table 8.3: *KATRIN* parameters, used in this analysis. All other input parameters are nominal.

8.5.1 Statistical Sensitivity

Before studying the total sensitivity, which comprises both statistical and systematical effects, the influence of the elevated background rate on the statistical sensitivity alone is investigated. Figure 8.5 shows the statistical neutrino mass sensitivity as a function of measurement time for four different background levels in the 30 eV measurement interval.

The statistical sensitivity using the background rate, magnetic field settings and MTD from the TDR is depicted as the red line. This sensitivity doesn't differ significantly from the design value, even though the two outer FPD rings are excluded and the total measurement time is reduced to 30 instead of 36 months. However, the statistical sensitivity is greatly affected by the increased the background rate. The remaining three lines represent

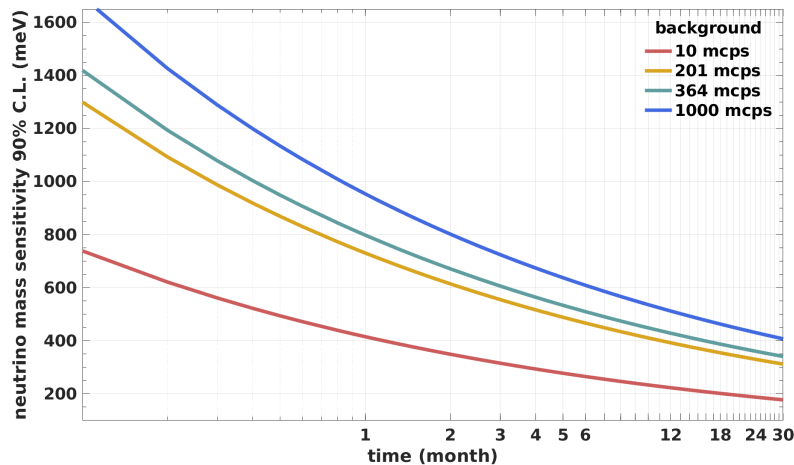


Figure 8.5: Statistical neutrino mass sensitivity at 90% confidence level as a function of measurement time for the 30 eV scan range. After just a few hours the neutrino mass sensitivity comes to approximately 1.4 eV for the current background level. Thereafter the former decreases steeply in the course of the first few months. After four months, the sensitivity curve becomes flatter, such that after 30 months the sensitivity yields approx. 340 meV. The statistical sensitivity curves runs similarly for the other background rates. The higher the background rate, the worse is the statistical sensitivity.

the sensitivities using the input parameters from table 8.3 and three elevated background levels. The yellow line shows the sensitivity with the SDS background rate, the green line with the current background rate and the blue line with a hypothetical background level of 1 cps. All four curves behave similarly. Within the first few months, the sensitivity decreases steeply. After about four months, the curves flatten out. The higher the background rate, the larger is the final statistical sensitivity after 30 months. The relation between background rate and statistical sensitivity is displayed in figure D.2.

The statistical sensitivity, assuming the current background level, comes to about 800 meV after one month and to 340 meV after the full measurement time of 30 months.

8.5.2 Sensitivity Breakdown for One Month

An upper limit below 1 eV on the neutrino mass is a milestone in the history of laboratory based neutrino mass measurements. The previous section shows that this is achievable from the statistical point of view in a matter of about one week. Nevertheless, since the knowledge and calibration of the KATRIN apparatus is not at its final level, the systematic uncertainty budget estimated for the first neutrino mass data taking period may exceed the design values. Due to that, systematic effects play an important role in the first measurement phase and have to be taken into account for realistic estimations. The following sensitivity calculations demonstrate, that KATRIN will reach a sub-eV-sensitivity in as few as one month of measurement time. The corresponding sensitivity breakdown for 30 days is illustrated in figure 8.6.

The statistical sensitivity after one month, illustrated as the white dashed bars, is 689 meV for the 60 eV scan range and 803 meV for the 30 eV range. Due to the steep rise of the β -spectrum below the endpoint $dN/dE \propto (E_0 - E)^2$, the statistical sensitivity is significantly better in the wider scan range, even though only a fraction of less than 1% of measurement time is spent below 30 eV in the IsoStat⁺ MTD. The total sensitivity mounts up to 767 meV for the 60 eV range and, in contrast to the statistical sensitivity only slightly higher, 810 meV for the 30 eV range.

The sensitivity breakdown is shown in figure 8.6 by the colored bars. The broad bars resemble the total sensitivity, including systematic effects one after the other. Exemplary, the broad yellow bar show the sensitivity taking the uncertainty from statistics, theoretical corrections and the FSD into account. The narrow colored bar, show the sensitivity contribution of only one systematic effect at once in addition to statistical sensitivity. For both

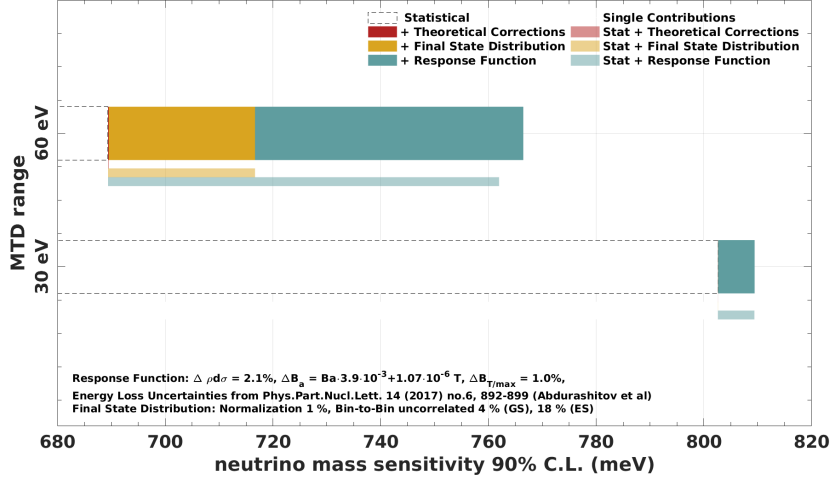


Figure 8.6: Neutrino mass sensitivity breakdown at 90% confidence level for 30 days of measurement time. The background of 364 mcps corresponds to the level, observed during the first tritium campaign, scaled to $B_a = 7$ G. The *IsoStat*⁺ MTDs are used for two energy ranges of 30 eV and 60 eV below the anticipated endpoint of 18575 eV.

measurement energy windows, the contribution from theoretical corrections play a minor role. Furthermore, the FSD has almost no influence for the 30 eV range sensitivity, whereas it becomes important for the wider scan window. This originates from the separation of the FSD into ground and excited states. The description of the latter has a significantly larger uncertainty than the ground state. Since the excited states start at excitation energies of about 18 eV, the 60 eV range is much more affected. The dominant systematic uncertainty for both energy ranges is the uncertainty on the response function. Similar to the FSD uncertainty, the response function uncertainty has a larger impact for the wide energy range. Having a 114 meV smaller statistical sensitivity than the 30 eV range, the 60 eV range, ends up with a total sensitivity, which is only 43 meV better than 30 eV range. This shows that the 60 eV range suffers substantially more from systematic effects, despite the small time fraction spent deeper than 30 eV into the spectrum.

To conclude, this section demonstrates that *KATRIN* yields a sub-eV neutrino mass sensitivity in less than one month of measurement time for both scan ranges. While the statistical uncertainty is smaller for the 60 eV range, the former is substantially more affected by systematic effects. Due to that, the total sensitivity is similar for both ranges. Given that, it could be considered to measure further than 30 eV below the endpoint for a short time, such that the increase of systematic uncertainties is balanced by the gain in statistics. This opens the door for investigations of systematic effects with data, in particular the final state distribution (FSD).

8.5.3 Response Function Breakdown and Impact of Energy Loss Function Parameterizations

Since the response function uncertainty is the dominant systematic effect for one month of measurement time, it is worthwhile to go one step deeper and to investigate the influence of its building elements. As described in 6.5, the response function and therefore its uncertainty comprises the product of column density ρd and inelastic scattering cross section σ_{inel} , the magnetic fields B_{max}, B_s, B_a and the energy loss function. Figure 8.7 shows the breakdown for the response function's sensitivity contributions. The two graphs differ with respect to the energy loss function parametrization and error estimation. While the left employs the energy loss function from Abdurashitov *et al.* [A⁺a], the right uses the one from Aseev *et al.* [A⁺c]. For a detailed comparison refer to section 6.5. Since the two parameterizations are very similar, the sensitivities regarding statistical, $\rho d \sigma_{\text{inel}}$ and the magnetic field uncertainties using either Abdurashitov *et al.* or Aseev *et al.* are almost identical. However, the estimation of the energy loss function uncertainties differ substantially from parametrization to parametrization. The impact of the energy loss function uncertainty on the sensitivity is much stronger using the Abdurashitov *et al.* compared to Aseev *et al.*. With the newer parametrization the energy loss function uncertainty outweighs the

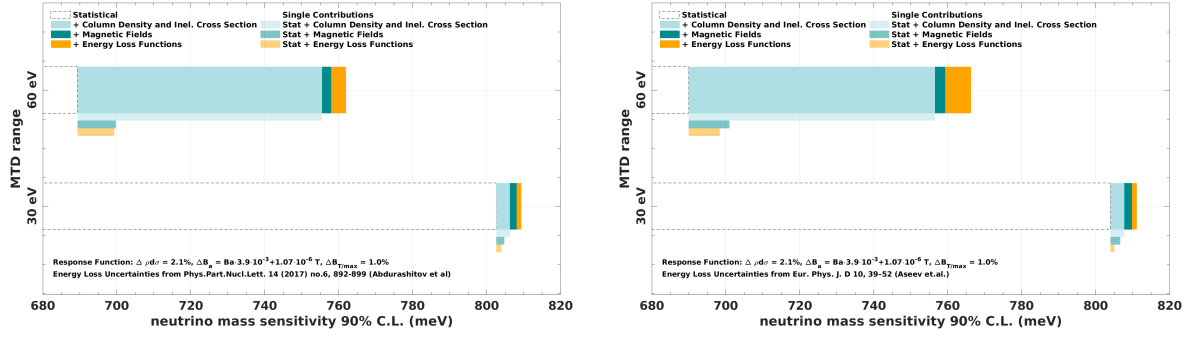


Figure 8.7: Sensitivity breakdown of the response function for 30 days of measurement time at 90% confidence level. The two figures differ in the parametrization of the energy loss function and its uncertainty estimation. The left graph employs the parametrization from Abdurashitov *et al.*, whereas the right graph uses [A⁺c]Aseev *et al.*

magnetic fields uncertainties by far and gives rise to the second largest contribution for the 60 eV range and to the largest contribution for the 30 eV range. In contrast to that is the sensitivity based on the Aseev *et al.* energy loss function even smaller than the sensitivity taking the magnetic fields uncertainties into account. However, for both parameterizations gives the uncertainty on the product of column density and inelastic cross section the largest contribution to the total sensitivity for the wider energy range.

8.5.4 Sensitivity Breakdown for the Full Measurement Time

Going beyond the expected sensitivity for the first neutrino mass data taking period, the sensitivity breakdown for the full measurement time of 900 days is shown in figure 8.8. As for 30 measurement days, the 60 eV range yields a better statistical sensitivity than the 30 eV range on the one hand, but is more affected by systematic effects on the other hand. The dominant systematic effect for the 60 eV range is the FSD, which plays only a minor role in the smaller energy window. The response function uncertainty impacts the sensitivity greatly for both ranges. Since the uncertainty from the energy loss function is expected to be reduced to a negligible level by dedicated measurements, it is not depicted in the response function breakdown. In contrast to the previous section, the sensitivity contribution from the magnetic fields outweigh those from $\rho d\sigma_{\text{inel}}$.

The wider range yields a total sensitivity of 331 meV, which comprises contributions from statistics of 294 meV and from systematic effects of 260 meV. The 30 eV sensitivity amounts up to 347 meV, where 341 meV come from statistical uncertainties and 174 meV from systematic uncertainties. Thereafter, the neutrino mass sensitivity is still statistics dominated after 900 days (30 month) of measurement time. Considering the MTDs and the systematic uncertainty budget of this study, the equilibrium between statistic and systematic uncertainties occurs after about 450 month for the 30 eV range and after approximately 50 month for the 60 eV. Consequently, KATRIN has the potential of improving its sensitivity by extending its operation time.

8.6 Sensitivity with SDS Background Level of 201 mcps

In previous works by [Kle14] and [Beh], the neutrino mass sensitivity was calculated for the elevated background level, observed during the SDS measurements. At $B_a = 7$ G and 70% magnetic field strength of the source and pinch magnet, this corresponds to a background rate for the FPD wafer (148 pixels) of 201 mcps. In order to optimize the magnetic field settings with respect to the elevated background level, neutrino mass sensitivities were calculated for different B_a . Systematic effects were included in the same manner as in the Design Report, namely by calculating the neutrino mass shift, induced by a given systematic effect. This treatment of systematics differs substantially from the treatment in the analysis at hand. Thus, the neutrino mass sensitivities, corresponding to the SDS background level, are recalculated using the new systematics treatment for KATRIN with covariance matrices, in order to investigate this difference. Moreover, this study gives the opportunity to investigate the

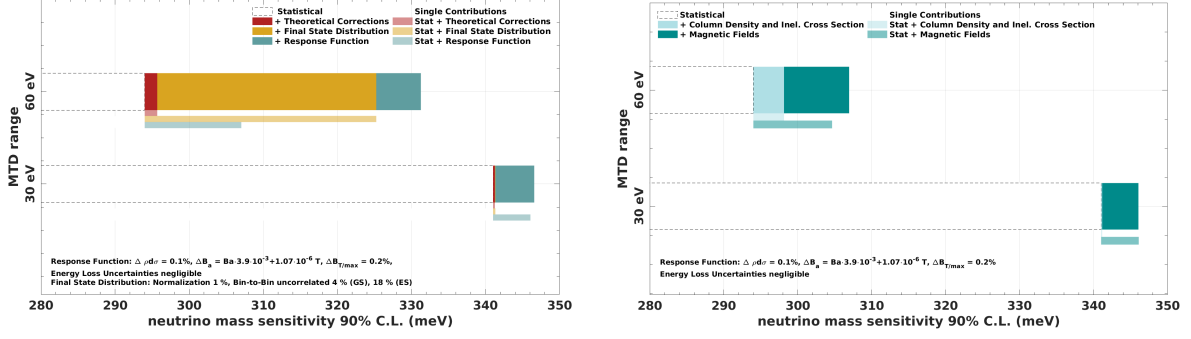


Figure 8.8: Neutrino mass sensitivity at 90% confidence level for a measurement time of 900 days and two scan ranges. **Left:** Sensitivity breakdown for uncertainties from statistics, theoretical corrections, final state distribution and response function. **Right:** Sensitivity breakdown for the contributions from the response function.

influence of different measurement time distributions (MTDs) on the sensitivity, since the two kinds of optimized MTDs, namely *KaFit* and *IsoStat*⁺, are available for this scenario. *KATRIN* parameters, which differ from their nominal values in [A⁺b], are listed in table 8.4.

parameter	value
B_s	2.52 T
B_{\max}	4.2 T
B_a	3-12 G
background (148 Pixel)	201 mcps at $B_a = 7$ G
ϵ_{FPD}	90%
FPD pixels	148
MTD	<i>KaFit</i> and <i>IsoStat</i> ⁺
energy range	30 eV, 45 eV and 60 eV below E_0

Table 8.4: *KATRIN* parameters, used in this analysis, which differ from the nominal setting in [A⁺b].

8.6.1 Optimizing B_a - Background vs. Energy Resolution

Due to the trade off between background and energy resolution, the optimal magnetic field strength in the analyzing plane differs from the nominal value of 3 G. Taking that into account, the neutrino mass sensitivity is calculated using ten different B_a between 3 G and 12 G, using the *KaFit* MTDs. Furthermore, three energy ranges, namely 30, 45 and 60 eV below the anticipated endpoint are considered. The MTDs are optimized according to each setting. For each MTD a matching set of covariance matrices, accounting for uncertainties with regard to the response function, final state distribution and theoretical corrections, is computed. The uncertainty budget is given in 8.1. Uncertainties on the energy loss function parametrization from Aseev *et al.* are taken into account.

Figure 8.9 (left) shows the statistical sensitivity as a function of B_a and corresponding background rate. For all B_a the best statistical sensitivity is obtained with the 60 eV range. This is, as already discussed in 8.5.2, due to the shape of the β -spectrum.

For all energy ranges the statistical neutrino mass sensitivity decreases about 40 meV from 3 G to 9 G. Rising B_a within this interval translates to an increase of the energy resolution from 1.3 eV to 4.0 eV, whereas the background decreases from almost 500 mcps to about 150 mcps. Since the sensitivity is improving up to $B_a = 9$ G, the background suppression wins over the increase of resolution. However, increasing B_a and consequently also the resolution further doesn't lead to a significant improvement in the statistical sensitivity. All curves are very flat.

Figure 8.9 (right) shows the sensitivity development including systematic effects. In this scenario, the 30 eV energy

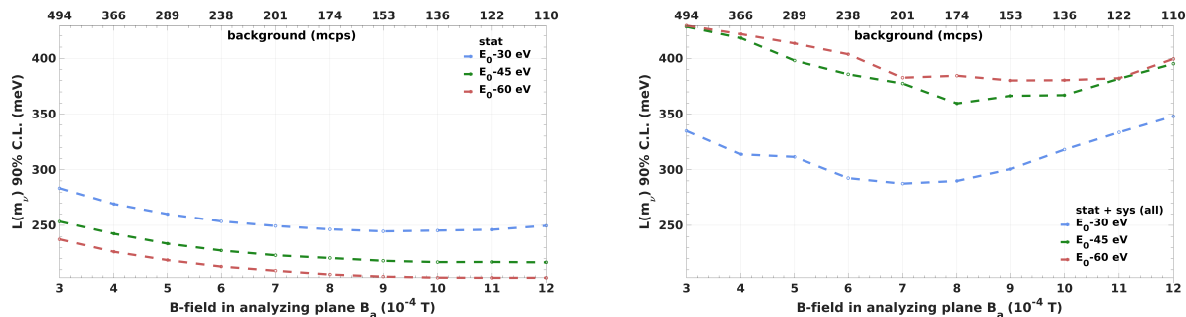


Figure 8.9: Neutrino mass sensitivities $L(m_\nu)$ of three scan ranges for varying magnetic fields in the analyzing planes and corresponding background rates (upper x-axis). The 60 eV range yields the best statistical sensitivity for all B_a , whereas the sensitivity, including systematic effects, is obtained with the 30 eV range MTD for all B_a . **Left:** Statistic uncertainties only **Right:** Statistic and systematic uncertainties. The systematic uncertainties take uncertainties from the response function ($\rho d\sigma$, σ_{inel} , B_{max} , B_s , B_a , energy loss function), FSD and theoretical corrections into account.

range yields the best sensitivities for all B_a . Similar to the statistical case, the sensitivity decreases with increasing magnetic field until a certain B_a . In contrast to the previous case, the sensitivity increases again after finding a minimum at 7 G for the 30 eV range and about 8 G for the higher ranges. For 45 and 60 eV the minimum is not as pronounced as in the 30 eV range. At these magnetic field strengths the suppression of the background rate doesn't outweigh the increasing energy resolution anymore. In addition to that increases the absolute uncertainty on B_a as well, as shown in appendix D.1. An increase in ΔB_a is propagated through the model of the inelastic scatterings and through the spectrometer transmission. Therefore affects this the sensitivity strongly.

An overview plot, showing the sensitivity development for each systematic effect, can be found in appendix D.3. The change of the optimal measurement when including systematic effects, can be also observed when considering only the FSD uncertainty or only the response function uncertainty. Based on that, a magnetic field strength in the analysis plane of 7 G, which corresponds to an energy resolution of 3.1 eV, is used for all further analysis, if not explicitly denoted otherwise.

In previous studies the optimal B_a was found to be 6 G. In contrast to the analysis at hand, [Beh] and [Kle14] concluded that the 60 eV measurement range is preferable over the 30 eV range, even when including systematic effects.

8.6.2 Sensitivity Breakdown

The previous section concludes that for a given B_a , the inclusion of systematic effects in the sensitivity calculations results in a reversed order of preferred scan ranges with respect to the purely statistical treatment. This stands in contradiction to previous studies [Beh, Kle14]. To bring further light into this, each systematic effect is switched on, one after the other. The result is shown in figure 8.10. The colored bars, depict the results using covariance matrices to include systematic uncertainties. The gray bars show the systematics budget, used in [Kle14].

For MTDs, going 30 eV into the spectrum, the dominant systematic uncertainty is the response function, whereas the FSD and theoretical corrections play a subordinate role. This picture changes for the higher energy ranges. Even though the response function on its own still causes the largest systematic uncertainty, the final state distribution follows shortly after. Comparing the thin bars to the broad bar for 45 and 60 eV shows, that sensitivity cannot be recovered significantly with decreasing only the uncertainty of the response function of the final state distribution. Let's consider 60 eV energy range exemplary. Starting at a statistical sensitivity of 215 meV, the total sensitivity sums up to about 390 meV. If, in the extreme case, there was no uncertainty on the response function, the sensitivity would decrease to 340 meV. The other way round, if the FSD uncertainty was diminished to zero, the sensitivity is decreases to 355 meV. Consequently, only a reduction of both main systematic uncertainties, the

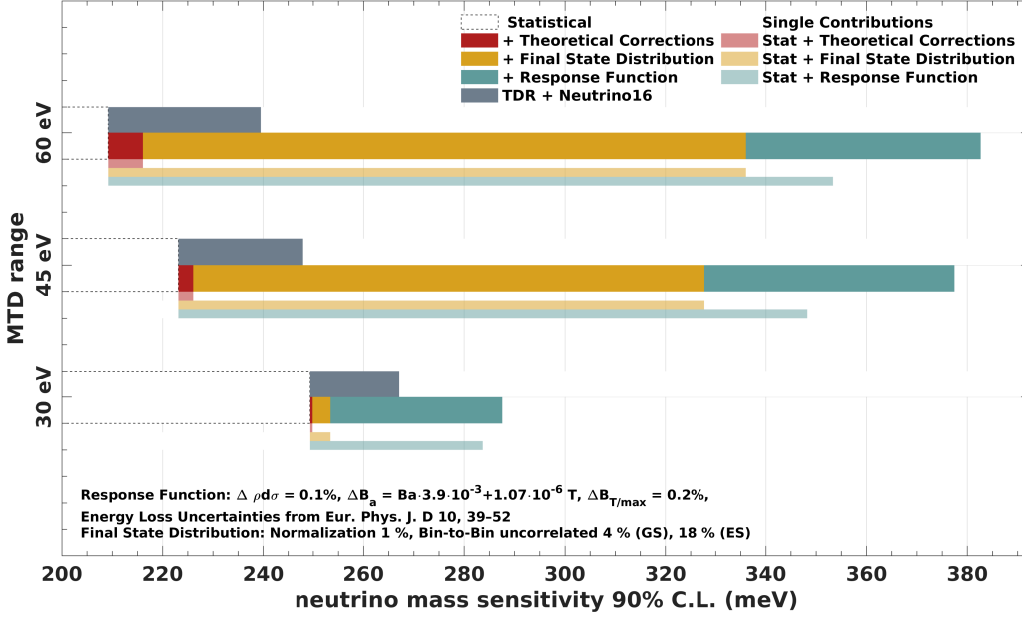


Figure 8.10: Neutrino mass sensitivity (90% C.L.) breakdown of systematic effects for three years of measurement time using *KaFit* MTDs. Uncertainties, arising from systematic effects strongly increase when going deeper into the spectrum. For energy ranges of 45 and 60 eV, the main systematic uncertainties originate from the response function and the final state distribution. A large improvement in sensitivity can be achieved for the higher ranges only by reducing both main systematic uncertainties at the same time. The gray bars show the contribution of systematic uncertainties calculated by [Beh, Kle14].

response function and the final state distribution, will result in a significantly improved sensitivity for the wider energy ranges.

The gray bars show, that the contribution from systematic effects in [Beh, Kle14] is much smaller than with the covariance matrix approach. The wider the MTD range, the larger is the deviation. In the analysis at hand, the systematic effects are energy dependent, because every covariance matrix is calculated individually for each magnetic field setting and measurement range. [Beh, Kle14] take the energy dependent increase of systematic uncertainties only through an increased systematic uncertainty on inelastic scatterings into account. Due to that, the neutrino mass sensitivity is driven by the statistical uncertainty, which is smaller for the wider than for the narrower range.

8.6.3 Impact of MTDs on the Sensitivity

In order to investigate the impact of the MTDs on the sensitivity, the neutrino mass sensitivities in the same scenario as in the previous section, are calculated using the *IsoStat*⁺ MTDs instead of the *KaFit* MTDs. As can be seen when comparing figure 8.11 to 8.10, the statistical sensitivities for 30 eV as well as for 60 eV are larger with the *IsoStat*⁺ MTDs. This demonstrates the large dependence of the neutrino mass sensitivity on the MTD. Since the *IsoStat*⁺ MTDs are not as highly optimized to the specified scenario, but have a more conceptual origin, the statistical sensitivities are 50-60 meV larger. The systematic uncertainties, however, behave differently. The 60 eV range yields, in contrast to the *KaFit* MTD, a better sensitivity than the 30 eV range. Due to the fewer time spent below 30 eV, the increase of systematic uncertainties is outweighed by the gain in statistics. The *KaFit* MTDs spend approximately 5.5% of measurement time in the energy region, in which systematics largely increase, whereas the *IsoStat*⁺ MTDs spent less than 1%. In that way, the *IsoStat*⁺ MTDs yields a better sensitivity in the 60 eV range, namely about 310 meV, than the *KaFit* MTDs, which is 390 meV. This shows, that the inclusion of energy dependent systematic effects is crucial in the MTD optimization process. A combination of highly optimized *KaFit* MTD and

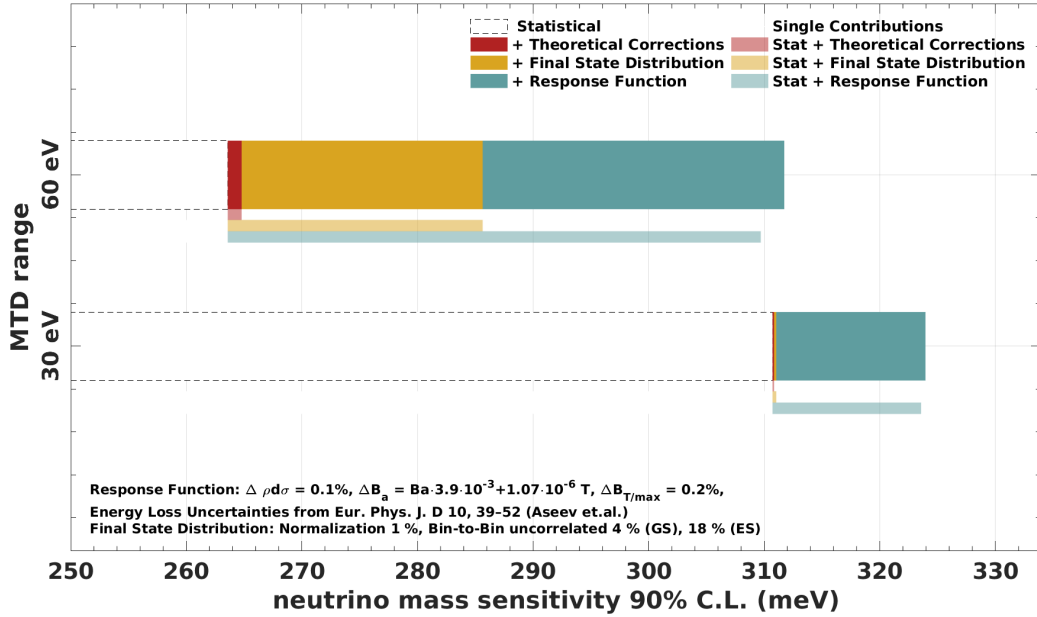


Figure 8.11: Neutrino mass sensitivity (90% C.L.) breakdown of systematic effects for three years of measurement time using *IsoStat*⁺ MTDs. Since the 60 eV MTD spends only a very little time fraction below 30 eV, the increase of systematic uncertainties is balanced by the gain of statistics. In that way a better total neutrino mass sensitivity is obtained with the *IsoStat*⁺ MTD than with the *KaFit* MTD for the 60 eV range, even though the statistical sensitivity from the *IsoStat*⁺ MTD is approx. 50 meV larger.

robust *IsoStat*⁺ MTD, spending only a small time fraction at low retarding potentials, should be considered for future measurements.

Chapter 9

Summary and Conclusion

In the frame of this thesis a new method to include systematic effects in the [KATRIN](#) experiment was explored. Systematic uncertainties are propagated through a model of the molecular tritium β -decay and the transmission of the experimental setup with extensive Monte Carlo simulations, taking possible correlations between systematic effects into account. The impact on the integral spectrum is further on estimated with covariance matrices, keeping track of bin-to-bin correlations within the spectrum. This method was implemented successfully in the frame of this work in form of a new class in the simulation and analysis software [Samak](#). Being now fully automatized, it is possible to calculate, combine and store covariance matrices for any desired set of systematic effects and associated uncertainties. Furthermore, various features for display and sanity checks are available in the code. The method of covariance matrices enables a consistent energy dependent consideration of systematic effects in both simulations and data analysis.

A series of systematic effects were considered. They range from modifications of the conventional description of the β -decay by the Fermi theory over systematic effects associated with the inelastic scattering of the β -electron on tritium molecules to systematic uncertainties on the spectrometer resolution.

The developed treatment of systematic effects in [KATRIN](#) was applied in two ways in this thesis: Firstly, in the analysis of the first [KATRIN](#) tritium data, taken in October 2018. Secondly, in a comprehensive neutrino mass sensitivity study in the light of the elevated background level.

Analysis of First KATRIN Tritium Data

Cumulating to a measurement time of approximately 4.9 days, 64 scans of the tritium β -spectrum were analyzed. The goal of the tritium commissioning measurement was to demonstrate a global system stability to the per mil level and to investigate the impact of systematic effects on the integral spectrum. The main physical parameter of interest in this data analysis was the endpoint of the tritium spectrum. Being strongly correlated to the neutrino mass, which was set to zero throughout this work due to its low sensitivity, the endpoint is influenced by systematic effects in a similar way. Therefore, the analysis of the endpoint acts as a valuable proxy with respect to future neutrino mass measurement campaigns.

The magnitude of influence of the systematic uncertainties on the endpoint was broken down into the individual effects. The total uncertainty on the endpoint cumulates to 210 meV. For both, the short and medium energy range (200 eV and 400 eV below E_0), the uncertainty on the product of column density and inelastic scattering cross section is the dominant systematic effect, exceeding even the statistic uncertainty. Consequently, the first tritium commissioning campaign is systematics dominated with respect to the endpoint, when combining the statistics of 64 runs. The uncertainty on the molecular final state distribution amounts to the second largest and for the long range (1600 eV below E_0) even to the largest contribution. Furthermore, a shift of the central value of the endpoint was observed when including systematic effects in the data analysis. The maximal endpoint shift for the medium range is 390 meV taking all systematic effects into account.

Furthermore, the parameter evolution over the course of measurement time for three different measurement

ranges was investigated. It was found, that the variation of the endpoint is consistent with statistical fluctuations. However, the deviation from a constant endpoint becomes larger with respect to the uncertainties from short to medium energy range. This changes when including systematic uncertainties. In this case, the endpoint fluctuations are in very good agreement with their uncertainties for all energy ranges.

Moreover, the signal normalization as a function of measurement time was found to be stable for the short and medium range. In contrast to that, for the long range the fluctuation of the signal normalization with respect to a constant is significant even when taking systematic uncertainties into account. Being particularly sensitive to the tritium activity, slightly *wrong* assumptions on the column density or on the molecular DT concentration with respect to the actual measurement lead to a normalization factor that differs significantly from one. When this tritium activity bias is different from run to run, the signal normalization factor is not stable over time. Due to the high statistics of the long range, the variation of the normalization factor becomes significant. This is in general of no concern, since an uncertainty on the overall activity does not degrade the neutrino mass and endpoint sensitivities. However, a systematic uncertainty on ρd does not only alter the normalization but also the shape of the spectrum. Therefore, the column density needs eventually to be known to the per mil level. Also we expect improvements on the molecular DT concentration measurement: [LARA](#), which monitors the gas composition inside the [WGTS](#), was not designed to measure DT concentrations as low as those of the first tritium campaign. Thus, the non-stable signal normalization originates presumably from a systematic uncertainty on the latter. Since the upcoming first neutrino mass measurement campaign, scheduled in March 2019, will utilize a much higher tritium purity, this issue is expected to be resolved.

Moreover, the parameter evolution as a function of measurement range was studied. In contrast to the analysis considering only statistic uncertainties, the endpoint and the signal normalization were found to be stable within uncertainties when including systematic effects. However, a remaining pattern can be observed for all parameters evolutions: Endpoint, signal normalization and background are approximately constant for large energy ranges until about 300 eV. Thereafter, they increase (E_0) or decrease (N , B) monotonically. This observation implies unaccounted systematic effects. The modeling focused on the energy region close to the endpoint (< 100 eV below E_0), which will be relevant to future neutrino mass measurements. The patterns of the fit parameters may originate from effects further away from the endpoint or from the current model of the final state distribution and energy loss function, whose development is ongoing. The lack of statistics in the energy region close to the endpoint limits the ability to conclude whether the model is good enough for upcoming m_ν measurements.

Additionally, the impact of the energy loss function on the endpoint and on the goodness-of-fit was studied. The energy loss function plays a key role in the accurate description of the inelastic scattering processes in the [WGTS](#), and a more precise determination of the former is one of the main tasks in the ongoing data analysis of the STS-III campaign in October 2018. At the time of writing, two energy loss functions, measured with the Troitsk ν -mass experiment, were available: Aseev *et al.* from the year 2000 and Abdurashitov *et al.* from 2017. Considering only statistic uncertainties, the endpoint obtained with Abdurashitov *et al.* is significantly larger and the χ^2 better compared to Aseev *et al.*. When including systematic uncertainties, the endpoint values are more similar and the deviation is no longer significant.

Furthermore, the first tritium data was analyzed using different final state distributions. It was demonstrated, that the goodness-of-fit can be slightly improved when including the normalization of ground and excited states as two additional free parameters in the fit, accompanied by a pull term. Moreover, it was shown that the model does not describe the data well, when no excited states or even no final state at all are assumed. Surprisingly, the contrary is true when fitting the data with a model assuming the [FSD](#) for different isotopologues than DT. When the [FSD](#) for either HT or T₂ is used, which both come from a different calculation than DT, the fit yields the best p-values of all considered scenarios. This emphasizes the need of a more accurate description of the [FSD](#).

Lastly, an alternative approach to determine the column density was explored. The conventional estimation of ρd during the first tritium campaign was the comparison of observable parameters, such as the vessel pressure, with thermodynamical gas simulations of the [WGTS](#) hardware group. Besides that, the integral spectrum itself provides a handle on the column density through its impact on the tritium activity and the inelastic scattering in the [WGTS](#). The column density was fit to the integral spectrum using different energy ranges. The sensitivity on the column density using this approach is larger than the systematic uncertainty of 2.2% provided by the [WGTS](#) hardware group. For the full measurement energy range the uncertainty on ρd is 4.2%. In addition to that, this

uncertainty increases with decreasing energy range. However, even though this approach cannot compete with the standard method of the first tritium campaign, it provides a consistency check. When systematic uncertainties are taken into account, the central values of the retrieved column densities for the long energy ranges are about 5% larger than the anticipated one. Moreover, a qU dependent pattern is observable. Similar to the pattern of the endpoint fit results as a function of measurement range, the column density is rather constant until ≈ 300 eV below the endpoint. Thereafter, it fluctuates up and down. Following the previous discussion on the fluctuations of the endpoint variations, higher statistics close to the endpoint are required for further investigations.

Neutrino Mass Sensitivity at Elevated Background Level

In this thesis, a comprehensive neutrino mass sensitivity study for the [KATRIN](#) experiment in the light of the elevated background level was performed. To describe systematic effects as accurate as possible, covariance matrices were customized for any [KATRIN](#) hardware configuration, such as magnetic field configuration or measurement time distribution. The [KATRIN](#) operational parameters were varied, in order to explore a larger parameter space to find ways of improving the neutrino mass sensitivity.

It was found, that it is beneficial to adapt the magnetic field configuration to the new background scenario: An increase of the magnetic field strength in the analyzing plane B_a leads to a reduced flux tube volume of the main spectrometer. As the background is approximately proportional to the volume of the flux tube, the background rate can be decreased by increasing the magnetic field in the analyzing plane. The drawback of this is a worsening of the energy resolution. This work demonstrates that the optimal B_a is enlarged to 7 G with respect to the nominal value of 3 G. This setting corresponds to a background rate of 364 mcps for the full [FPD](#) and a spectrometer energy resolution of 3.1 eV.

Furthermore, it was shown that the choice of the measurement time distribution plays a key role in the sensitivity optimization. On the one hand, the more time is spent at retarding potentials far below the endpoint, the better is the statistical sensitivity due to the increased rate. On the other hand, it was found in the frame of this thesis that systematic uncertainties, in particular those originating from the [FSD](#) and $\rho d \cdot \sigma_{\text{inel}}$, increase strongly when extending the measurement range. The conclusion is that the optimal [MTD](#) with respect to the neutrino mass sensitivity, should spend only a small fraction of time at retarding potentials more than 30 eV below the endpoint in order to improve the statistical sensitivity, but not as long to be dominated by systematic uncertainties. An attempt was made to design such an [MTD](#) with [Samak](#), called *IsoStat*⁺. Not exhausting its full potential yet, it still requires further development.

The total sensitivity for one month of data taking, corresponding approximately to the scheduled time of the first [KATRIN](#) neutrino mass measurement campaign in March 2019, amounts to about 810 meV for the 30 eV and about 770 meV for the 60 eV range using the *IsoStat*⁺ [MTD](#). This demonstrates that a sub-eV sensitivity is within reach already in the first neutrino mass campaign, halving the current upper limit.

Additionally, the neutrino mass sensitivity for the full anticipated measurement time of 30 months was calculated. Considering the largely elevated background level, the sensitivity exceeds the design value of 200 meV: It amounts to about 350 meV for the 30 eV range and to approximately 330 meV for the 60 eV range. However, this large increase does not originate from additional systematic effects or the new systematics treatment, but comes mainly from the reduced statistical sensitivity. The elevated background reduces the absolute shape distortion of the integral spectrum caused by a given neutrino mass and therefore directly impacts the statistical sensitivity. This thesis revealed, that the neutrino mass measurement is still strongly dominated by statistic uncertainties for a measurement time of 30 months. The equilibrium between statistic and systematic uncertainties will be reached for the 30 eV range after as much as 450 months and for the 60 eV range after 50 months. This demonstrates, that [KATRIN](#) has the potential of improving its sensitivity by either extending its operation time or by taking means to mitigate its background.

List of Acronyms

Samak Simulation and Analysis with Matlab for KATRIN

KATRIN KARlsruhe TRItium Neurino

TDR KATRIN Design Report

MTD measurement time distribution

WGTS windowless gaseous tritium source

FPD focal plane detector

LARA LAsEr RAmAn spectroscopy

SDS spectrometer detector section

ROI region of interest

FSD final state distribution

TASR tritium activity fluctuations per subrun

pdf probability distribution function

LS least squares

MC Monte Carlo

DAQ data acquisition

DPS differential pumping system

CPS cryogenic pumping system

Appendices

Appendix A

Measurement Time Distributions

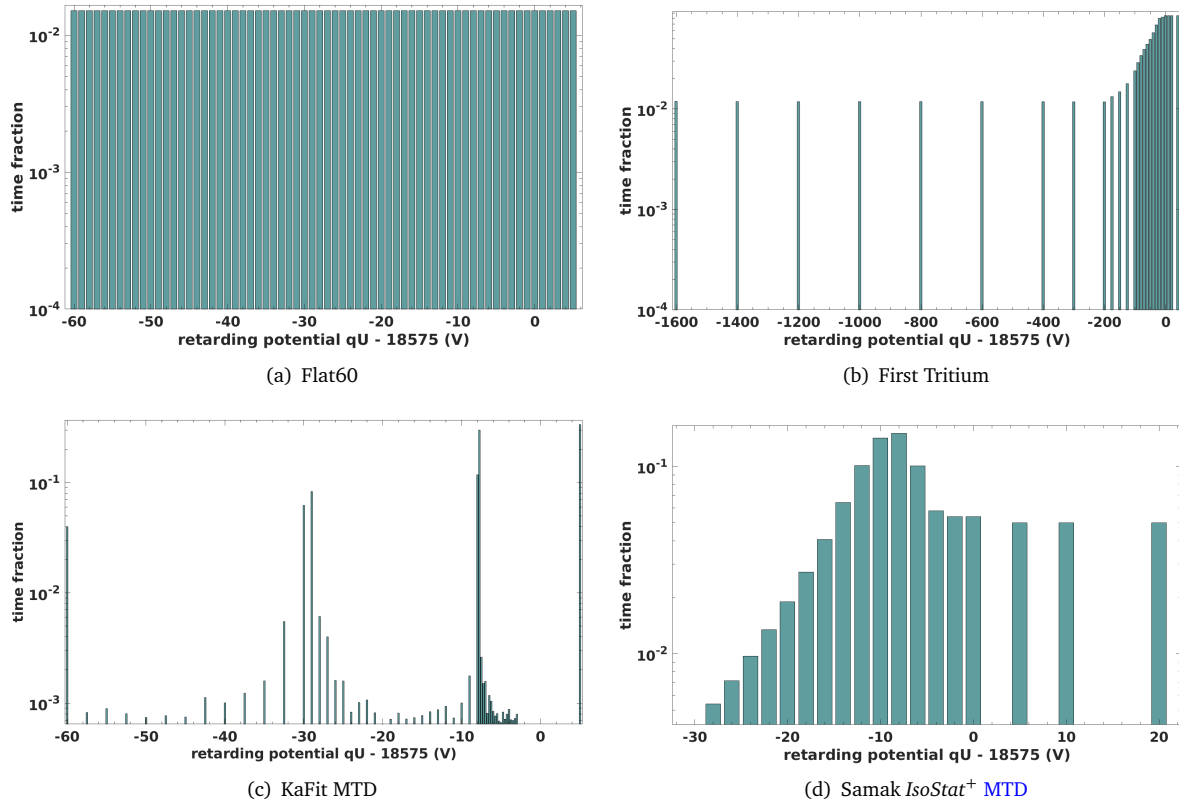
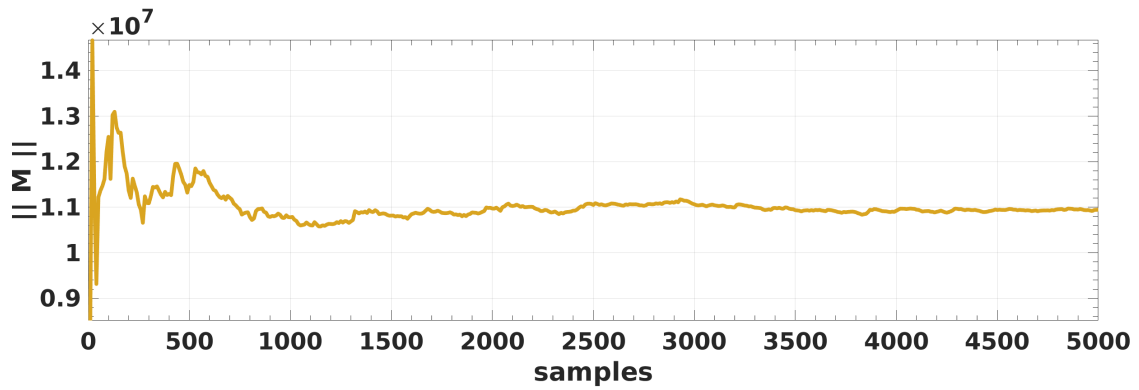


Figure A.1: measurement time distribution (MTD), which are used in the work at hand. The retarding potential qU below the anticipated endpoint of 18575 V is entered on the x-axis. The fraction of total measurement time, spent at each high voltage point, lies on the y-axis. **Top Left:** *Flat60*. The same fraction of measurement time is spent at each retarding potential. The retarding potential set points are equally spaced. **Top Right:** measurement time distribution (MTD) of the first tritium commissioning measurements. **Bottom Left:** *KaFit* MTD, obtained with Monte Carlo Markov Chain method. The MTD is optimized for an energy interval of $[E_0 - 60 \text{ eV}, E_0 + 5 \text{ eV}]$, a magnetic field strength in the analyzing plane of $B_a = 7 \text{ G}$ and 70% magnetic field strength of the pinch and source magnets. All other settings are nominal. **Bottom Right:** *IsoStat*⁺ MTD, optimized for an energy range of $[E_0 - 30 \text{ eV}, E_0 + 20 \text{ eV}]$, a magnetic field strength in the analyzing plane of $B_a = 7 \text{ G}$ and 70% magnetic field strength of the pinch and source magnets. All other settings are nominal. The MTD consists of three components with different weights: the inverse rate of the integrated tritium spectrum, the neutrino mass signal inside the spectrum and bins above the endpoint for the background determination. The MTD is optimized by minimizing the sensitivity for variable weights.

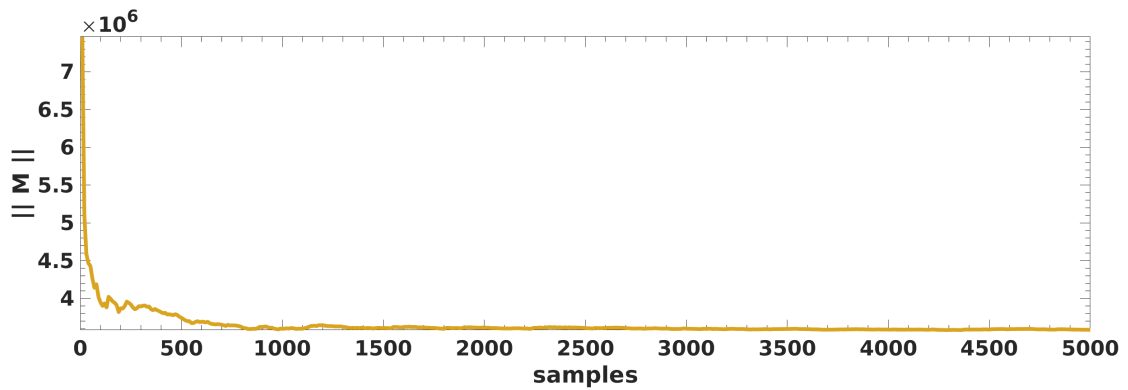
Appendix B

Covariance Matrices

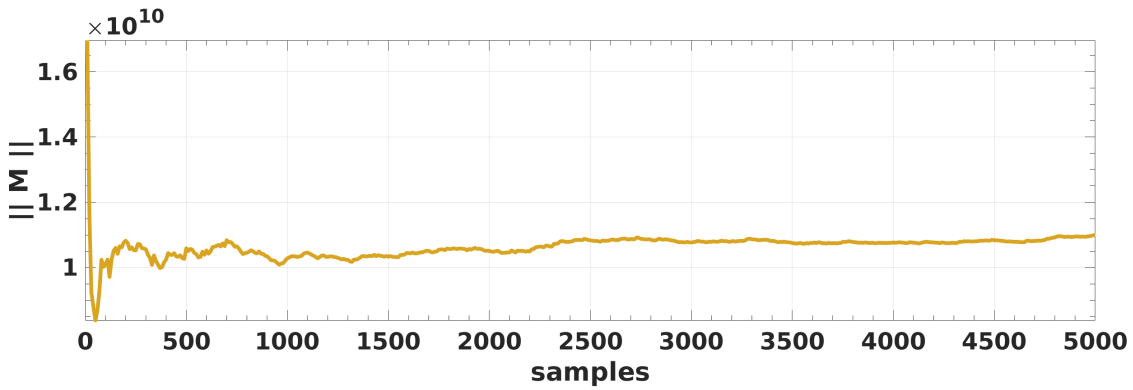
B.1 Convergence Test



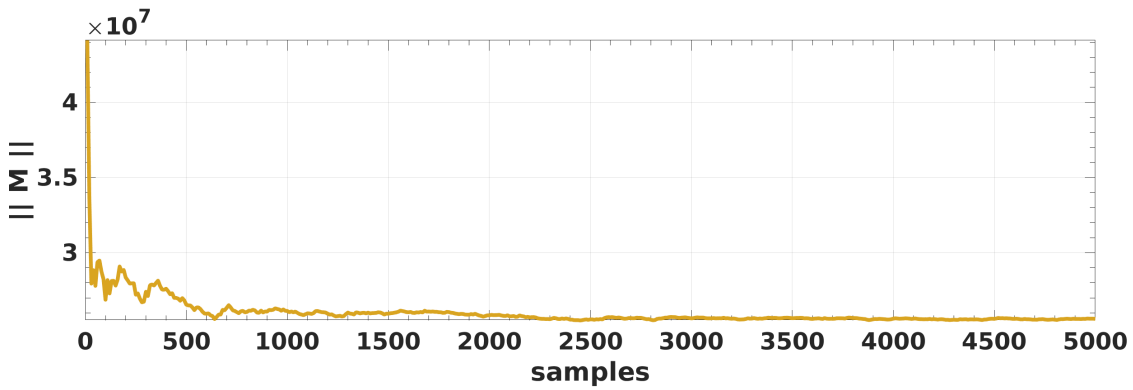
(a) Molecular final state distribution



(b) Tritium activity fluctuations per subrun



(c) Response function



(d) Run combination - stacking

Figure B.1: Covariance matrices, estimated with the MultiSim method are tested for convergence according to section 5.4.2 using the Cauchy Convergence Criteria. The plots show the matrix norm as a function of samples.

B.2 Final State Distribution

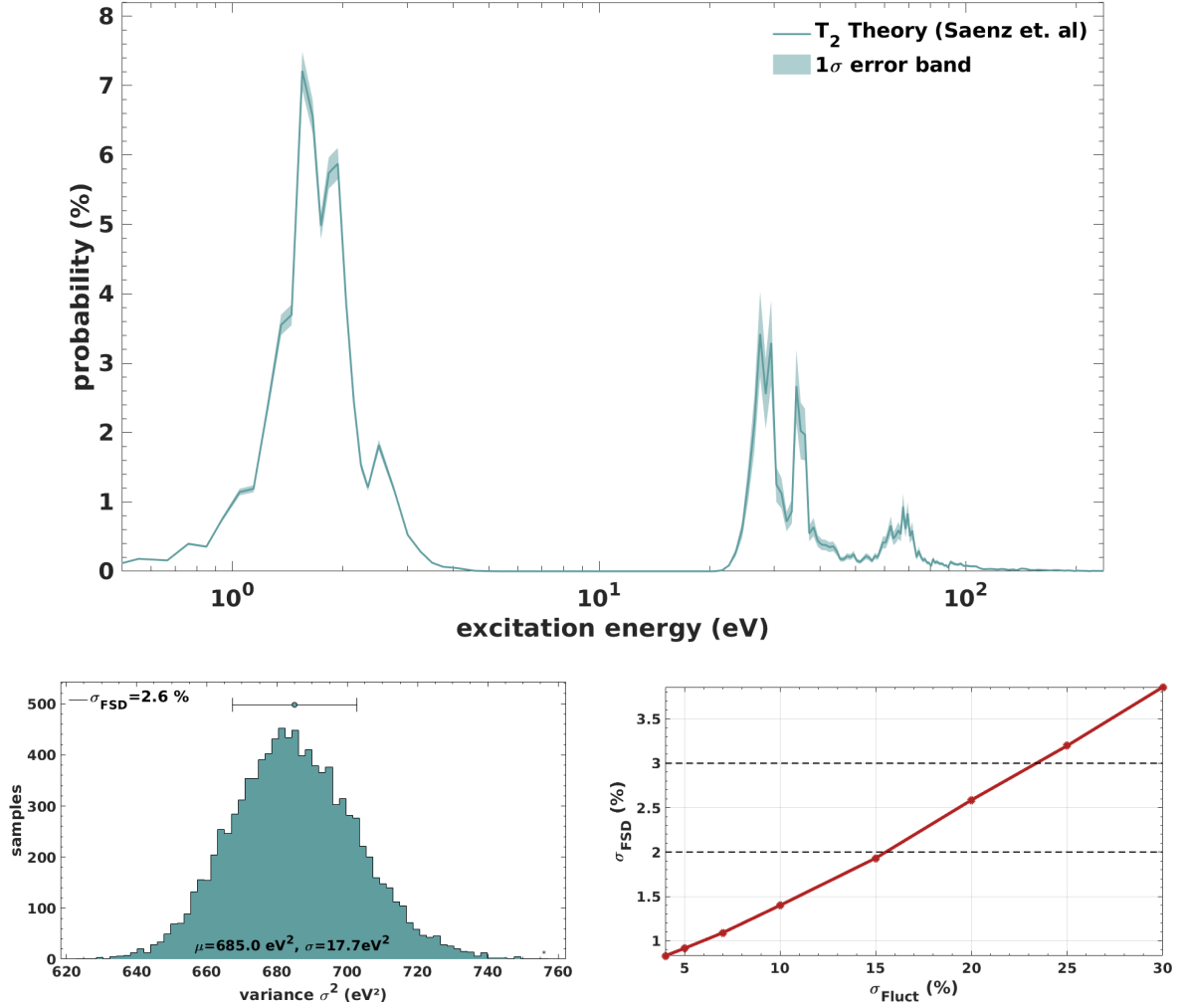


Figure B.2: **Top:** 1σ uncertainty band for the whole T_2 final state distribution. The normalization of ground to excited states probability is varied within 1%. The bin-to-bin uncorrelated Gaussian fluctuation σ_{Fluct} is 4% for the ground state and 20% for the excited states. This corresponds to a variation of the variance for the whole spectrum σ_{FSD} of 2.6% and for the ground state of 1.1%. **Bottom Left:** Histogram of the final state distribution variance σ^2 for 10,000 samples. The normalization uncertainty from ground to excited states is 1%. The intensity of the uncorrelated Gaussian bin-to-bin fluctuation σ_{Fluct} is 4% for the ground state and 20% for the excited states. This results in a mean variance of 685 eV². The relative variation of this variance is 2.6%. **Bottom Right:** Standard deviation of the FSD variance σ_{FSD} as a function of σ_{Fluct} . In order to obtain an uncertainty of 2-3% on the FSD variance, the bin-to-bin uncorrelated uncertainty has to be between 15% and 25%.

B.3 Response Function

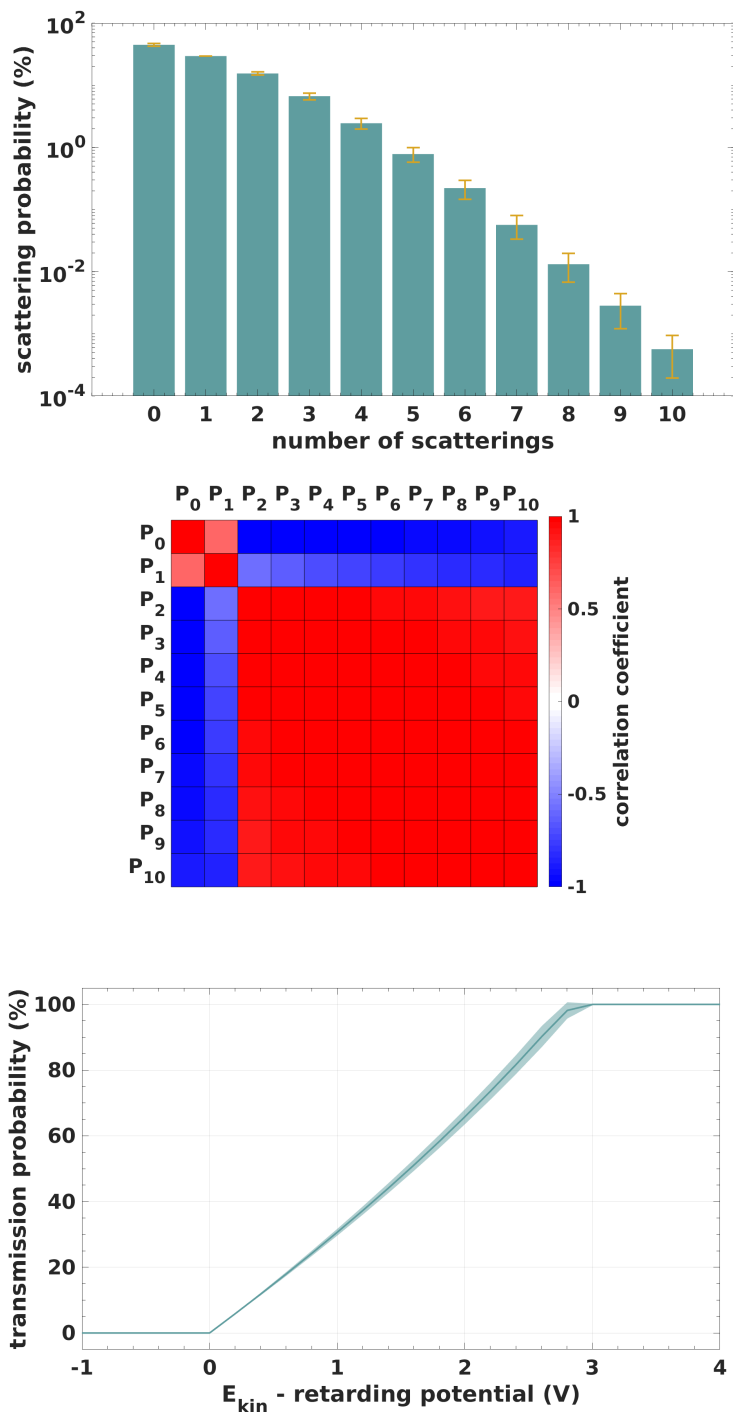


Figure B.3: **Top:** Inelastic Scattering Probabilities and Uncorrelated Uncertainties. There is 2% uncertainty on the magnetic fields and 5% on $\rho d\sigma$. **Center:** Correlation Matrix for Scattering Probabilities. **Bottom:** Transmission Function with 1σ -error band. The uncertainty for B_s and B_{max} are 2%.

B.4 Theoretical Corrections

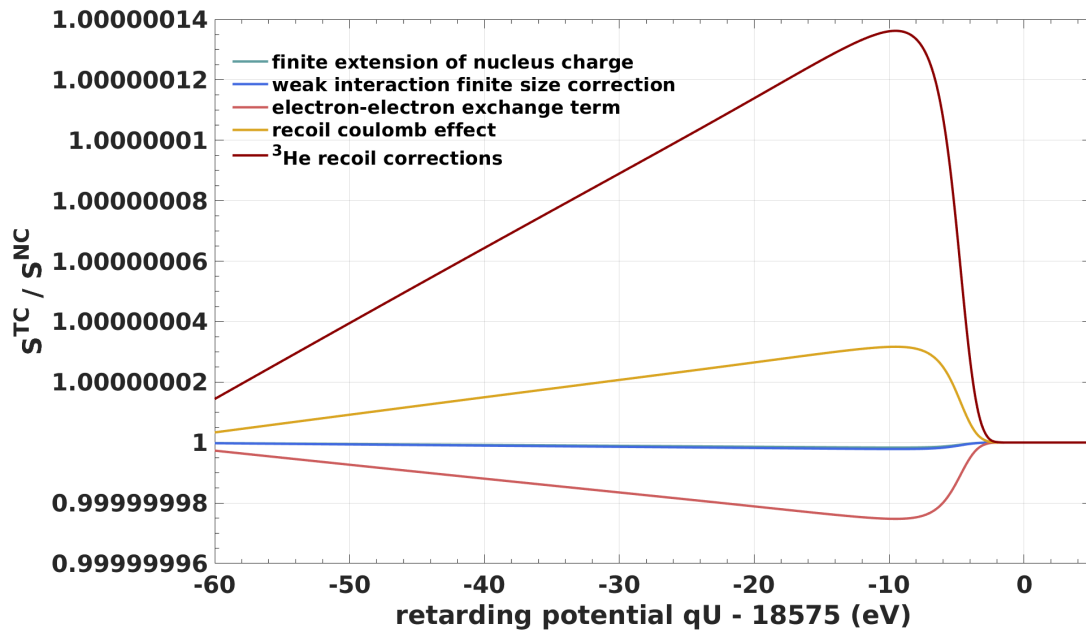


Figure B.4: Ratio of integral spectrum with theoretical corrections to the uncorrected integral spectrum. Only the minor corrections are considered. The correction from the finite extension of nuclear charge and the finite size in the weak interaction lie on top of each other.

Appendix C

First Tritium Campaign

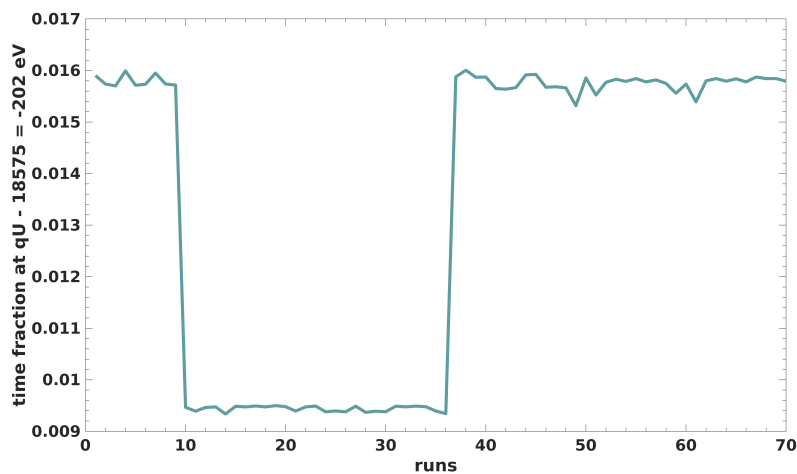


Figure C.1: Fraction of time, spent at the retarding potential $qU - 18575 = 202 \text{ eV}$ as a function of runs.

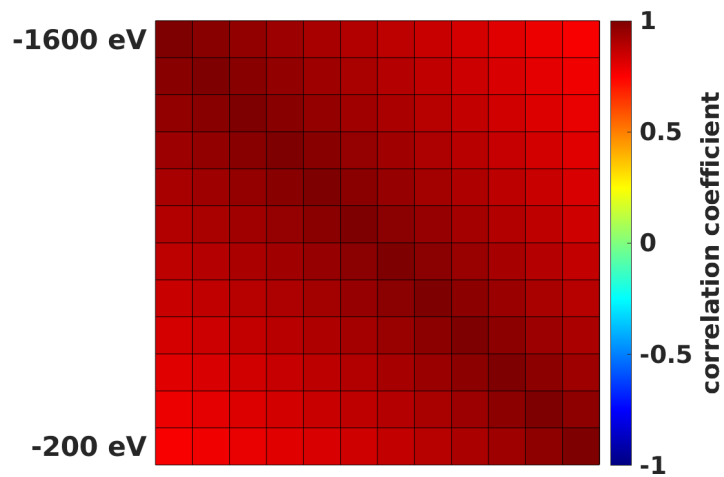


Figure C.2: Correlation matrix for energy range dependent fit results.

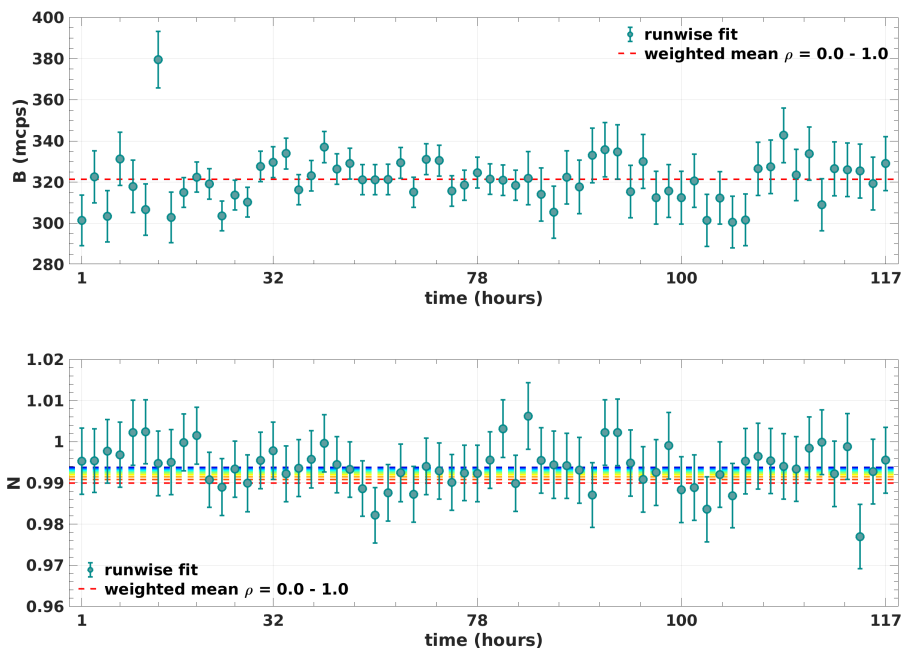


Figure C.3: Stability of fit results over time for the 400 eV range including statistic and systematic uncertainties. **Top:** Background rate. **Bottom:** Signal Normalization

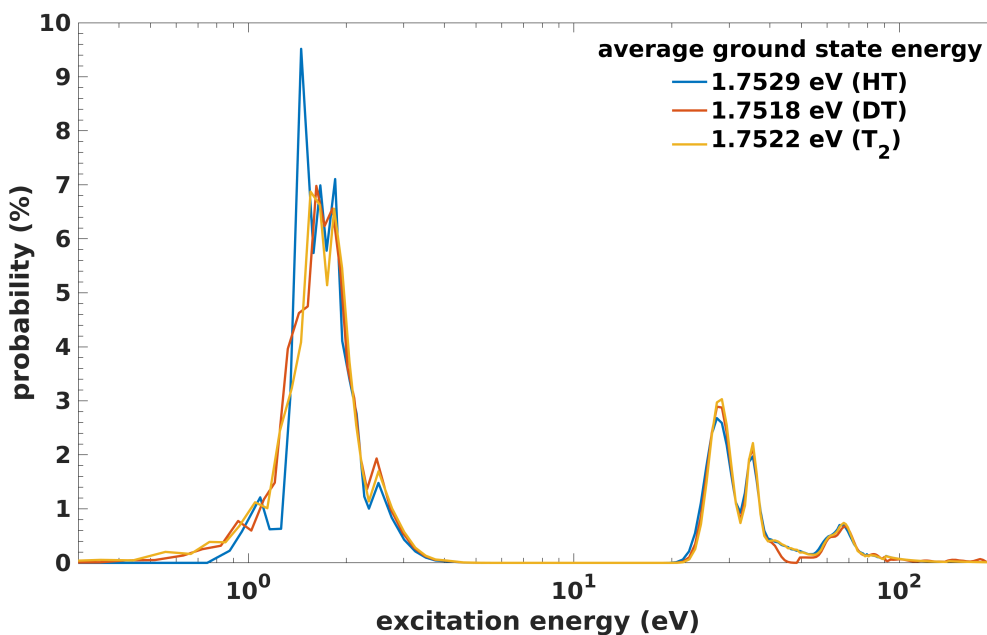


Figure C.4: Molecular final state distribution for the three isotopologues HT (Saenz *et al.*), DT (Doss *et al.*) and T₂ (Saenz *et al.*). The FSD differ only little in their average ground state energy.

Appendix D

Neutrino Mass Sensitivity Studies

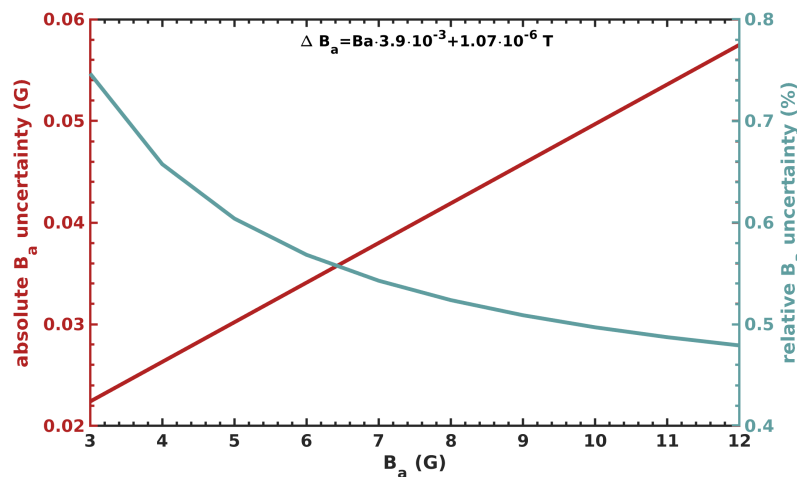


Figure D.1: Uncertainty on the magnetic field strength in the analyzing plane B_a . While the absolute uncertainty increases with rising B_a , the relative uncertainty decreases.

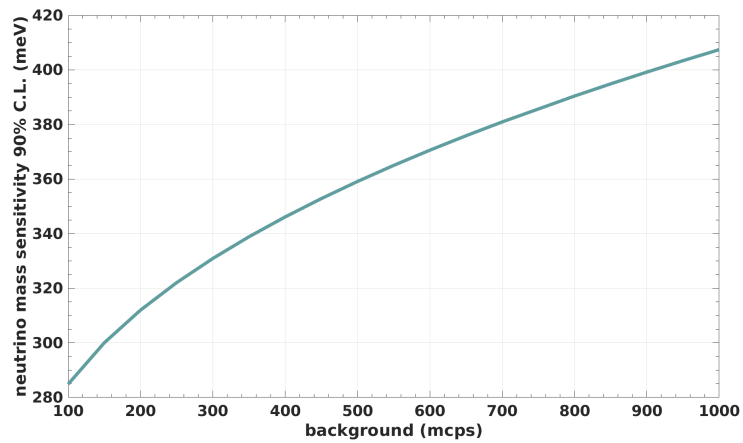


Figure D.2: Statistical neutrino mass sensitivity after 30 months as a function of the background rate. The *IsoStat*⁺ MTD is adapted to every background level for the 30 eV interval. All *KATRIN* parameters, which aren't nominal, are chosen according to table 8.3

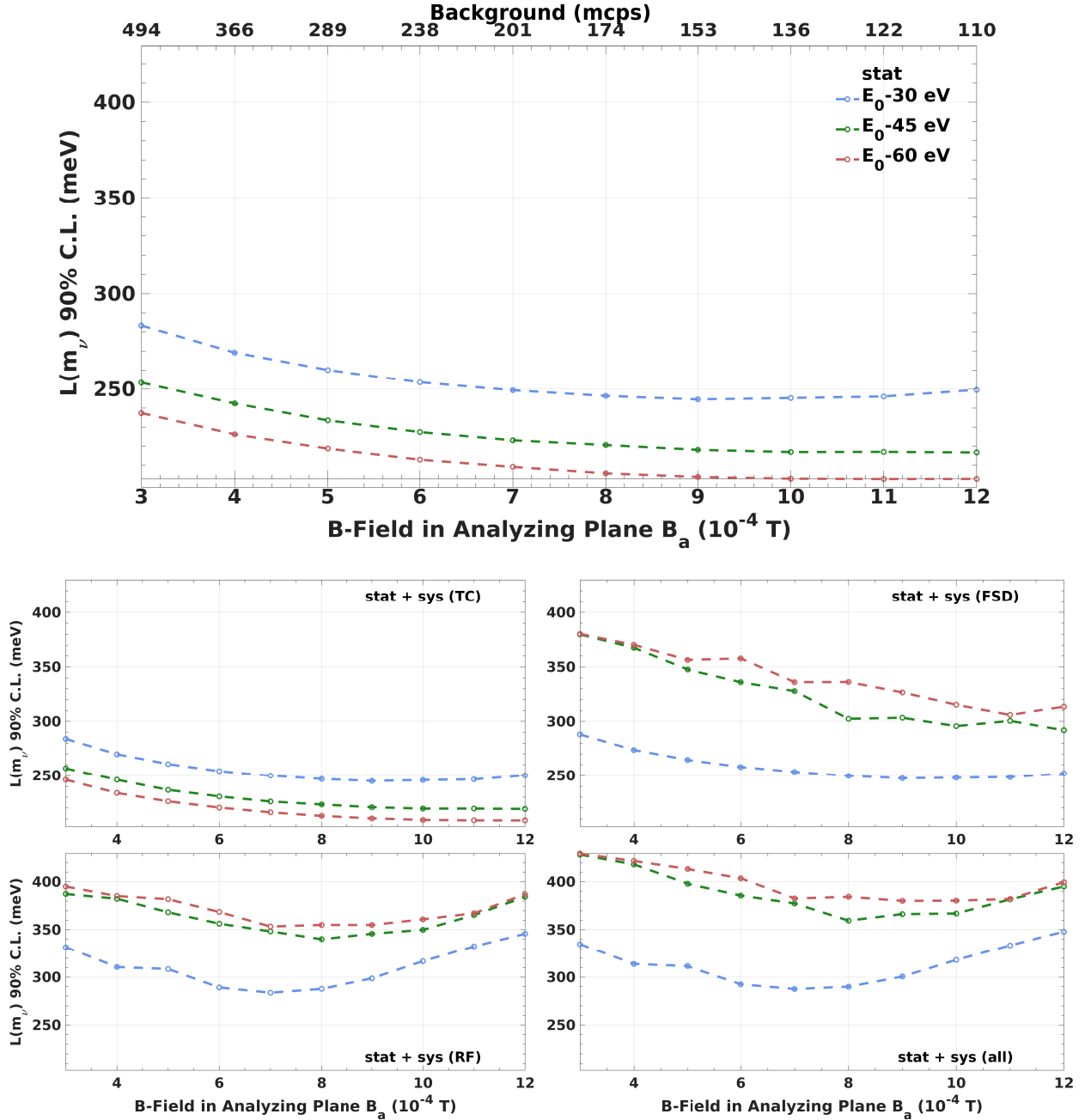


Figure D.3: Neutrino mass sensitivities for three scan ranges. In order to adapt the magnetic field in the analyzing plane B_a to the elevated background level, sensitivities are calculated for ten different B_a . Considering only statistical uncertainties, the best sensitivity is obtained with a *MTD*, going 60eV below the endpoint, and a B_a larger than $9 \cdot 10^{-4}$ T. This picture changes then systematic effects are included. The uncertainties on the response function (RF) as well as on the final state distribution (FSD) cause a switch in best measurement range. The optimal measurement range, using the *KaFit MTD*, is in this case 30 eV.

Bibliography

- [A⁺a] D. N. Abdurashitov et al. Electron scattering on hydrogen and deuterium molecules at 14–25 keV by the “Troitsk nu-mass” experiment. *Phys. Part. Nucl. Lett.* **14**(6), 892-899 (2017).
- [A⁺b] J. Angrik et al. Katrin design report. *FZKA 7090 scientific report* (2005).
- [A⁺c] V.N. Aseev et al. Energy loss of 18 keV electrons in gaseous t and quench condensed d films. *The European Physical Journal D* **10**(1), 39-52 (2000).
- [A⁺01] Q.R. Ahmad et al. Measurement of the rate of $\nu_e + d \rightarrow p + p + e^-$ interactions produced by 8b solar neutrinos at the sudbury neutrino observatory. 2001. *Phys. Rev. Lett.* **87**, 071301.
- [A⁺11] V.N. Aseev et al. Upper limit on the electron antineutrino mass from the troitsk experiment. 2011. *Phys. Rev. D* **84**, 11.
- [A⁺18a] M. Agostini et al. Improved limit on neutrinoless double- β decay of ^{76}Ge from gerda phase ii. 2018.
- [A⁺18b] M. Arenz et al. First transmission of electrons and ions through the katrin beamline. 2018. *Journal of Instrumentation*.
- [AH08] A. Alhakim and W. Hopper. A non-parametric test for several independent samples. 2008. *Journal of Nonparametric Statistics*, **20**:3, 253-261.
- [Are16] M. Arenz. Commissioning of the vacuum system of the katrin main spectrometer. 2016. *JINST* **11**, no.04, P04011.
- [Bar89] R.J. Barlow. *A Guide to the Use of Statistical Methods in the Physical Sciences*. Wiley, 1989.
- [BB18] J. Behrens and F. Block. Katrin first tritium reference report - systematic uncertainty of magnetic field in the analyzing plane. 2018. *Internal Analysis Report*.
- [Beh] J. Behrens. *MTD workshop and internal communication* (2018).
- [BG19] F. Block and Marsteller A. Glück, F. Katrin first tritium reference report systematic uncertainty of column density, 2019. *Internal Analysis Report*.
- [BK00] V.V. Buldygin and Yu. V. Kozachenko. *Metric characterization of random variables and random processes (Translations of Mathematical Monographs)*. American Mathematical Society, 2000.
- [Blo18] F. Block. Characterisation of the background in the katrin experiment. Master’s thesis, 2018. *Karlsruhe Institute of Technology*.
- [BPR] L. I. Bodine, D. S. Parno, and R. G. H. Robertson. Assessment of molecular effects on neutrino mass measurements from tritium β decay. *Phys. Rev. C* **91**, 035505 (2015).
- [Bra14] S. Brandt. *Data Analysis - Statistical and Computational Methods for Scientists and Engineers*. Springer, 2014.

- [CJRH⁺56] C.L. Cowan Jr., F. Reines, F.B. Harrison, H. W. Kruse, and A. D. McGuire. Detection of the free neutrino: a confirmation. 1956. [Science 124, 3212](#).
- [Cow98] G. Cowan. *Statistical Data Analysis*. Oxford University Press, 1998.
- [DHH68] Raymond Davis, Don S. Harmer, and Kenneth C. Hoffman. Search for neutrinos from the sun. 1968. [Phys. Rev. Lett. 20, 1205](#).
- [E⁺] M. Erhard et al. Technical design and commissioning of the katrin large-volume air coil system. [JINST 13, no.02, P02003 \(2018\)](#).
- [Eno18] S. Enomoto. Internal communication. 2018.
- [Erh16] M. Erhard. *Influence of the magnetic field on the transmission characteristics and the neutrino mass systematic of the KATRIN experiment*. PhD thesis, 2016. [Karlsruhe Institute of Technology](#).
- [F⁺85] O. Fackler et al. Accurate theoretical β -decay energy spectrum of the tritium molecule and its neutrino mass dependence. 1985. [Phys. Rev. Lett. 55, 1388](#).
- [F⁺98] Y. Fukuda et al. Evidence for oscillation of atmospheric neutrinos. 1998. [Phys. Rev. Lett. 81, 1562](#).
- [Fra] A.J. Franke. *Searching for Reactor Antineutrino Flavor Oscillations with the Double Chooz Far Detector*. PhD thesis. [Colombia University \(2012\)](#).
- [Fur39] W. H. Furry. On transition probabilities in double beta-disintegration. 1939. [Phys. Rev. 56, 12](#).
- [G⁺] F. Glück et al. Design document - air coil system & magnetic field sensor system. [internal KATRIN document \(2009\)](#).
- [G⁺16] A. Gando et al. Search for majorana neutrinos near the inverted mass hierarchy region with kamland-zen. 2016. [Phys. Rev. Lett. 117, 082503](#).
- [GP12] A. Giuliani and A. Poves. Neutrinoless double-beta decay. 2012. [Adv. High Energy Phys. 2012, 857016](#).
- [H⁺17] F. Heizmann et al. The windowless gaseous tritium source (wgts) of the katrin experiment. 2017. [J. Phys.: Conf. Ser. 888 012071](#).
- [Har15] F. Harms. *Characterization and Minimization of Background Processes in the KATRIN Main Spectrometer*. PhD thesis, 2015. [Karlsruhe Institute of Technology](#).
- [Hue] W. Huelsnitz. *Handling Uncertainties in IceCube with Covariance Matrices*. [Ice Cube Tech Note \(2011\)](#).
- [Jam94] F. James. Minuit (function minimization and error analysis) reference manual. 94.1, 1994. [CERN Program Library entry D506](#).
- [K⁺05] Ch. Kraus et al. Final results from phase ii of the mainz neutrino mass search in tritium β decay. 2005. [Eur. Phys. J. C 40: 447](#).
- [K⁺18] M. Kleesiek et al. β -decay spectrum, response function and statistical model for neutrino mass measurements with the katrin experiment. 2018. [arXiv:1806.00369](#).
- [KAT] [Internal KATRIN document](#).
- [Kle14] M. Kleesiek. *A Data-Analysis and Sensitivity-Optimization Framework for the KATRIN Experiment*. PhD thesis, 2014. [Karlsruhe Institute of Technology](#).
- [L⁺11] S. Lukic et al. Measurement of the gas-flow reduction factor of the katrin dps2-f differential pumping section. 2011. [Vacuum 86, 8](#).

- [Liu73] J. W. Liu. Total inelastic cross section for collisions of H₂ with fast charged particles. 1973. [Phys. Rev. A 7, 103](#).
- [Liu87] J. W. Liu. Total cross sections for high-energy electron scattering by H₂ ($^1 \Sigma_g^+$), N₂ ($^1 \Sigma_g^+$), and O₂ ($^3 \Sigma_g^-$). 1987. [Phys. Rev. A 35, 591](#).
- [LP12] J. Lesgourgues and S. Pastor. Neutrino mass from cosmology. 2012.
- [Mer12] S. Mertens. *Study of Background Processes in the Electrostatic Spectrometers of the KATRIN experiment*. PhD thesis, 2012.
- [MG18] P. I. Morales Guzmán. Simulation, data challenge, and analysis of first katrin tritium data. Master's thesis, Technical University of Munich, 2018.
- [MNS62] Z. Maki, M. Nakagawa, and S. Sakata. Remarks on the unified model of elementary particles. 1962. [Prog. Theor. Phys. 28, 5](#).
- [OW08] E.W. Otten and C. Weinheimer. Neutrino mass limit from tritium β decay. 2008. [Reports on Progress in Physics 71, 8](#).
- [Pau30] W. Pauli. Open letter to the group of radioactive people at the gauverein meeting in tübingen. 1930. [MicroBooNE Document Database of Fermi National Accelerator Laboratory](#).
- [Pol] A. Pollithy. *In Preparation*. PhD thesis, Technical University of Munich.
- [Pon58] B. Pontecorvo. Inverse beta processes and nonconservation of lepton charge. *Zh. Eksp. Teor. Fiz.*, 34(247), 1958.
- [PRS⁺15] B. Povh, K. Rith, C. Scholz, F. Zetsche, and W. Rodejohann. *Particles and Nuclei - An Introduction to the Physical Concepts*. Springer, 2015.
- [R⁺] R. G. H. Robertson et al. Limit on ν_e^- mass from observation of the β decay of molecular tritium. [Phys. Rev. Lett. 67, 957 \(1991\)](#).
- [Rei13] J. C. Reich. *Magnetic Field Inhomogeneities and Their Influence on Transmission and Background at the KATRIN Main Spectrometer*. PhD thesis, 2013. [Karlsruhe Institute of Technology](#).
- [Rob18] R. G. H. Robertson. Internal communication. 2018.
- [Rö17] C. Röttele. Results of the first cool-down of the katrin cryogenic pumping section. 2017. [J. Phys.: Conf. Ser. 888 012228](#).
- [Sch16] K. Schönung. *Development of a Rear Wall for the KATRIN Rear Section and investigation of tritium compatibility of Rear Section components*. PhD thesis, 2016. [Karlsruhe Institute of Technology](#).
- [SD] W. Stoeffl and D. J. Decman. Anomalous structure in the beta decay of gaseous molecular tritium. [Phys. Rev. Lett. 75, 3237 \(1995\)](#).
- [SJF] A. Saenz, S. Jonsell, and P. Froelich. Improved molecular final-state distribution of het^+ for the β -decay process of T₂. [Phys. Rev. Lett. 84, 242 \(2000\)](#).
- [T⁺] M. Tanabashi et al. *Review of Particle Physics*. [Phys. Rev. D. 98, 030001 \(2018\)](#).
- [Tro18] N. Trost. *Modeling and measurement of Rydberg-State mediated Background at the KATRIN Main Spectrometer*. PhD thesis, Karlsruhe Institute of Technology, 2018.
- [Wan13] N. Wandkowsky. *Study of background and transmission properties of the KATRIN spectrometers*. PhD thesis, 2013. [Karlsruhe Institute of Technology](#).

Acknowledgment

I would like to thank all the people who supported me during my master's thesis, in particular:

- DR. THIERRY LASSERRE for sharing his expertise with me in extensive discussions about physics, KATRIN and the best location for a Samak team meeting.
- PROF. DR. SUSANNE MERTENS for giving me the opportunity to join the KATRIN collaboration and for letting me spend all my master's money on a summer school in Siberia.
- DR. MARTIN SLEZÁK for instructive discussions on confidence intervals and error propagation.
- DR. KATRIN VALERIUS, DR. JAN BEHRENS AND NIKOLAUS TROST for their helpful comments on previous sensitivity studies and background measurements.
- All members of the Munich KATRIN/TRISTAN group for making my time at MPP memorable. I enjoyed working with you, in particular during our many very last day(s) of summer.
- TIM BRUNST for proof reading this thesis and for making sure that the MPP-container never runs out of coffee.
- My friends and my volleyball team, who have been my constant source of balance and inspiration.

Finally, I would like to thank my parents for their permanent support and the many care packages, they send me all the way to Bavaria.